Spring 2019

ACOUSTIC DETECTION AND QUANTIFICATION OF CRUDE OIL

Scott Christopher Loranger
University of New Hampshire, Durham

Recommended Citation

Loranger, Scott Christopher, "ACOUSTIC DETECTION AND QUANTIFICATION OF CRUDE OIL" (2019). *Doctoral Dissertations*. 2456.
https://scholars.unh.edu/dissertation/2456

ACOUSTIC DETECTION AND QUANTIFICATION OF CRUDE OIL

BY

Scott Loranger
Biological Sciences (BS), Cornell University, 2009

DISSERTATION

Submitted to the University of New Hampshire
in Partial Fulfillment of
the Requirements for the Degree of

Doctor of Philosophy
in
Oceanography

May, 2019

This thesis/dissertation has been examined and approved in partial fulfillment of the requirements for the degree of Doctor of Philosophy in Oceanography by:

Thesis/Dissertation Director, Dr. Thomas C Weber, Associate Professor (Mechanical Engineering)

Dr. Nancy Kinner, Professor (Ocean Engineering)

Dr. Anthony Lyons, Research Professor (Ocean Engineering)

Dr. Larry Mayer, Professor (Earth Science)

Dr. David Valentine, Professor (Earth Science), University of California, Santa Barbara
on November 30, 2018

Original approval signatures are on file with the University of New Hampshire Graduate School.

Contributions and Publication Status

The material in this thesis is the work of the author and the co-authors listed in chapters 2 - 4. Specific contributions from co-authors are listed below.

Chapter 2:

Published: Loranger, Scott, Bassett, Chrisopher, Cole, Justin P., Boyle, Bret & Weber, Thomas C. 2018. Acoustically relevant properties of four crude oils at oceanographic temperatures and pressures. *The Journal of the Acoustical Society of America*, **144** (5), 2926-2936.

Differential scanning calorimetry measurements and interpretation of the results were provided by Justin P Cole and Bret Boyle of the Department of Chemistry at Colorado State University.

The reflection coefficient analysis in Figure 2.11 as well as assistance with the literature review was provided by Christopher Bassett of NOAA National Marine Fisheries Service.

Chapter 3:

Revision submitted to the Journal of the Acoustical Society of America.

Bounday element method (BEM) modeling was performed by Geir Pedersen of the Norwegian Research Center.

Chapter 4:

In preparation for submission.

This thesis is dedicated to the memory of John ”Jack” Sibley Ostrom for always believing in me and for keeping me focused on my goals.

I would like to thank the many people who helped in the development of this thesis. Thanks to my committee members for their insights and encouragement in this work.

Special thanks goes to my advisor Tom Weber. My PhD experience has been incredibly rewarding and Tom has been an encouraging and enthusiastic presence. He has always demanded that I work to my full potential.

I would also like to thank the Earth Sciences Department and the School of Marine Science and Ocean Engineering, and especially Tom Lippmann. Tom Lippmann helped lay the ground work for my PhD and he was a tremendous help throughout my entire PhD experience. Similarly, I also appreciate all the conversations and assistance from Tony Lyons. He was always ready to provide help either in acoustics research or in everyday life.

Another thank you goes to the Center for Coastal and Ocean Mapping / Joint Hydrographic Center and NOAA for funding my PhD. Very sincere thank you to Larry Mayer for advice on science and on life. Larry is an inspiring person to work for and to work with and I feel very lucky to have been welcomed into CCOM/JHC.

I also need to thank the UNH graduate student community. I couldn't have done this without the friendship and support of the other students.

A special thanks goes to Danette Hedman for fostered my interest in science.

Thank you to my friends and family for their support and encouragement. Thank you to my mom, Janet Loranger, for taking me to see the movie version of Carl Sagan's *Contact* in theaters and starting this obsession with science.

Thank you to my amazing wife Rebecca Sanders-DeMott. You have been an incredible inspiration, partner, sounding board and support for me since we met - but especially through

my PhD experience. Thank you for putting up with me and for keeping me sane.

And lastly, but certianly not least, thank you to my daughter Quinn. Thank you for inspiring me to be my best and thank you for waiting until after I defended to come into the world.

Contents

List of Tables

List of Figures

Acoustic detection and quantification of crude oil

Scott Loranger

Abstract

The fate and transport of oil droplets from natural and anthropogenic sources is key to understanding the impact of spills and the resilience of marine communities. Without knowledge of natural background levels, it is difficult to determine the response of the marine environment to large influxes of oil. Current estimates of global flux of oil from natural seeps varies by an order of magnitude, and the wide range of estimates is due in part to the lack of sufficient in-situ quantification techniques for oil droplets in the water column. This work is focused on the feasibility of employing broadband acoustics to address this gap by developing a better understanding of the interaction between sound generated by broadband acoustics and oil droplets in the ocean. The dissertation is organized into three experiments, each written into a manuscript for peer-reviewed publication. The first addresses the paucity of data at oceanographically-relevant pressures and temperatures regarding the physical properties of crude oil that impact acoustic scattering. The acoustic impedance of four crude oils was measured under oceanographic conditions using a sound speed chamber designed and constructed for this experiment. Measurements showed significant deviations from an often-used empirical model and a new empirical model was developed. The results of the first experiment were used in the analysis of the second study. High frequency broadband acoustic backscatter was recorded from droplets of three different crude oils of varying size and shape and compared to three scattering models for fluid targets. The results highlighted the importance of droplet shape (i.e., deviations from a perfect sphere) in acoustic backscatter observations of crude oil droplets. The first two experiments were used to inform the analysis of the third experiment. Broadband acoustics along with ADCP measurements were used to determine flux at an anthropogenic seafloor release of oil and gas. Results of this

thesis indicate that broadband acoustics are capable of quantifying oil droplets and oil flux.

Chapter 1

Introduction

1.1 Background

It is estimated that over 2 million tons of oil enters marine environments from anthropogenic sources annually (GESAMP, 2007). Anthropogenic oil spills can have devastating impacts on marine organisms that cascade across trophic levels. For example, within the planktonic community an influx of hydrocarbons can have drastically different effects across species (Abbriano *et al.* , 2011). Certain species of hydrocarbon specialists will experience blooms following a spill event (Transportation Research Board and National Research Council, 2003; Valentine *et al.* , 2010), while other species will experience significant declines (Ozhan *et al.* , 2014). A study by Parsons *et al.* (2015) found that during the Deepwater Horizon spill the phytoplankton community as a whole decreased in abundance and that there was a significant shift in the community composition. At higher tropic levels the combined impacts of changes to the planktonic community assemblage and the effects of direct exposure to hydrocarbons result in significant changes including increased mortality and decreased fecundity (Beyer *et al.* , 2016). Increased oil concentrations in the marine environment impact economically important species including shrimp (Van Der Ham & De Mutsert, 2014), predatory pelagic fish (Incardona *et al.* , 2014) and marine mammals (Venn-Watson *et al.* , 2015). However, the impacts are highly variable and depend on the hydrocarbon concentrations experienced locally which can vary over small spatial scales within the spill area (Rozas *et al.* , 2000; Mendelssohn *et al.* , 2012).

Oil spill responders use the best available technology and science to respond to spills and mitigate environmental and economic impacts, however, they are often hampered by a lack of real time *in-situ* data on the fate and transport of oil, especially from seafloor hydrocarbon sources. Oil spills cover massive areas with hydrocarbon concentrations varying locally on scales of tens of meters. The most efficient and effective response to a spill would be to determine where the impacts will be greatest and use the available response resources in those areas. However, without *in-situ* oil detection and quantification techniques, especially in the water column, responders do not have the information they need to adequately determine what areas are likely to be the most significantly impacted. The work presented in this thesis describes novel *in-situ* acoustic methodologies developed for the detection and quantification of oil in the marine environment to address this critical gap in knowledge.

The lack of *in-situ* measurements of oil leads to many unanswered questions about the environmental response to influxes of oil - both anthropogenic and natural - across the climatically and ecologically diverse environments that are exposed to hydrocarbons. Understanding potential environmental impacts due to spills and developing an appropriate response requires both the ability to quantify the total volume of oil spilled and knowledge of baseline levels of natural oil seepage. Current estimates of the global flux of oil from natural sources varies by an order of magnitude (Transportation Research Board and National Research Council, 2003) and this uncertainty in background levels results in uncertainty of the potential impacts of a spill on the environment. For example, the Deepwater Horizon spill was an influx of between 34 - 340% of the total annual flux from natural sources in the Gulf of Mexico (United States & Coast Guard, 2011). While any increase above background levels is likely to have an environmental impact, knowledge of the magnitude of a spill relative to background levels is necessary both to inform decision making during spill response and to assess the long-term impact on the environment. Acoustic methods offer a path toward quantifying both anthropogenically released and naturally occurring liquid hydrocarbons in the ocean.

Active acoustic methods have been used to estimate the flux of oil from seafloor wells (Camilli *et al.* , 2012), to determine flux of oil at ranges of up to a hundred meters from the instrument (Weber *et al.* , 2012) and to estimate the thickness of oil layers under sea ice (Wilkinson *et al.* , 2015; Bassett *et al.* , 2016; Pegau *et al.* , 2017). The main impediment to the use of acoustic methods for detection and quantification of oil is the low characteristic acoustic impedance contrast between crude oil and seawater. The contrast in the characteristic acoustic impedance (the product of the density and sound speed) determines the degree to which sounds is reflected and refracted at the boundary between two media; in this case the boundary of the ambient seawater and the oil droplet. While the acoustic impedance of oil is poorly understood at oceanographic conditions (see Chapter 2), it is sufficiently characterized to determine that the impedance is similar to that of water, and to therefore classify oil droplets in the ocean as weakly scattering.

Weakly scattering particles such as oil droplets reflect the most sound when the wavelength of the sound wave (λ) is of the same size or smaller than the radius of the particle (a), a situation referred to as geometric scattering. The relationship between wavelength and particle size is typically expressed in terms of ka where k is the acoustic wave number ($2\pi/\lambda$). When ka is less than one, described as Rayleigh scattering, the efficiency of scatter, or target strength (TS), for a weak scattererer decreases with a power law that goes as $(ka)^4a^2$ (Figure 1.1). TS is the ratio of the intensity of the backscattered sound to the intensity of the incident sound, and is therefore a measure of the efficiency of backscatter of a particle. Gas bubbles, which have a larger characteristic acoustic impedance contrast, are much better scatterers of sound and have a higher TS across all frequencies than an oil droplet of the same size. Wavelength is inversely proportional to frequency and low frequency waves, with large wavelengths, do not efficiently scatter sound from oil droplets. Figure 1.1

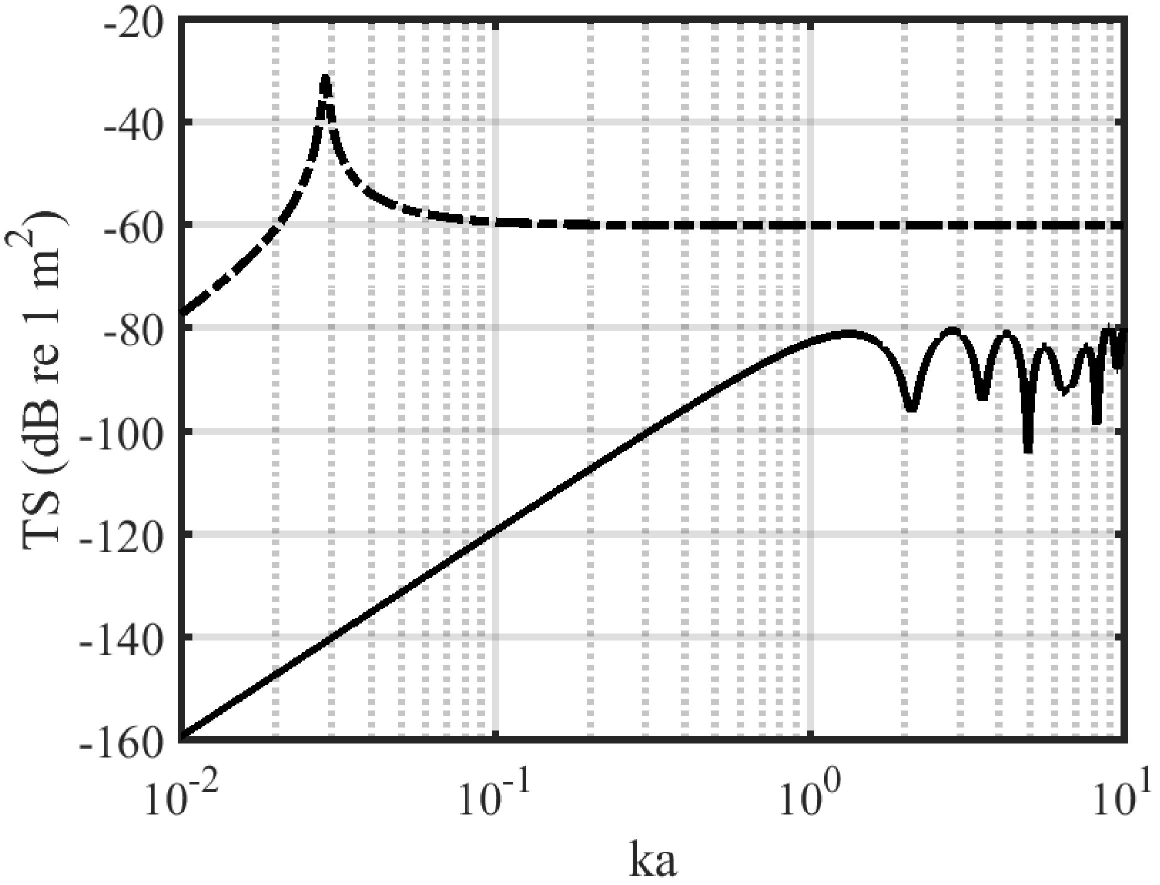

Figure 1.1: Target strength gas bubbles (dashed line) and oil droplets (solid line) according to Anderson (1950) as function of the size (a) and acoustic wave number (k).

shows the TS as a function of frequency for a one mm droplet according to the exact modal solution for a plane wave incident on a fluid sphere derived by Anderson (1950). For a 1 mm radius oil droplet, the transition from Rayleigh to geometric scattering occurs at around 240 kHz, and Figure 1.1 shows the decrease in TS at frequencies below 240 kHz. During the Deepwater Horizon spill Weber *et al.* (2012) were able to detect oil at distances greater than 100 meters with a 200 kHz shipboard echo sounder, however they were unable to detect oil at lower frequencies, where ka was much less than one.

The higher frequencies associated with the geometric scattering regime for oil droplets are also associated with increased signal attenuation (Figure 2). Absorption in seawater is greater for higher frequencies, and the increased attenuation at higher frequencies limits high frequency echo sounding to short ranges. There is a trade off in determining the frequency most appropriate for detecting oil droplets, frequencies should be high enough so that ka is around one but also low enough to mitigate signal attenuation due to absorption. One way to increase the signal to noise ratio (SNR), and therefore increase the range of detection, is to use a broadband acoustic signal. The acoustic waveform recorded by a broadband echo sounder can be matched-filtered, where the recorded signal is cross-correlated with the broadband transmit signal. A broadband matched-filter improves the SNR by approximately $2BT$ where B with the bandwidth of the signal and T is the pulse length (Turin, 1960; Chu & Stanton, 1998; Stanton & Chu, 2008; Lavery *et al.* , 2010; Stanton *et al.* , 2010).

The added benefit of using a broadband signal is that the broadband frequency response can be used to estimate the physical properties of a target. Backscattering measured at single frequency only reveals a point on the frequency response curve for a target, but when a wide range of frequencies is used the shape of the frequency response reveals information about the target. Previous work has used the broadband backscatter frequency response to differentiate between plankton and turbulent microstructure (Lavery *et al.* , 2010), to quantify bubbles under breaking waves (Medwin & Breitz, 1989; Terrill & Melville, 2000; Vagle & Farmer, 1992), and as an aid for classifying fish species (Holliday, 1972; Thompson & Love, 1996; Stanton *et al.* , 2010). The backscattering frequency response (Figure 1.1) for oil droplets is dependent on the droplet's impedance, size and shape. Therefore, if the impedance and shape are known, the frequency response can be used to estimate the remaining physical property; droplet size. In order to use the frequency response to quantify the physical properties of a target, some structure in the frequency response, such as a peak, null or change in slope, needs to be measured. The broader the transmitted signal, the more likely it is that a structure such as a null (or more ideally multiple nulls) will be within the ensonified range. In order to quantify droplets with broadband signals, the accuracy of acoustic scattering models, and the assumptions made in such models, for oil droplets must be verified (see Chapter 3).

Two potential impediments to the use of broadband acoustics for quantifying oil droplets come from other scatterers present at oil seeps; gas bubbles and biological scatterers (Judd, 2003; Sahling *et al.* , 2016; Kvenvolden & Cooper, 2003). Oil seeps, whether anthropogenic or natural, are often co-located with hydrocarbon gas bubbles. As discussed previously, gas bubbles have a higher impedance contrast with seawater than oil droplets and therefore are more efficient at scattering sound (Figure 1.1). When gas bubbles and oil droplets are in the same ensonified volume gas bubbles will mask any response from oil droplets, unless the oil is present in very high concentrations relative to the gas. Most planktonic organisms, on the other hand, are modeled as weak scatterers, just like oil droplets. Layers of planktonic organisms in the water column can mask oil droplets completely if present in dense enough layers. When concentrations of oil and gas are similar the TS of the biological scatterers can combine with the TS from oil droplets and suppress the peak and null shape used to quantify droplets when present in the same ensonified volume. While it is possible to quantify oil droplets under ideal laboratory conditions (see Chapter 3) at a field site where biological scatterers and gas bubbles are also present, quantification of oil will be more difficult (see Chapter 4).

The work presented in this thesis seeks to expand our understanding of how sound interacts with oil droplets in an effort to develop acoustic methodologies that will improve our understanding of the fate and transport of oil in the marine environment. The thesis consists of three studies of increasing spatial scale; a bench-top study of the physical properties of crude oil that determine scattering, a mesoscale laboratory study of the broadband scattering from individual oil droplets and a field evaluation of the use of shipboard broadband echo sounders to detect and quantify oil from a seafloor seep.

The study in Chapter 1 focused on the physical properties of oil that determine acoustic scattering at oceanographic conditions. In order to understand how sound interacts with oil droplets researchers need to know how the characteristic impedance - the density and sound speed - of oil varies as a function of depth and temperature in the ocean. Chapter 2 uses the results of chapter 1 to inform scattering models of oil droplets and compares the predictions of those models to empirical measurements of backscatter. In order to determine the physical properties of oil droplets - most importantly the droplet size - acoustically researchers need to know that models of acoustic backscatter from oil droplets are accurate and precise. If the sound speed and density of oil droplets is known, it should be possible to determine droplet size acoustically. In Chapter 2, the broadband backscattering frequency response of oil droplets of varying and known size from three of the four oils studied in chapter 1 was measured *in-situ*. Three commonly used models for backscattering of fluid targets were then inverted for droplet size. The size measured empirically and the size predicted by the models was compared to determine the accuracy of inversions of those models. Chapter 3 then used the models verified in Chapters 1 and 2 to predict the scattering from oil droplets emanating from a seafloor seep source in the Gulf of Mexico. Droplet size was predicted by the rise rate of droplets determined acoustically. The droplet size predictions were combined with sound speed and density modeled by the results of Chapter 1 and used to predict the frequency response of oil droplets using a model verified in Chapter 2. The frequency response was then compared to the measured backscatter to determine the flux from the seep site.

The research questions, significance, hypotheses, and outcomes of the three chapters are outlined below.

Chapter 1.) Acoustically relevant properties of four crude oils at oceanographic temperatures and pressures

Question: Do oceanographic conditions cause significant deviations for the generally accepted model of the physical properties of oil, a model that is derived from measurements made at reservoir conditions?

Significance: Empirical models of density and sound speed, the properties that determine acoustic scattering, are derived from measurements of those properties made at reservoir conditions (very high temperature and pressure). At oceanographic conditions the waxes in some oils may solidify and could impact the density and sound speed.

Hypothesis: The formation of waxes in crude oils at oceanographic conditions will cause significant deviations between the measured density and sound speed and the density and sound speed predicted by the commonly used empirical model.

Outcomes: Significant deviations between measured and modeled sound speed and density were found at oceanographic conditions and a new empirical model for those properties at oceanographic conditions was derived. The new empirical model outperformed the commonly used model when compared to sound speed measurements from the literature.

2.) Broadband acoustic scattering from oblate hydrocarbon droplets

Question: Do currently used models of acoustic scattering from oil droplets accurately predict the backscatter from individual droplets accurately enough to quantify droplet size?

Significance: In order to quantify oil droplets with broadband acoustics, models of backscatter must accurately characterize the broadband backscattering frequency response, especially the peak and null structure of the acoustic backscatter to differentiate between droplet sizes. Previous work has assumed droplets are spheres and if this assumption is violated the use of sphere models is likely to cause significant errors when inverting scattering models to determine droplet size.

Hypothesis: Models that assume oil droplets are spherical will not accurately predict the frequency dependent backscatter of droplets that are non-spherical. Other models that account for more complex shapes will show better agreement between the peak and null shape of the TS and the shape of the TS measured experimentally.

Outcomes: A model for acoustic scattering from fluid spheres did not accurately predict the null location of droplet of known impedance, shape and size. The distorted wave Born approximation and boundary element method, models that account for more complex shapes, showed better agreement for medium oils between the predicted and measured null location and inversions of those models accurately predicted the droplet size within the accuracy of the experimental system. However, there were significant errors when using inversions of these models to predict droplet size for the heavy oil studied.

3.) Hydrocarbon detection and quantification at a marine oil and gas seep

Question: Can a shipboard broadband acoustic echo sounder determine the flux of oil from a seep site known to consistently be producing an oil slick in the Gulf of Mexico?

Significance: Shipboard broadband acoustics were deployed in the presence of gas bubbles and biological scatterers to determine the flux of oil *in-situ* from a seep site in the Gulf of Mexico. The determination of flux in the water column *in-situ* is a new tool in the oil spill responder toolkit that can be used to detect and quantify oil from greater distances then current detection methods.

Hypothesis: Broadband acoustic backscatter will be able to detect and quantify oil droplets from a seafloor seep site and distinguish between the droplets, biological scatterers and hydrocarbon gas bubbles present at the site. The results will be a determination of the flux from a seafloor seep using shipboard acoustics.

Outcomes: The shipboard echo sounder was able to quantify the flux of methane and oil from the seep site. The plume at this site was divided into two regions - a high rise rate region where it was assumed only gas bubbles had a sufficiently high rise rate to be present, and a lower rise rate region likely to contain oil droplets and gas bubbles. For the end member assumption that all the targets in the droplet rise rate regime were oil droplets flux was between 156 - 341 barrels per day at the 95% confidence interval with a mean of 249 barrels per day. If that same region was comprised solely of methane gas bubbles, flux was 3.84 - 13.7 m^3 /day with a mean of 8.78 m^3 / day. The flux for increasing gas to oil ratios (GOR) were also computed. In order to estimate the GOR from the broadband acoustic backscatter, as outlined in chapters 2 and 3, accurate measurements of the material properties of the oil and gas at the site is required. Measurements of these properties were not available at the time of completion of this thesis.

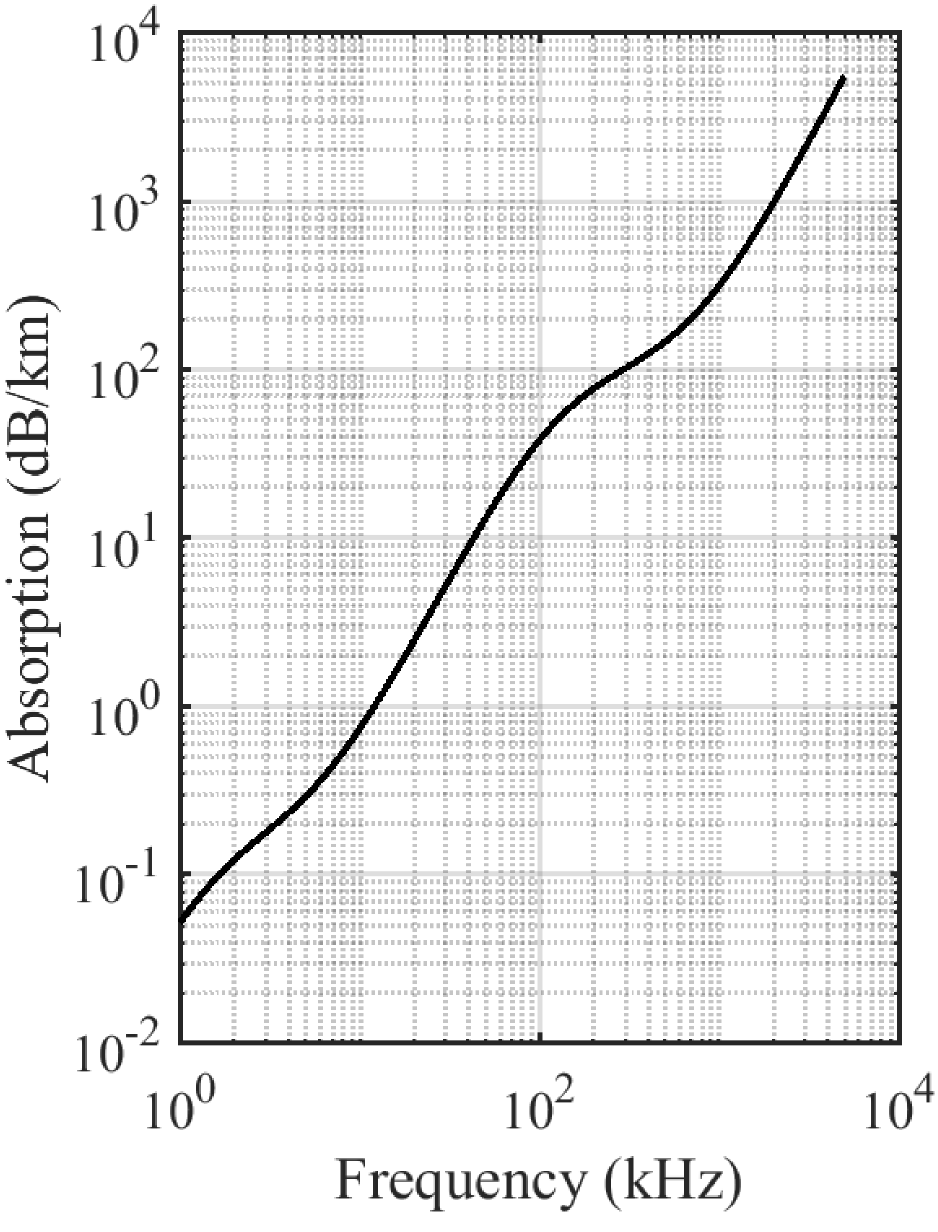

Figure 1.2: The absorption as a function of frequency for sound waves at 20 ° C and 40 meters water depth according to Francois & Garrison (1982).

Chapter 2

Acoustically relevant properties of four crude oils at oceanographic temperatures and pressures

Scott Loranger[1], **Christopher Bassett**[2], **Justin P. Cole**[3], **Bret Boyle**[3], **and Thomas C. Weber**[4]

[1] Department of Earth Sciences, University of New Hampshire, Durham, NH 03824

[2]National Marine Fisheries Service, Alaska Fisheries Service Center, Resource Assessment and
Conservation Engineering Division,Seattle, WA 98115, USA

[3]Department of Chemistry, Colorado State University, Fort Collins, CO, 80526

[4]Department of Mechanical Engineering, University of New Hampshire, 105 Main Street,
Durham, NH 03824

Abstract

Inversions of models of broadband acoustic scattering to detect and quantify weakly scattering targets, such as oil droplets in seawater, require precise knowledge of the physical properties that determine scattering. When the characteristic impedance contrast between a target and the surrounding medium is weak, small differences between the true and modeled impedance can cause significant errors in modeled scattering. For crude oil, currently available empirical models of density and sound speed are derived from measurements made at reservoir conditions (high temperature and pressure), which may not be relevant to oceanographic conditions due to phase changes in the oil. Measurements of the density and sound speed, as well as thermal characterization of phase changes via differential scanning calorimetry, of four crude oils at oceanographically relevant temperatures and pressures were made and compared to a commonly used empirical model for sound speed and density. Significant deviations between the measured and modeled values were found and new empirically fit models were developed. A literature review of sound speed data was also performed, and the new empirical model shows improvement over the commonly used empirical model for both the data measured here and the measurements in the literature.

2.1 Introduction

At the end of the first quarter of 2018, almost 800 offshore drilling rigs were available for hydrocarbon extraction (IHS, 2015). Over the past decade offshore oil production has accounted for approximately 30% of total oil production (U.S. Department of Energy, Energy Information Administration, 2016). Advances in exploration and extraction technology have resulted in expansion of offshore production into new environments. While a majority of this oil is extracted from waters less than 125 m deep, increasingly large portions are extracted from depths in excess of 1,500 m. This production occurs globally with rigs located in areas that cover the full range of oceanographic environments from warm tropical waters to seasonally ice-covered waters in the Arctic.

Many questions exist about the expected environmental impact of spills in the climatically and ecologically diverse environments where drilling occurs. Understanding potential environmental impacts due to spills and developing an appropriate response requires both the ability to quantify the total volume of oil spilled and knowledge of baseline levels of natural oil seepage. For example, the Deepwater Horizon spill released approximately 680,000 tonnes of oil (United States & Coast Guard, 2011). The most recently available estimate of annual flux of liquid hydrocarbons from natural seepage in the Gulf of Mexico is between 80,000 tonnes and 200,000 tonnes of oil and between 200,000 tonnes and 2,000,000 tonnes worldwide (Transportation Research Board and National Research Council, 2003). Liquid hydrocarbon flux from the Deepwater Horizon spill is estimated to have been between 34% and 340% of the global annual flux of oil into the ocean. While any increase above background levels is likely to have an environmental impact, knowledge of the magnitude of a spill relative to background levels is necessary both to inform decision making during spill response and to assess the long-term impact on the environment. Acoustic methods (e.g., Camilli *et al.* (2012), Weber *et al.* (2012)), offer a path toward quantifying both anthropogenically released and naturally occurring liquid hydrocarbons in the ocean, but are limited by the paucity of information describing the physical properties of oil needed for acoustic scattering models at oceanographic conditions. The present work seeks to address this information gap by reporting measurements of oil density and sound speed under pressure and temperature conditions relevant to much of the worlds oceans, and by developing an empirical model for these properties that performs better than existing models for the types of oils studied.

Natural hydrocarbon seepage from the seafloor can take the form of free gas, hydrate-coated gas bubbles, and liquid oil, and occur throughout the worlds' oceans (Judd, 2003; Sahling *et al.* , 2016; Kvenvolden & Cooper, 2003). Seepage associated with free gas (with or without hydrate) is often detected and quantified acoustically, taking advantage of the large impedance contrast between free gas and seawater (Merewether *et al.* , 1985; Greinert *et al.* , 2006; Heeschen *et al.* , 2003; Schneider von Deimling *et al.* , 2011; Römer *et al.* , 2012; Weber *et al.* , 2014). The present study is aimed at the study and assessment of the seepage of liquid oil, such as the seeps reported in the Gulf of Mexico and the Congo Basin (Transportation Research Board and National Research Council, 2003; Crooke *et al.* , 2015; Roberts & Carney, 1997; Sahling *et al.* , 2016; Jatiault *et al.* , 2018). In deep water environments a variety of instrumentation is used for the detection and quantification of oil, however, most of these instruments are limited to short detection ranges on the order of meters, or even centimeters (e.g., fluorometers, mass spectrometers). Given this short detection range it is difficult to accurately evaluate the flux for an entire ocean basin, or even a large spill. Acoustic instrumentation provides the potential for the detection and quantification of hydrocarbons at greater ranges. Active acoustic methods have been used to estimate the flux of oil from deep-water blowouts (Camilli *et al.* , 2012), to detect and quantify oil at ranges of up to hundreds of meters from the instrument (Weber *et al.* , 2012), and to estimate the thickness of oil layers under sea ice (Wilkinson *et al.* , 2015; Bassett *et al.* , 2016; Pegau *et al.* , 2017).

Quantifying oil acoustically, whether present as droplets or in layers, depends on a thorough understanding of the physical properties that determine acoustic scattering. The intensity of acoustic scattering is dependent on the geometry (e.g., the thickness of an oil layer or shape of a droplet) and the mismatch between the characteristic impedance (the product of density and sound speed) of the surrounding water and the target. In previous studies of crude oil researchers have had to make assumptions about the physical properties of oil in order to estimate flux (Weber *et al.* , 2012).

One of the reasons that the acoustically-relevant properties of crude oil (shape, size, density and sound speed) are difficult to quantify is that the term "crude oil" encompasses a wide variety of unrefined liquid petroleum products that are composed of multiple hydrocarbon chains of different molecular weights, in addition to other organic materials. Crude oils are often classified by their American Petroleum Institute gravity, API_g. This dimensionless quantity is related to the specific gravity of the liquid according to $\mathrm{API}_g = \frac{141.5}{\mathrm{SG}} - 131.5$, where SG is the specific gravity of the liquid at 15.56 ° C and 0.1 MPa. By this definition light crudes have an API_g higher than 31.1 °, medium crudes API_g between 22.3 ° and 31.1 °, and heavy to extra heavy crude oils have an API_g less than 22.3 °. The concentration of hydrocarbon chains of differing length and geometry as well as organic material present generally varies based on the origin of the petroleum and oils with similar API_g do not necessarily have the same distribution of hydrocarbon chains and organic materials.

The saturated hydrocarbon chains (also referred to as paraffins, waxes or *n*-alkanes), which generally make up a significant percentage of the mass of crude oil, are prone to crystallization at temperatures and pressures lower than those found in oil reservoirs. As temperature decreases, the temperature at which the saturated hydrocarbons begin to change phase from liquid to solid is referred to as the wax appearance temperature (WAT). In general, as molecular weight of saturated hydrocarbons increases the temperature at which saturated hydrocarbons come out of solution as solids increases (García & Urbina, 2003). The WAT is also determined by the breadth of distribution of paraffins, with wider distributions of carbon chain length resulting in a lower WAT (García, 2000; Ronningsen *et al.* , 1991; Vazquez & Mansoori, 2000) Significant changes to the physical properties of oils can occur below the WAT, and it is important to understand how these phase transitions influence the properties that determine acoustic scattering at oceanographically relevant temperature and pressures.

In this study a review of the measurements of sound speed available in the literature was performed and the results compared to Batzle & Wang (1992), a commonly used empirical model of the physical properties of oil. Samples of four crude oils were then chemically analyzed to quantify the concentration of saturated hydrocarbons and phase changes were identified and quantified by differential scanning calorimetry (DSC) over the relevant temperature range. To adequately characterize oils for acoustic scattering applications, the density and sound speed was measured over oceanographically relevant temperatures (-10 °C to 30 °C). Sound speed was also measured at oceanographically relevant pressures (0 MPa to 13.79 MPa). Finally, these results were also compared to the Batzle & Wang (1992) empirically derived model for sound speed and density of crude oils.

2.2 Literature Review

To evaluate the applicability of empirical models derived from measurements of oils at reservoir temperature and pressure to oceanographic conditions a literature review of available sound speed data was performed. Targeted search criteria returned 985 papers. These papers were further refined by exclusion criteria (Appendix 2.6) designed to eliminate papers with insufficient data for modeling sound speed. For example, papers that did not include temperature and/or pressure of measurements were excluded. Following filtering by the exclusion criteria only nine papers made measurements of the sound speed of crude oil with sufficient data for modeling (Daridon *et al.* , 1998; Ball *et al.* , 2002; Meng *et al.* , 2006; George *et al.* , 2008; Han *et al.* , 2010; Plantier *et al.* , 2008; Chaudhuri *et al.* , 2012; Bassett *et al.* , 2016; Khelladi *et al.* , 2010). Of the measurements in those nine papers only 19.7% were made at oceanographically relevant temperatures and pressures. While models derived from reservoir temperatures and pressures may be relevant for oil exploration, the potential for phase changes in oils at lower temperatures and pressures limits the potential applicability of these models to oceanographically relevant conditions. The available literature also focuses primarily on heavy oils; 70% of measurements at oceanographically conditions fell into this category.

In addition to the potentially limited applicability to oceanographic conditions, many of the available models and equations of state rely on *a priori* knowledge of a wide range of thermodynamic properties of oils (e.g. Gross & Sadowski (2001)). For oil spill responders and researchers, such thorough examinations of oil properties are often unfeasible due to the cost of characterization and limited access to large sample sizes. There are, however, simpler models that require fewer input parameters.

The most widely cited empirical model is Batzle & Wang (1992) (hereafter referred to as BW92) which empirically derives values for the sound speed and density of oil based solely on API_g. Because the focus of BW92 was on reservoir conditions, the authors of BW92 limited their analysis of sound speed and density to data that does not include any phase transitions. Oil density as a function of pressure is determined in BW92 by

$$\begin{aligned}\rho_p = \rho_o &+ (0.00277P - 1.61 \times 10^{-7} P^3)(\rho_o - 1.15)^2 \\ &+ 3.49 \times 10^{-4} P,\end{aligned} \tag{2.1}$$

where ρ_P is the oil density in kg/m^3 at pressure P in MPa, ρ_o is the oil density at atmospheric pressure and 15.56 °C (API_g conditions). Temperature is accounted for according to

$$\rho_{P,T} = \frac{\rho_p}{[0.972 + 3.81 \times 10^{-4}(T + 17.78)^{1.175}]}, \tag{2.2}$$

where $\rho_{P,T}$ is the oil density as a function of pressure and temperature, T, in °C.

Figure 2.1 shows the residuals between BW92 and the sound speed data from seven of the nine papers (RMS error 96.0 m/s). Two of the nine papers (Daridon *et al.* , 1998;

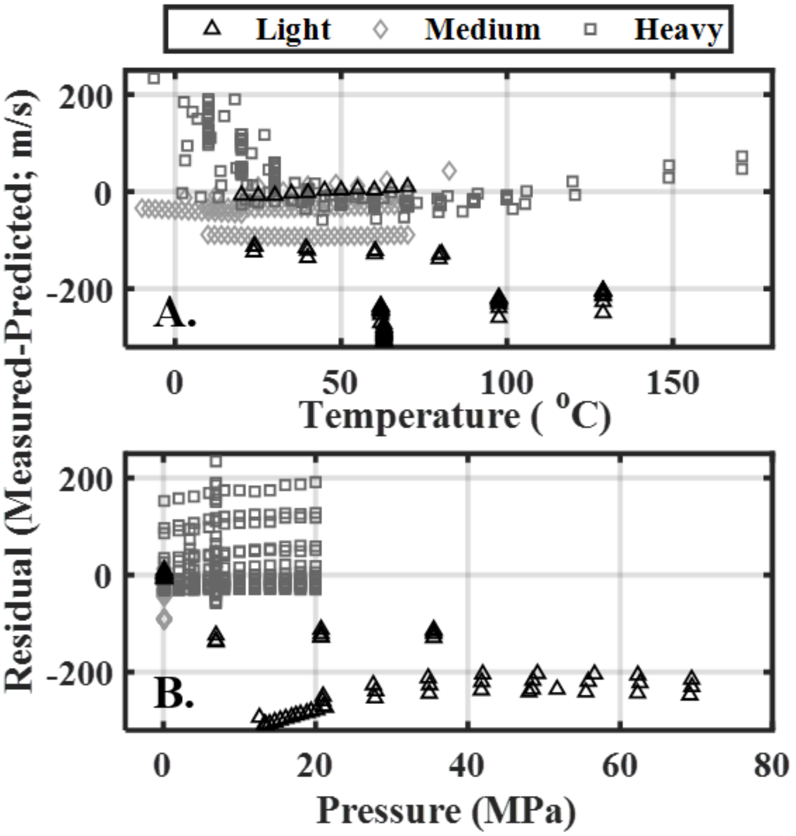

Figure 2.1: Comparison of literature sound speed data and BW92 model as a function of (A) temperature and (B) pressure. Residuals are the difference between the literature sound speed and BW92 in m/s.

Khelladi *et al.* , 2010) did not have API$_g$ or density data for the oils measured and therefore were excluded. BW92 overestimates the sound speed of light oils, RMS error = 211 m/s, underestimates medium and heavy oils, RMS error = 57 m/s and RMS error = 60 m/s respectively. BW92 increasingly underestimates the sound speed of heavy oil as the temperature decreases.

The heavy oil data from the literature shows an exponential increase in sound speed at temperatures below 20 °C that is not predicted by the BW92 model. Han *et al.* (2010) proposed that this exponential increase was due to a phase transition in the oil that they qualitatively referred to as the oil becoming "quasi-solid". The transition to "quasi-solid" state is presumably caused by the crystallization of waxes in the oils, however, the phase transition is not quantified by Han *et al.* (2010).

2.3 Materials and Methods

Samples of four different crude were obtained for analysis. The four oils studied are identified by the geographic region from which they were extracted: Alaskan North Slope ($\text{API}_g = 28.2$ °), Coal Oil Point, Califonia ($\text{API}_g = 22.6$ °), Angolan Bavuca ($\text{API}_g = 17.7$ °), and Angolan Xikomba ($\text{API}_g = 24.4$ °). The abbreviations ANS, COP, BAV, and XIK, respectively, will serve to reference the specific oils when discussing their properties. Based on their API gravities, ANS, COP and XIK are all medium oils while BAV is a heavy oil. All oils were analyzed for saturated hydrocarbon concentration, and thermally characterized by differential scanning calorimetry from -50 °C to 50 °C. Density was measured at ambient pressure for temperatures from -10 °C to 30 °C in 5 °C increments. Sound speed was also measured from -10 °C to 30 °C in 5 °C increments and at pressure from 0.10 MPa to 13.79 MPa in 3.45 MPa increments.

2.3.1 Calorimetry

Differential scanning calorimetry (DSC) was performed on an TA Instruments DSC Q20. DSC analysis reveals phase changes occurring within oil samples by measuring the heat flux required to change the temperature of a sample (Wunderlich, 1990). Deviations in the first derivative of the heat flux as a function of temperature in the test sample reveal the presence of a phase change over a temperature range. If the slope of heat flux as a function of temperature is constant over a region, no phase change is occurring. Measurements were performed by hermetically sealing each sample in an aluminum pan at atmospheric pressure. Samples were then heated to 50 °C, isothermed for 3 minutes, then cooled to -50 °C and isothermed again for 3 minutes. This was performed at 10 °C/min, 5 °C/min, and 3 °C/min.

2.3.2 Saturated Hydrocarbons

Saturated hydrocarbon analysis (SHC) was performed by Alpha Analytical according to EPA SW-846 method 8015D (US EPA, 2007). This method uses Gas Chromatography with Flame Ionization Detector (GC/FID) to determine the concentration of 32 n-alkane hydrocarbons (saturated hydrocarbons with only single covalent bonds) and selected isoprenoids for carbon chains from 9 carbons to 40 carbons in length. The method also reports the total concentration of saturated hydrocarbons along with the total petroleum hydrocarbons.

2.3.3 Density

Density was measured by calibrated hydrometers, FisherSci 11510B and 11510C, according to ASTM D1298-12b. Approximately 250mL of each was oil transferred at room temperature into 300mL ungraduated cylinders and sealed with parafilm. The sealed cylinders and hydrometers were placed in a temperature-controlled incubator, ESPEC BTL-433, which was set to -10 °C. A NIST certified Omega Ultra Precise Platinum RTD temperature probe (PMA-1/8-6-1/2-TS5; range: -100 °C to 250 °C, accuracy: 0.15 °C $\pm$ 0.002 $|T|$, where T is the temperature of measurement) connected to a NIST certified Omega High Accuracy PT100 Input Thermometer (HH804U; accuracy 0.05%$|T|$) was inserted through the parafilm into the XIK sample, which had the highest heat capacity over the temperature range as measured by DSC. Once the incubator temperature was stable, the samples were given 1.5-hours to equilibrate. XIK reached a stable temperature of -9.8 °C after 45 minutes. Samples then sat for an additional 45-minutes to assure that the entire sample reached equilibrium. Temperature inside the incubator was constantly recorded by an RBR solo T Temperature Logger (accuracy ± 0.002 °C) recording at a 1-second sample rate. Hydrometers were placed in each sample and allowed to equilibrate for 30 minutes. Each hydrometer was read and recorded, noting the maximum height of the oil on the hydrometer. Corrections for opaque liquid meniscus and glass expansion/contraction were made according to ASTM D1298-12b. The temperature of the chamber was then set to -5 °C and once the temperature in the chamber was stable, the samples were allowed 1-hour to equilibrate. These steps were repeated to obtain measurements in 5 °C intervals from −10 °C to 30 °C.

2.3.4 Sound Speed

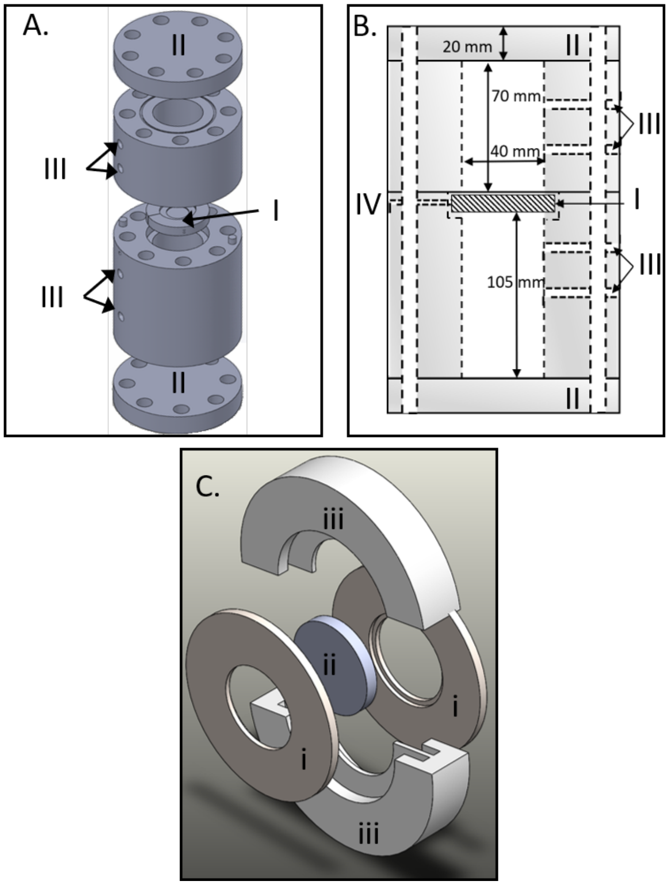

Figure 2.2: (A) Exploded exterior view of sound speed chamber with: (I) The piezoelectric sandwich, (II) the endcaps, and (III) the fill and pressure ports. (B) Cross-sectional view of interior of sound speed chamber with same labeling as (A) with the addition of (IV) the hole through which the wires to the piezoelectric "sandwich" pass. (C) The piezoelectic sandwich. The brass washers (i) are wired to the signal generator, with one washer wired to positive and the other to negative. These washers sit flush against the face of the piezoelectric transducer (ii). The washers and held apart and the entire sandwich held together by the plastic spacers (iii) which also fit flush against the inside of the sound speed chamber. (Color Online).

Sound speed measurements were made using a system modified from the design by Dashti & Riazi (2014). The chamber was vacuum filled to minimize air entrainment in the sample. Sound was generated by a piezoelectric transducer held in the center of two cylindrical stainless-steel chambers (Figure 2.2). The transducer was driven by an Agilent Arbitrary Waveform Generator, which drives an 10V peak-to-peak, five-cycle, 750 kHz pulse that travels bi-directionally through the length of each chamber. No tapering window was applied to the signal. The waves are reflected by the end caps and then return to the transducer. A Tektronix TBS 1102B Digital Oscilloscope records the voltages associated with the reflected waves. Data was recorded over a 100 μs window encompassing only the first and second returns (excluding the transmit pulse and higher multiple returns) with a sample rate of 2.5 MHz. The Tektronix TBS 1102B Digital Oscilloscope records 16 individual wave forms, coherently averages them together to reduce noise and outputs that average as a single waveform. For a given temperature and pressure 100 of the outputted waveforms were recorded.

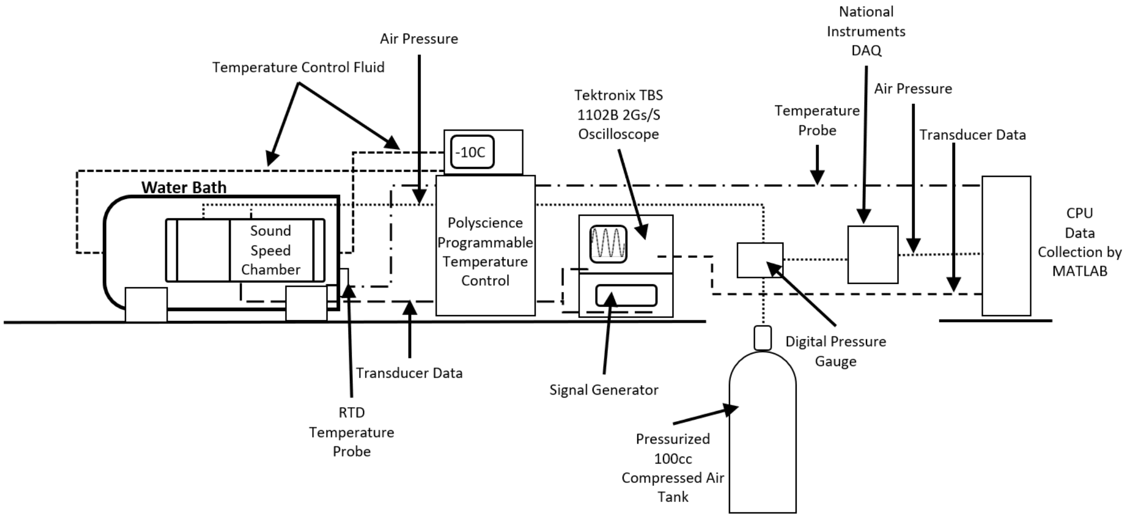

Figure 2.3: Diagram of sound speed chamber temperature and pressure control and data collection.

Figure 2.3 diagrams the environmental control and data recording set-up for sound speed measurements. The internal pressure of the system was controlled by a precision pressure control valve connected to a SCUBA tank. Pressure data was recorded by a NIST certified Omega Digital Pressure Gauge (DPG409-3.5KG) with and accuracy of 0.08% of the full scale (24 MPa). Temperature was controlled by placing the chamber in an insulated PVC housing connected to a PolyScience Programmable Temperature Controller. A 50/50 mixture of water/ethylene glycol was used as the bath fluid to permit temperatures as low as −50 °C. Temperature in the housing was recorded by a NIST certified Omega Ultra Precise Platinum RTD temperature probe (PMA-1/8-6-1/2-TS5) connected to a NIST certified Omega High Accuracy PT100 Input Thermometer (HH804U). Data recorded by the oscilloscope was recorded in MATLAB. During temperature transitions, MATLAB was used to calculate real-time sound speed using a single recorded waveform every ten seconds. When the sound speed was constant (not changing by more than 0.1 m/s) over a 10-minute period, it was determined that the oil had reached equilibrium with the fluid bath.

The path length difference between the two sides of the sound speed chamber was calibrated using ASTM Type 1 deionized water, as detailed in Appendix 2.7. The calibration evaluated the effects of temperature and pressure on the path lengths and found that there was no significant relationship between the estimates of $\Delta\ell$, the difference in path length between the sides of the chamber, and temperature, pressure or both. The mean path length difference for all temperatures and pressures is 69.934mm ± 0.245mm (95% CI). For a 1500 m/s fluid this equates to an uncertainty in sound speed of ± 5.3 m/s.

Sound speed, c, is calculated by dividing the mean path length difference by the difference in arrival time for the two waves according to,

$$c = \Delta\ell/\Delta t, \tag{2.3}$$

where the propagated uncertainty for σ_c was calculated according to

$$\sigma_c = \pm c\sqrt{\left(\frac{\sigma_\ell}{\ell}\right)^2 + \left(\frac{\sigma_{\Delta t}}{\Delta t}\right)^2}, \tag{2.4}$$

where σ_ℓ and $\sigma_{\Delta t}$, are the standard deviations of the length and time difference respectively. The 95% confidence intervals of all sound speed measurements was between 5.0 m/s and 5.4 m/s. Results agree well with the Belogol'skii *et al.* (1999) model for pure water (RMS error

2.5 m/s, Figure 2.4).

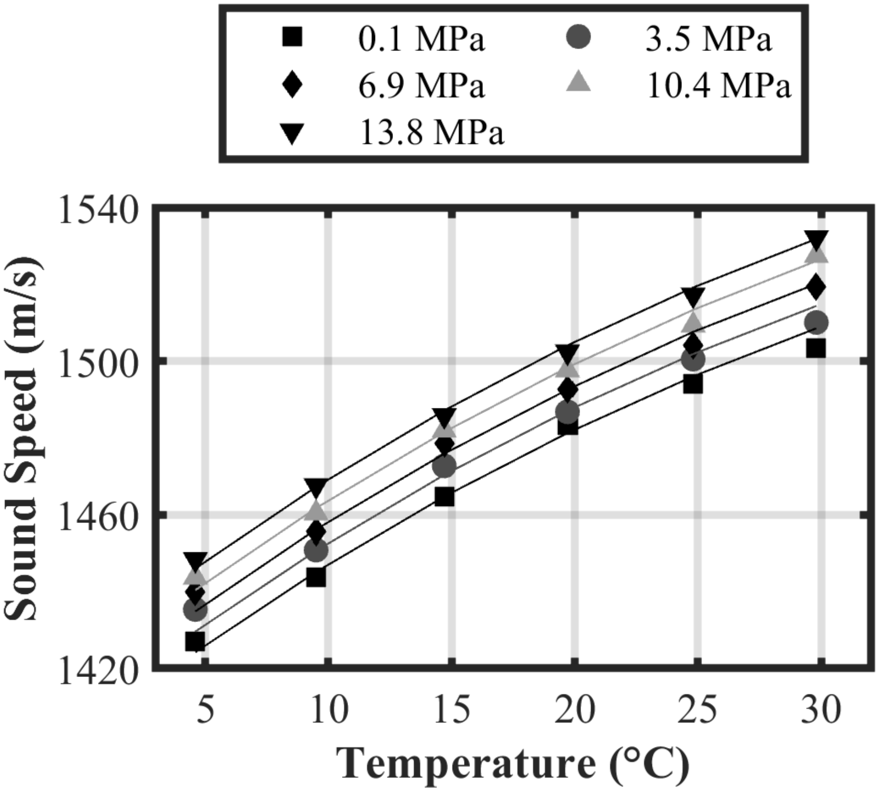

Figure 2.4: Sound speed of type 1 deonized water measured (markers) compared to Belogol'skii *et al.* (1999) (lines).

Equation 2.3 was used to calculate sound speed for ANS, XIK, BAV and COP, using the temperature and pressure independent estimate of $\Delta\ell$ from the DI water calibration corrected for thermal expansion at the temperature of a given measurement.

2.4 Results and Discussion

2.4.1 Calorimetry

Differential scanning calorimetry (DSC) results are summarized in Table 2.1. DSC did not detect any phase changes in BAV over the measurement range, but did detect phase change in ANS, XIK and COP. Enthalpy is the integrative measure of the magnitude of a phase transition and was the highest for COP and lowest for ANS. The phase transition is bounded by the WAT (the temperature at which waxes begin to form) and the onset of melt (the value below which no more waxes are solidifying). Peak melt temperature is the temperature at which enthalpy is greatest in the transition. While COP has a higher overall enthalpy, the majority of its phase transition occurs below the oceanographically relevant range. XIK has the next highest enthalpy, and its phase transition occurs over almost the entire measurement range. ANS has a much lower enthalpy, and while the transition is within the measurement range, the overall magnitude of the transition is much smaller than XIK and COP."

2.4.2 Saturated Hydrocarbons

XIK has the highest concentration of saturated hydrocarbons, relative to total petroleum hydrocarbons, followed by COP, ANS, and BAV (Table 2.1). When comparing this data to the DSC results above, oils that have a phase transition have higher percent saturation, the ratio of saturated hydrocarbons to all hydrocarbons. XIK has the highest total saturated hydrocarbon concentration at all molecular weights (Figure 2.5). This broad distribution of saturated hydrocarbons and higher concentration of longer chain waxes results in the higher enthalpy. While COP has a high concentration of saturated hydrocarbons, the concentration of high molecular weight paraffins is lower than XIK, contributing to the lower phase transition temperature. ANS has a lower percent saturation, and fewer long chain saturated hydrocarbons contributing to the lower total enthalpy. Since BAV only has a small number of low molecular weight paraffins, it possesses a weak phase transition at very low temperatures.

Table 2.1: Phase transition and percent saturation for four crude oils. Phase transition data is from DSC analysis. Percent saturation was determined by saturated hydrocarbon analysis.

	ANS	XIK	COP	BAV
Enthalpy (J/g)	0.58	3.26	4.70	n/a
Onset of Melt (°C)	-13.7	-18.3	-40.9	n/a
Peak Melt Temperature (°C)	3.08	7.62	-11.19	n/a
Wax Appearance Temperature (°C)	14.68	20.66	19.60	n/a
Percent Saturation (%)	11.2	16.5	13.1	0.8

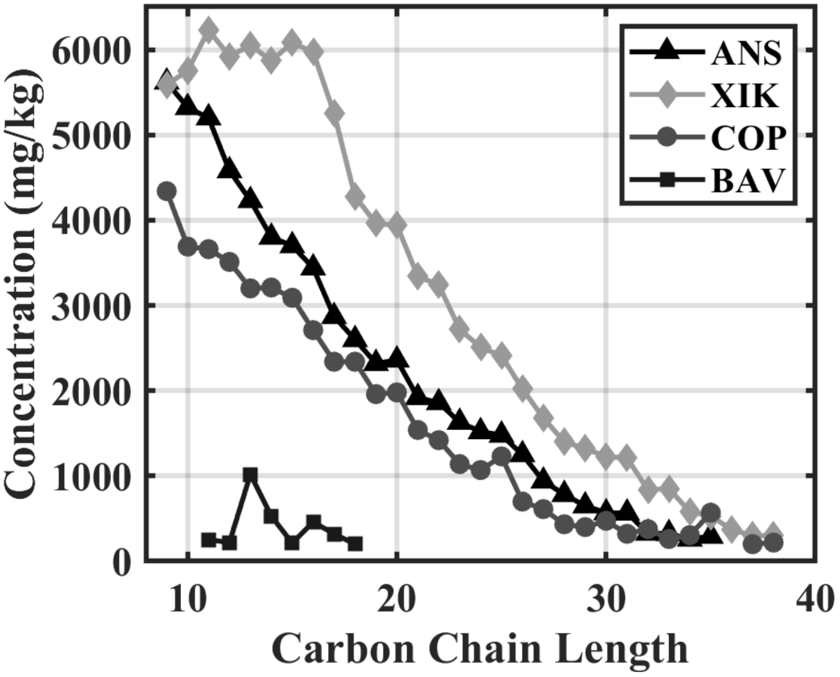

Figure 2.5: Concentration of saturated hydrocarbons by carbon chain length.

2.4.3 Density

All oils have an inverse relationship between temperature and density (Figure 2.6). BAV, COP and ANS all have similar relationships between temperature and density, regardless of the presence of a phase transition as detected by DSC. Below the WAT, XIK transitioned from liquid to higher density waxy solid, with an increasingly rapid rise in density with decreasing temperature. Below the peak melt temperature the viscosity of XIK was too high for measurements of density to be made (the hydrometer was effectively stuck in place).

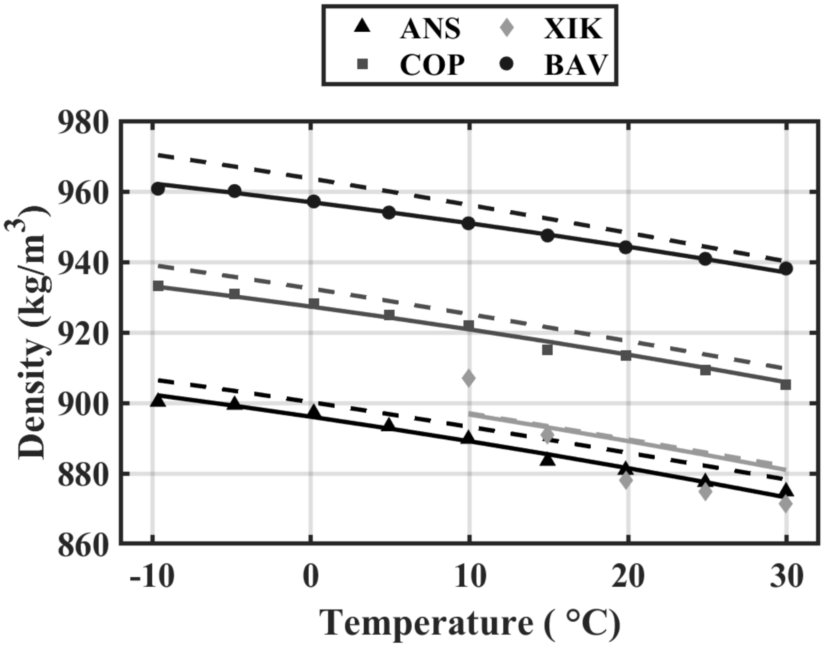

Figure 2.6: Density results comparing measured (markers), empirically derived model in this study (solid lines) and BW92 (dashed lines).

API$_g$ for use in the BW92 model was calculated by fitting a second order polynomial to the data to get the density at 15.5 °C. BW92 slightly over-predicts the density for all oils (Figure 2.6), except for XIK at 10 °C, where BW92 under-predicts density. The RMS error for the BW92 model for all oils is 25.9 kg/m^3.

To improve on BW92, an empirically fit model was developed. A stepwise regression was computed using input parameters API$_g$ and temperature. Coefficients were calculated for both input parameters as well as linear and quadratic combinations of these parameters.

Any input parameters or combinations with correlation p-values less than 0.05 were rejected (Draper & Smith, 1998). XIK was excluded from the modeling analysis: in order to accurately model the relationship between density and temperature for oils with a significant phase transition similar to that seen for XIK would require more than two measurements below the phase transition temperature. Therefore, this empirically derived model is applicable only to oils with either no phase transition over the modeled range (BAV), or a very weak transition over the modeled range (ANS and COP). The result is a six-term equation for the density of crude oil as a function of temperature with inputs ρ_0, density (kg/m^3) at API conditions (15.56 °C and 0.1MPa), and T, the temperature in °C,

$$\rho = C_0 + C_1 T + C_2 \rho_o + C_3 T \rho_o + C_4 T^2 + C_5 \rho_o^2, \tag{2.5}$$

with coefficients in Table 2.2.

Table 2.2: Coefficients for empirically derived model in this study for density and sound speed.

Coefficient	Density	Sound Speed
C_0	-995.02	2148.4
C_1	-2.011	-4.1630
C_2	3.249	3.548
C_3	1.527×10^{-3}	-50.25
C_4	-3.405×10^{-3}	2.0402×10^{-2}
C_5	-1.255×10^{-3}	8.7438×10^{-3}
C_6	–	0.95175

The new model has RMS error equal to 2.0 kg/m^3, including XIK (1.1 kg/m^3 excluding XIK).

2.4.4 Sound Speed

Sound speed decreases with increasing temperature and decreasing pressure. The three medium oils all have similar sound speeds, while BAV has a sound speed on the order of 75 m/s higher for all temperature and pressures (Figure 2.7). At 5 °C BAV showed exceptionally

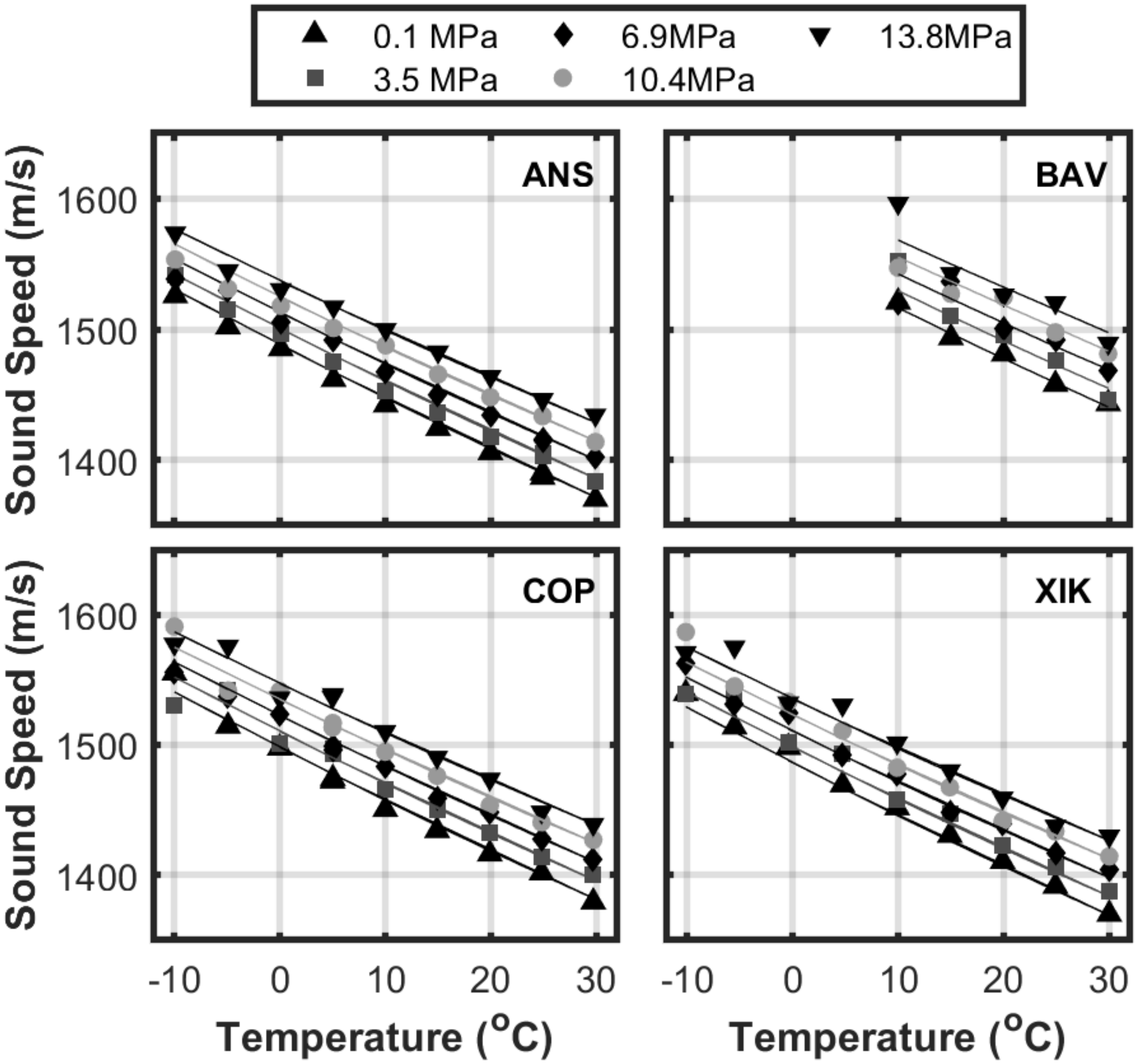

Figure 2.7: Measured sound speed (markers) and empirically derived model from this study (lines).

high signal attenuation, to the point that there was no detection from the longer side of the chamber and a very low amplitude signal from the short side. Below 5 °C no echoes were detected. Due to the low signal to noise ratio, no reliable measurements of sound speed were possible below 10 °C for BAV.

BW92 predicts significant deviations from the measured sound speeds, RMS error 42.5 m/s and largest magnitude residual -74.6 m/s (Figure 2.8). A new empirical model was derived using a stepwise regression analysis. Regression coefficients were calculated for all input parameters (temperature, sound speed and API_g) as well as all linear and quadratic combinations of parameters. Any coefficients with regression p-values greater than 0.05 were excluded. The result is a seven-term model with inputs T, temperature in °C, P, pressure in MPa, and API$_g$,

$$\begin{aligned} c =&C_0 + C_1T + C_2P + C_3API \\ &+ C_4TP + C_5T^2 + C_6API^2 \, , \end{aligned} \tag{2.6}$$

with coefficients listed in Table 2.2. The RMS error for the new model is 7.4 m/s with maximum residual 28.2 m/s (Figure 2.8). This empirical model provides a better fit than BW92 over oceanographically relevant temperatures and pressures while still only including temperature, pressure and API$_g$ as input parameters.

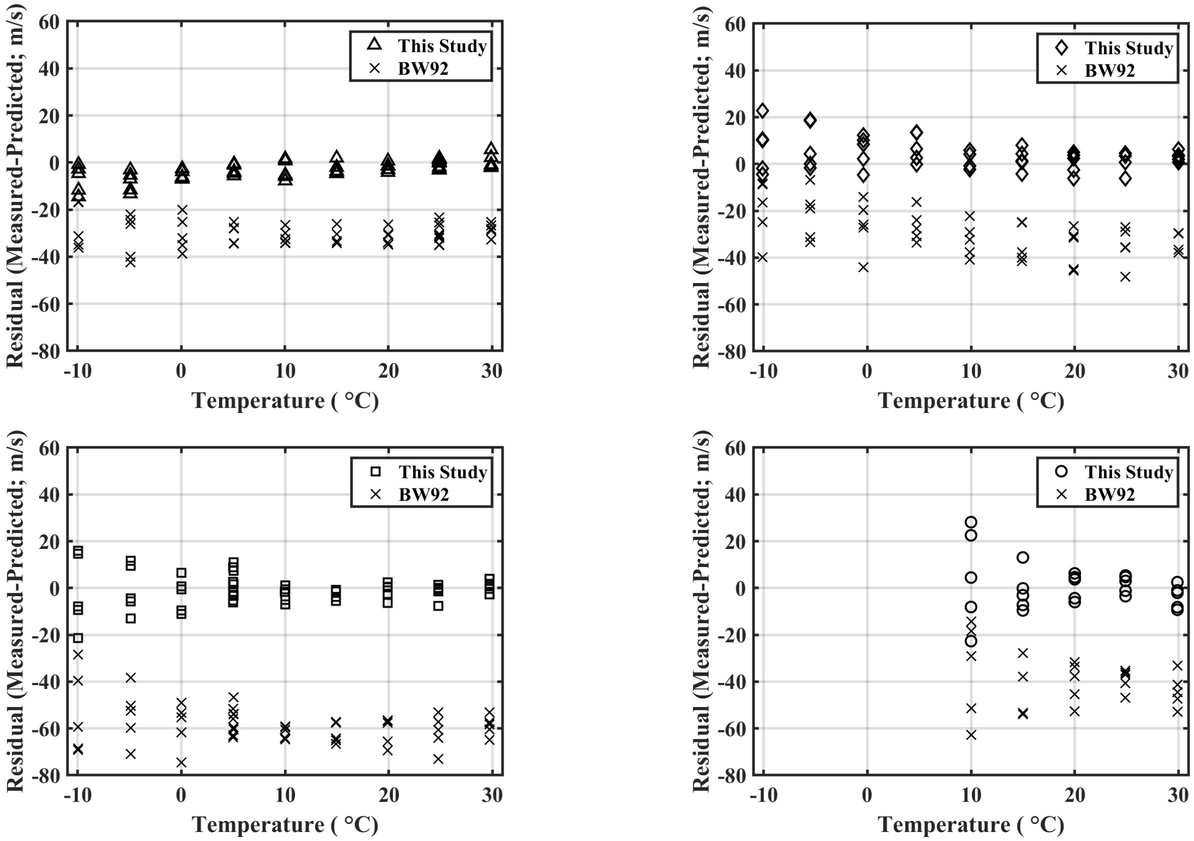

Figure 2.8: Residuals for sound speed measured in the present work and newly derived model compared to residuals for sound speed measured in the present work and BW92. A.) ANS, B.) XIK, C.) COP, D.) BAV.

The empirical model derived in this study was compared to literature values for oceanographically relevant temperatures and pressures. The new empirical model is a marginally better predictor of sound speed for literature data, RMS error 76.3 m/s compared to 84.9 m/s for BW92. The literature data includes three measurements of light oils whose API gravities are much higher than the oils analyzed here (two measurements of API_g 37.7 ° and one of 45.6 °). The empirical model derived here is a poor predictor of sound speed for light oils, due to lack of light oil measurements. If the three measurements of light oils are removed from both BW92 and the new empirical model, the RMS error for the new model improves to 55.1 m/s while BW92 RMS error stays relatively unchanged, 85.2 m/s. For medium and heavy oils, the new empirical model is a better predictor of sound speed (Figure 2.9).

2.4.5 Implications for Scattering Models

The broadband acoustic backscatter from a 2 mm radius spherical COP droplet at 15 °C and ambient pressure (0.1 MPa) is analyzed here as an illustrative example of the importance of well-constrained acoustic properties. A wide range of frequencies are used to detect and quantify oil from shipboard instruments in the 100's of kHz range to MHz imagining sonars. The example here focuses on the lower, shipboard frequencies. The sound speed for COP oil measured in this study at 15 °C and 0.1 MPa is 1434.3 ±5.03 m/s. Using the empirically derived model in this study, the sound speed is 1438.4 ±14.8 m/s, while the BW92 model provides a sound speed of 1491.9 ±85 m/s. The density of COP measured in this study at these same conditions is 915.0 kg/m^3, for the empirical model in this study the density is predicted to be 917.4 ±2.24 kg/m^3 and the empirical BW92 model predicts 921.5 ±12.0 kg/m^3. Figure 2.10 shows the results of the Anderson (1950) scattering model for a 2 mm radius spherical droplet using the three different acoustic impedances - measured in this study, predicted by the empirical model derived in this study and according to the BW92 empirical model. The surrounding medium was assumed to be seawater with density = 1026 kg/m3 and sound speed 1473 m/s. The newly derived model is a better predictor of the peak

TS as well as the frequency range of the null, two important factors for inverting scattering models to predict droplet properties.

Another example of the importance of well-constrained acoustic properties is in modeling the reflection of sound generated in the water column and reflected from oil layers. Such scattering is most accurately modeled as a three-layer problem, however for brevity and simplicity it is modeled here as a two layer-problem where the oil and water both occupy a half space. When the interface between the fluids is acoustically smooth, the reflected energy is a function of the mismatch in the acoustic impedance. As the difference in acoustic impedance across the water-oil interface approaches zero, little energy is reflected. At oceanographically relevant temperatures and pressure the conditions under which the detection of oil layers is difficult depends on the acoustic properties of both the water and oil. Figure 2.11 shows modeled reflection coefficients from an acoustically smooth water-oil interface over a range of API gravities and water temperatures. Modeled oil temperature are at equilibrium with the water. Local minima occur from -2 °C to 15 °C for oils with API gravities between 15 ° - 37 °. Notably, at the lowest modeled temperatures when conditions would be consistent with an oil layer under ice light and heavy oils would be more difficult to detect than medium oils. The minima for medium oil occurs at higher temperatures, up to 12 °C, and is mostly likely to occur for oil at the sea surface when ice is not present. In the case of a three-medium problem, the oil-water layer would effectively disappear, and reflection would occur from the fluid/ice or fluid/atmosphere interface. These results demonstrate the importance of adequately constrained acoustic properties when setting thresholds for detecting and quantifying crude oil in ocean environments.

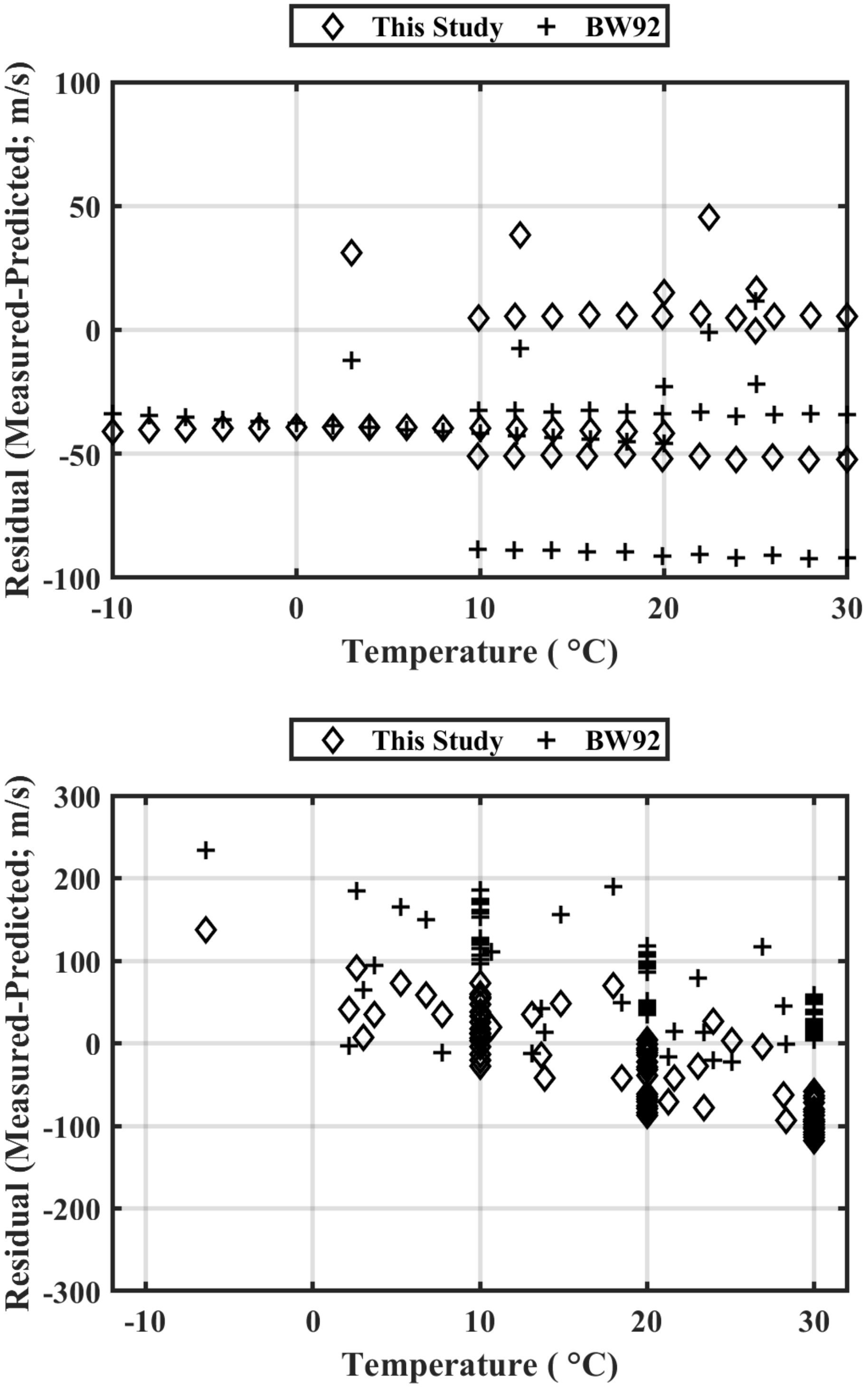

Figure 2.9: Residuals between literature values for sound speed and the empirical equation from this study as well as BW92. A.) Medium Oil, B.) Heavy Oil.

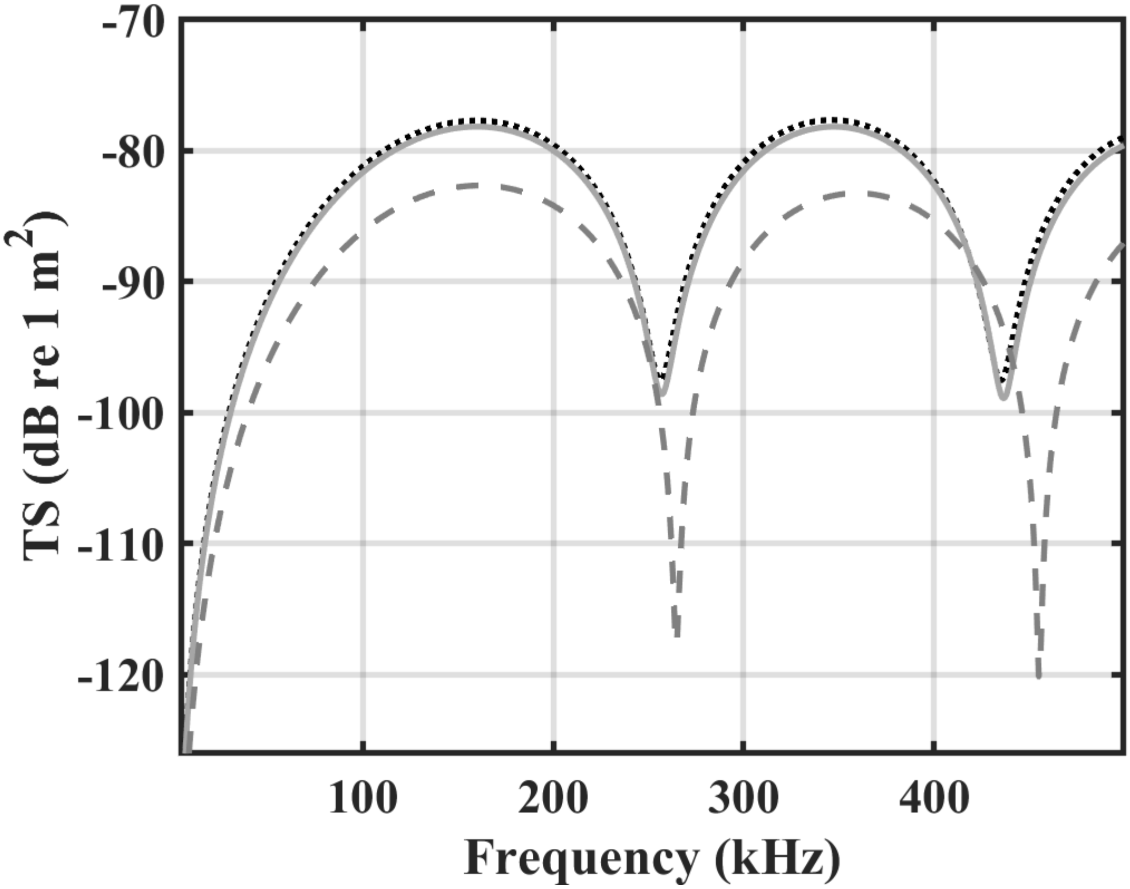

Figure 2.10: Acoustic scattering predicted by Anderson (1950) using the measured impedance (dotted line), impedance predicted by BW92 (dashed) and impedance predicted by the empirically derived model in this study (solid line) for a COP droplet at 25 °C.

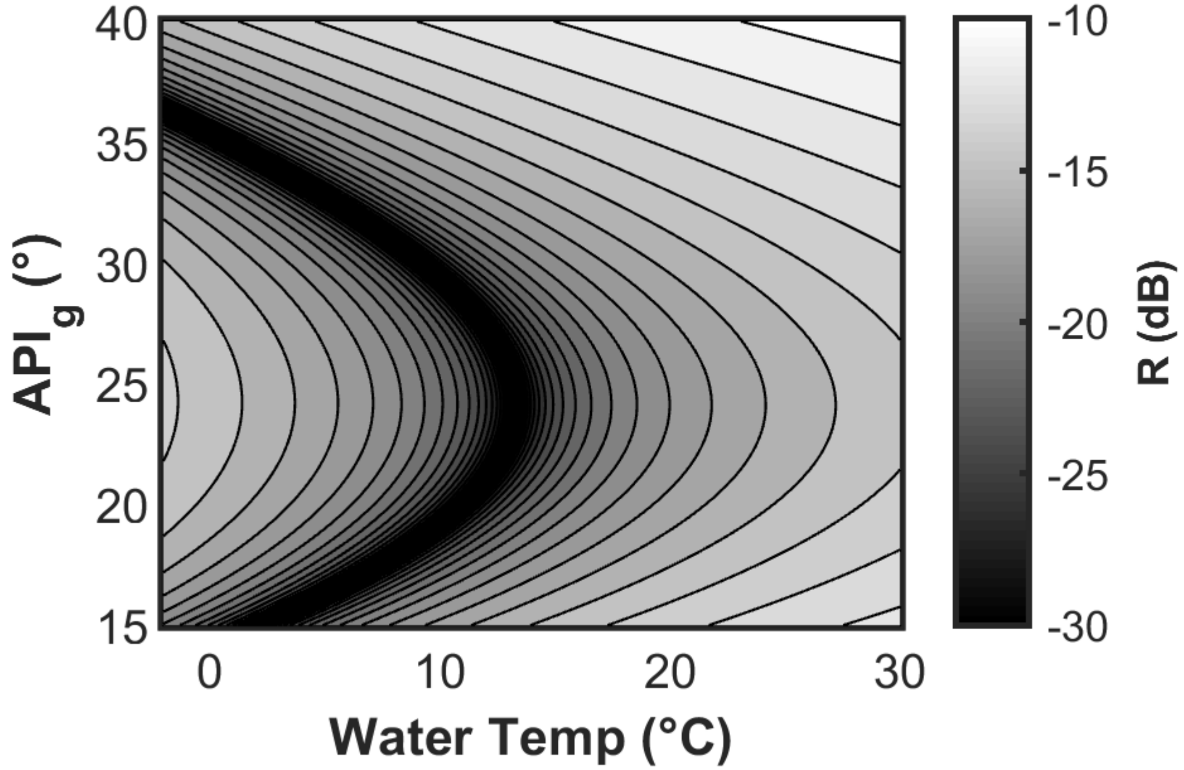

Figure 2.11: Reflection coefficients for an acoustically smooth water-oil interface as a function of API gravity and temperature assuming that the oil and water temperatures are at equilibrium (Clay & Medwin, 1977). The acoustic properties of the oil are determined by the empirically derived model (Eqs. 2.5 and 2.6) at atmospheric pressure and the water has a salinity of 30 psu. Local minima in the reflection coefficient curve highlight the combinations of oil and water properties that would make the detection of thin oil layers difficult using acoustic scattering techniques.

2.5 Conclusions

The empirical models derived in this study are limited in sound speed to medium and heavy oils, and in density to oils that do not have a large phase transition in the temperature range. More data is need, including phase transition information, in order to expand this model and determine its applicability to light oils and to oils where waxes become solid over the range of interest.

Active acoustic measurements are a powerful tool that can be used along with other techniques to detect and quantify oil in oceanographic applications. While acoustic scattering techniques may be used to detect oil droplets or oil layers without *a priori* knowledge of the acoustic properties of the oil, quantification of volumes in oil layers and fluxes associated with oil droplets is contingent upon acoustic properties that are adequately constrained. Complex models requiring a wide range of physical and thermodynamic oil properties as inputs may improve accuracy, however, researchers and oil spill responders often do not have the time or sample volume to obtain a wide range of properties. We propose a simpler empirical model, requiring only the API_g and environmental conditions (temperature and pressure) to predict density and sound speed at environmental conditions relevant to oil in the ocean. Our model shows significant improvement over the relevant environmental conditions compared to BW92, which was derived from conditions relevant to oil in subsurface reservoirs. When direct measurements of sound speed and density are unavailable, this empirical model can be used to improve the accuracy of predictions of acoustic scattering used to estimate oil flux in the water column and oil layer thickness, both of which are crucial to determining the natural background levels of hydrocarbons in the environment and the environmental impact of anthropogenic spills.

The literature review provided examples of where heavy oils showed an exponential increase in sound speed at low temperatures due to what was qualitatively described as a transition to a “quasi-solid” state (Han *et al.* , 2010). By contrast, the present study found that solidification of waxes can occur in medium oils, but that phase transition did not significantly impact the sound speed as a function of temperature over the range studied here. However, the present study focused on a relatively narrow temperature range and it may be the case that the sound speed changes exponentially with temperature over a broader range. The empirical model derived here is more applicable to oceanographically relevant conditions than a model derived from higher temperature and pressure measurements. More samples of heavy, medium and light crudes that show solid wax formation over the relevant temperature range are needed to fully determine how this transition affects sound speed and to model how the transition impacts density.

Acknowledgement

We thank Alpha Analytical Environmental Testing Laboratory for providing the saturated hydrocarbon analysis; John Mousette from JW Precision Co. Inc. and Paul Lavoie from University of New Hampshire for fabrication of the sound speed chamber; Peter Vrolijk and John Blum from Exxon Mobile and David Valentine from University of California Santa Barbara for providing the crude oil samples. The work was supported by the National Oceanic and Atmospheric Administration (Grant # NA15NOS4000200). The scientific results and conclusions, as well as any views or opinions expressed herein, are those of the author(s) and do not necessarily reflect the views of NOAA or the Department of Commerce. Reference to trade names does not imply endorsement by the National Marine Fisheries Service, NOAA.

2.6 Appendix A: Literature Review

A review of primary scientific literature was performed using the Web of Science database using the following terms: “sound speed” OR “speed of sound” OR “sound velocity” OR “velocity of sound” OR “wave velocity” OR “wave speed” OR “seismic properties”) AND (Oil OR Hydrocarbons OR Crude OR Petroleum OR “pore fluid”). These keywords were designed to capture any study that either directly measures, or uses other physical parameters to determine, the speed of sound in crude oil, as well as any models for the sound speed of oil based on other physical properties. The search returned an initial pool of 985 papers. These papers were screened for relevance to the topic of interest. Papers were then screened and excluded if:

1. They did not contain measurements of sound speed or derivation of sound speed from other physical properties
2. Sound speed measurements were not associated with a density, API_g or API_g based classification (Light, Medium, Heavy or Extra Heavy).
3. Experiments were performed using hydrocarbons not derived from or composed of crude petroleum.
4. Mineral oils were excluded.
5. The same data was used in multiple papers. In this case only the earliest publication of those same results was recorded.
6. They were not studies of hydrocarbon mixtures of greater than three different length hydrocarbon chains
7. Papers did not include either temperature or pressure data
8. They did not report sufficient data for inclusion in analysis
9. Oil-in-water mixtures were excluded.
10. Seismic studies were excluded.

2.7 Appendix B: Sound Speed Chamber Deionized Water Calibration

The sound speed chamber was calibration using ASTM Type I deionized water. Sound speed measurements were made at 5 °C increments from 5 °C to 30 °C and 3.4 MPa increments from 0.1 MPa to 13.8 MPa. Each recorded time series from the transducer was filtered using a fifth order Butterworth bandpass filter to decrease out-of-band noise.

Analytical forms of each waveform were then normalized to their peak value and auto-correlated (Figure 2.12). The difference in time between the peak of the correlation from the echo from the shorter side (t_1) and the peak of the correlation from the longer side (t_2) gives the difference in time of flight for each pressure and temperature, $\Delta t_{T,P}$, for the two chambers ($\Delta t_{T,P} = t_2 - t_1$). The sound speed of distilled water, c_{ref}, was modeled according to Belogol'skii *et al.* (1999) and was used to calculate the difference in path length between the two sides of the chamber for each temperature and pressure according to

$$\Delta \ell'_{P,T} = c_{\text{ref}}(\Delta t_{P,T}), \tag{2.7}$$

Each difference in path length is then corrected for the difference in length of each section of the chamber caused by thermal expansion,

$$\Delta \ell_{P,T} = \Delta \ell'_{P,T} - 2\ell_2 \boldsymbol{\alpha_L}(T-23) - 2\ell_1 \boldsymbol{\alpha_L}(T-23)\,, \tag{2.8}$$

where $\ell_2 = 110$ mm is the length of the longer chamber at 23 °C according to the design, $\ell_1 = 70$ mm is the length of the shorter chamber at 23 °C according to the design and $\boldsymbol{\alpha_L} = 16.6 \times 10^{-6}\, m/m/K$ is the coefficient of thermal linear expansion for stainless steel (ASTM A276 - 98b, 2017). The estimates of $\Delta \ell_{P,T}$ were then regressed against temperature, pressure and temperature and pressure combined.

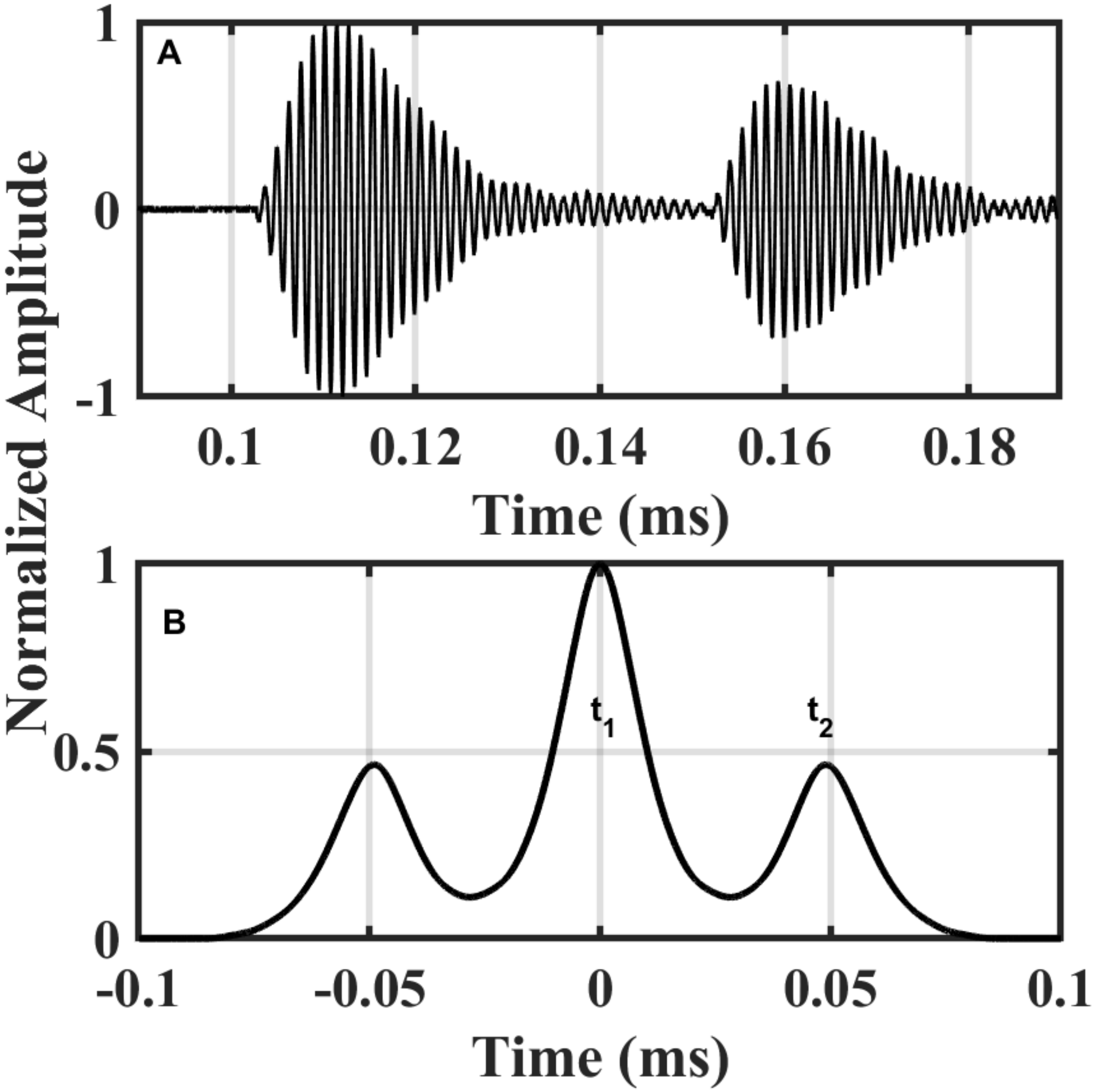

Figure 2.12: (A) Raw waveform showing the return from the shorter side and the lower amplitude return from the second side. (B) Autocorrelation of (A) with times used to calculate sound speed labeled.

Chapter 3

Broadband acoustic scattering from oblate hydrocarbon droplets

Scott Loranger[1], **Geir Pedersen**[2], **and Thomas C. Weber**[3]

[1] Department of Earth Sciences, University of New Hampshire, Durham, NH 03824

[2]Norwegian Research Centre, P.O. Box 6031, Bergen 5892, Norway

[4]Department of Mechanical Engineering, University of New Hampshire, 105 Main Street, Durham, NH 03824

Abstract

Improved in-situ quantification of oil in the marine environment is critical for informing models of fate and transport, and for evaluating the resiliency of marine communities to oil spills. Broadband acoustic backscatter has been used to quantify a variety of targets in the water column; from fish and planktonic organisms to gas bubbles and oceanic microstructure, and shows promise for use in quantifying oil droplets. Quantifying water column targets with broadband acoustic backscatter relies on accurate models of a target's frequency dependent target strength, a function of the target's acoustic impedance, shape and size. Previous acoustic quantification of oil droplets has assumed that droplets were spheres. In this study, broadband (100.5 - 422 kHz) acoustic backscatter from individual oil droplets was measured and the frequency dependent target strength compared to a model of acoustic scattering from fluid spheres and to two models for more complex shapes. Droplets of three different crude oils, two medium oils and one heavy oil, were quantified and all droplets were oblate spheroids. The impact of the deviation from sphericity on the accuracy of each model was determined. If an inversion of the model for spherical droplets were used to estimate flux from acoustic observations, errors in the predicted volume of a droplet were between 30 % to 50 %. The heavy oil also showed deviations in predicted volume of 20 % to 40 % when using the two models for more complex shapes.

3.1 Introduction

Improved acoustic methodologies for the detection and quantification of oil in the marine environment are necessary for determining the extent and fate of oil spills, as well as the natural background level of oil in the marine environment. During the Deep Water Horizon (DWH) spill, high frequency (above 1 MHz) acoustic systems were deployed to the leaking well site to determine the flux of oil and gas from the wellhead (Camilli *et al.* , 2012). Lower frequency (200 kHz) ship mounted echo sounders were also used to detect oil from a greater range and to determine flux in the water column (Weber *et al.* , 2012). Both methods estimated a similar concentration of oil, however, they also relied on assumptions about the size and shape of droplets to determine flux from acoustic scattering.

Droplet size is crucial to determining fate and transport of oil in the marine environment, as it is a key component in determining both droplet rise rate and bioremediation rate. As droplet size decreases surface area to volume ratio increases exposing more oil to hydrocarbon consuming bacteria. In fact, oil spill responders take advantage of the enhanced bioremediation provided by smaller droplets by adding chemical dispersants to decrease droplet size. Estimates of the initial diameter of droplets released from the DWH spill range from 300 μm to 10 mm for droplets formed without the addition of chemical dispersants, and from 10 μm-1000 μm for droplets formed after the addition of dispersants (Socolofsky *et al.* , 2011; North *et al.* , 2015; Zhao *et al.* , 2014). The wide range of droplet size estimates is due in part to a lack of *in-situ* verification of droplet size. Broadband acoustics offer the opportunity to quantify oil droplet size *in-situ*, which in turn will improve determination of the fate of oil in the marine environment.

Broadband acoustic backscatter has been used to differentiate between plankton and turbulent microstructure (Lavery *et al.* , 2010), to quantify bubbles under breaking waves (Medwin & Breitz, 1989; Terrill & Melville, 2000; Vagle & Farmer, 1992), and as an aid for classifying fish species (Holliday, 1972; Thompson & Love, 1996; Stanton *et al.* , 2010). The quantification and classification of these targets relies on well constrained models of frequency dependent target strength (TS), a measure of the strength of backscatter that is a function of the target's size, shape and contrast in sound speed and density between the target and the surrounding medium. TS is the ratio of the backscattered intensity to the incident intensity and is independent of the incident power. The broadband TS of weak scatterers, such as oil droplets, has a characteristic peak and null structure where the amplitude of peaks and frequency of nulls are used to classify targets. Modeling the amplitude of peaks and frequency of nulls requires precise knowledge of the sound speed and density of oil, which at oceanographic conditions, can be difficult to determine due to phase changes in oil. The sound speed and density are predictable for some oils at oceanographically relevant temperatures and pressures (Loranger *et al.* , 2018). If the impedance and shape are known, inversions of scattering models for individual scatterers can be used to determine the remaining model input: size.

Jech *et al.* (2015) and Stanton & Chu (2000) review a variety of acoustic scattering models of increasing complexity, both computationally and in terms of the target shape. Weber *et al.* (2012) used a simplified model of acoustic scattering that assumes droplets were spherical to determine oil flux during the DWH Spill. However, oil droplets can vary in shape depending on the size and physical properties of the oil (Clift *et al.* , 1978; Pedersen, 2016). The degree to which oil droplets deviate from the spherical shape assumed by Weber *et al.* (2012) and the impact of the deviations on acoustic scattering, and ultimate predictions of droplet size, is unknown.

In this study broadband (100.5 kHz - 442 kHz) acoustic backscatter from crude oil droplets in freshwater was measured. Droplets of varying material properties, size and shape were generated by a novel droplet making device and the size and shape were measured by a calibrated machine visions camera. The material properties of the oils was measured and described in (Loranger *et al.* , 2018). The measured TS of droplets was compared to three increasingly complex models of scattering from fluid targets; Anderson (1950) for simple spheres, the Distorted Wave Born Approximation (DWBA)(Stanton *et al.* , 1998), an estimation of scattering for more complex shapes, and finally the Boundary Element Method (BEM)(Okumura *et al.* , 2003; Francis & Foote, 2003), a more computationally complex model for complex shapes, to determine how well each model agrees with empirically measured broadband backscatter.

3.2 Materials

Three different crude oils, identified by geographic origin of the sample, were used in this study: Alaska North Slope (ANS), Angolan Xikomba (XIK) and Angolan Bavuca (BAV). Table 3.1 lists the properties of these oils at the experimental temperature, 21.6 °C and atmospheric pressure, based on measurements by Loranger *et al.* (2018). Viscosity was measured by a rotational viscometer (Brookfield Ametek LVDV1M Viscometer, ASTM D7867-13 (2013)). Surface tension for each oil in deionized water and in simulated seawater (Salinity 35 ppt; Kester *et al.* (1967)) was measured by the Center for Complex Fluids at Carnegie Mellon University (Alvarez *et al.* , 2010) at 21.0 ±0.5 °C. The acoustic experiments were conducted in a 12 m x 18 m x 6 m (length x width x depth) freshwater tank at the University of New Hampshire. Properties of the tank water are listed in Table 3.1. Temperature was measured by an RBRsolo T Temperature Logger (accuracy ± 0.002 °C) and sound speed calculated according to Bilaniuk & Wong (1993). A nominal value of 998 kg/m^3 was assumed for density.

Table 3.1: Physical properties of the fluids used in this study. All values are for atmospheric pressure and 21.6 °C. Interfacial tension values are for oil and simulated sea water / deionized water

	ANS	XIK	BAV	Tank Water
API Gravity (°)	28.2	24.2	17.7	N/A
Density (kg/m^3)	878.5	875.7	942.2	998
Sound Speed (m/s)	1399.7	1403.5	1471.1	1487.2
Viscosity (cP)	17.1	31.3	650.0	0.9
Surface Tension (mN/m)	20.3/26.2	24.0/23.5	27.1/26.7	N/A

3.3 Models

The experimental results are compared to broadband backscattering modeled by three commonly used models; the modal solution derived by Anderson (1950), the distorted wave Born approximation (DWBA)(Stanton *et al.* , 1998), and the Boundary Element Method (BEM)(Okumura *et al.* , 2003; Francis & Foote, 2003). The Anderson model assumes that targets have spherical symmetry, while the DWBA can be used for more complex shapes, however it assumes that targets are weakly scattering. The BEM is valid for complex shapes and for a variety of boundary conditions; however, it is much more computationally expensive than the Anderson (1950) model and the DWBA. For all of the models it is assumed that the material properties are homogeneous throughout the droplet and the effects of dispersion and attenuation within the target are negligible.

The droplets in this experiment rose to the surface with their axis of symmetry perpendicular to the water surface and the incident and reflected waves parallel to the axis of symmetry. Experimental results were limited to droplets that were within 3 degrees of the maximum response angle of the transducer, and therefore the maximum deviation from normal incidence is three degrees, a deviation that does not significantly impact model results. The DWBA and BEM were computed for droplets that are oblate spheroids and the Anderson model for equivalent volume spheres.

The subscripts t and w below indicate that the variable is in reference to the target or surrounding medium respectively. The details of the models below are intended to provide a physical insight into the model methodologies and are in no way meant to be a rigorous derivation.

3.3.1 Anderson Sphere Model

Taking advantage of the symmetry of a spherical target, Anderson (1950) calculated the exact modal solution for sound scattering from a plane wave incident on a fluid sphere, and it has been used to predict scattering from many different targets assumed to be spheres including euphausiids and oil droplets Kristensen & Dalen (1986); Weber *et al.* (2012). The exact solution for the backscattering form function, f_{bs}, in the far field from a fluid filled sphere is,

$$f_{bs} = -\frac{i}{k_w}\sum_{n=0}^{\infty}(-1)^n(2n+1)A_n\,, \tag{3.1}$$

where k_w is the acoustic wave number of the surrounding medium and

$$A_n = \frac{-1}{1+iC_n}\,, \tag{3.2}$$

where

$$C_n = \frac{[j_n'(k_t a)y_n(k_w a)]/[j_n(k_t a)j_n'(k_w a)] - gh[y_n'(k_w a)/j_n'(k_w a)]}{j_n'(k_t a)j_n(k_w a)]/[j_n(k_t a)j_n'(k_w a)] - gh}\,. \tag{3.3}$$

j_n is the spherical Bessel function of the first kind of order n where a prime denotes the derivative with respect to the argument, y_n is the spherical Neumann function where a prime denotes the derivative with respect to the argument, k is the acoustic wavenumber of the target, a is the radius of the sphere, g is the density ratio (ρ_t/ρ_w), h is the sound speed ratio (c_t/c_w), ρ is the density, c is the sound speed of target and the subscripts t and w denote the target and surrounding medium respectively.

The target strength (TS) is related to f_{bs} by,

$$TS = 10\log_{10}(|f_{bs}|^2) \tag{3.4}$$

The Anderson model in this study was evaluated by taking the sum of the first $ka+20$ terms $(n = ka+20)$ which provides for convergence of the solution relative to a precision of 0.1 dB (Jech *et al.* , 2015).

3.3.2 Distorted Wave Born Approximation

Scattering from a plane wave incident on the target can be approximated by the distorted wave Born approximation (DWBA). The born approximation assumes that a target is weakly scattering and that therefore the total field at a point is approximately equal to the incident field. The DWBA has been used to predict the scattering from a variety of biological targets including copepods, euphausiids, krill and squid Chu *et al.* (1993); Jones *et al.* (2009); Stanton & Chu (2000). For the DWBA, scattering is calculated with the magnitude of the incident acoustic wave number determined by the sound speed of the scatterer (hence the term distorted). The DWBA is valid over all ranges of angles of incidence (Stanton *et al.* , 1998; Stanton & Chu, 2000). The general form of the Born approximation is a volume integral derived by Morse & Ingard (1968),

$$f_{bs} = \frac{k_w^2}{4\pi} \iiint_v (\gamma_\kappa - \gamma_\rho) e^{2i(\vec{k}_i)\bullet\vec{r}_v} dv \,, \tag{3.5}$$

where γ_κ is the compressibility parameter $((\kappa_t - \kappa_w)/\kappa_w)$ and κ is compressibility $((\rho c^2)^{-1})$, γ_ρ is the density parameter $((\rho_t - \rho_w)/\rho_t)$, $(\vec{k}_i)$ is the acoustic wavenumber vector, r_v is the position vector of the volume and v is the volume of body. The distorted wave born approximation replaces $(\vec{k}_i)$ with the wavenumber vector whose magnitude is determined by the material properties of the target $(\vec{k}_i)_t$ (Stanton *et al.* , 1993). Stanton *et al.* (1998) solve the volume integral for an object whose cross section is circular at every point along the lengthwise axis (i.e. a cylinder or disk) where the radius of the cross section can vary as a function of position on the lengthwise axis (a deformed cylinder or disk) and the orientation of the cross section can also vary as a function of position (a bent cylinder or disk Figure 3.1). For an unbent cylinder, such as an oblate spheroidal oil droplet, the volume integral reduces to a line integral,

$$f_{bs} = \frac{k_w}{4} \int_{r_{\vec{pos}}} (\gamma_\kappa - \gamma_\rho) e^{2i(\vec{k}_i)_t\bullet\vec{r}_{pos}} \times a \frac{J_1(2k_t a \cos\theta)}{\cos\theta} |dr_{\vec{pos}}| \,, \tag{3.6}$$

where $\vec{r}_{pos}$ is the position vector of the axis of the cylinder, J_1 is the spherical Bessel function of the first kind of order 1 and θ is the angle of orientation of the body relative to the direction of the incident wave. The droplets in this study had an unbent axis of symmetry parallel to the incident and reflected waves resulting in end-on ensonification for all cross-sections. For end-on ensonification, where the incident wave is in the same direction as r_{pos}, θ is equal to 90 ° (0 ° is broadside incidence) and the dot product $(\vec{k}_i)_t \bullet \vec{r}_{pos}$ reduces to $|k_t||r_{pos}|$. The discontinuity in the integral at 90 ° can be approximated by calculating the limit of f_{bs} as it approaches 90 ° from both sides.

The integral solution was approximated with a rectangle rule, using cross-sections of thickness 1μm, less than 1/1000 of a wavelength for all frequencies.

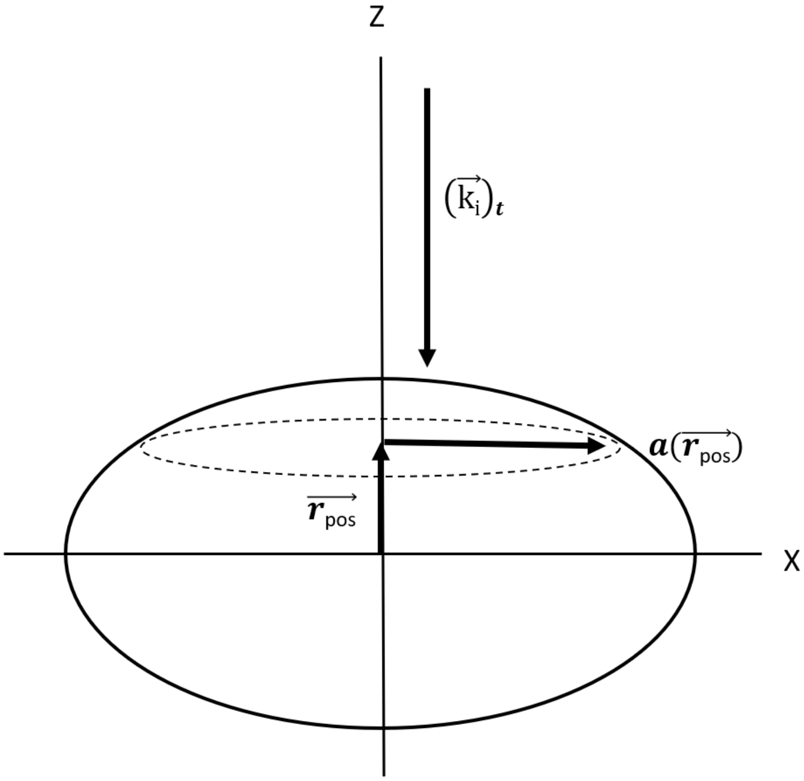

Figure 3.1: Geometry of incident wave, $(\vec{k}_i)_t$, and an oblate oil droplet for end-on ensonification for use in the DWBA. $r_{\vec{pos}}$ is the position vector and $a(r_{\vec{pos}})$ is the radius of cylinder of thickness $dr_{\vec{pos}}$, at position $r_{\vec{pos}}$.

3.3.3 Boundary Element Method

The Boundary Element Method (BEM) breaks the surface of a target into a finite number of geometric shaped elements (Figure 3.2). It can be used to approximate scattering of an incident plane wave from spheres and from more complex shapes. BEM has previously been used successfully to model backscatter by gas and weakly scattering targets, including bubbles, fish swimbladders, and swimbladder like shapes (see e.g. Francis & Foote (2003); Okumura *et al.* (2003)).

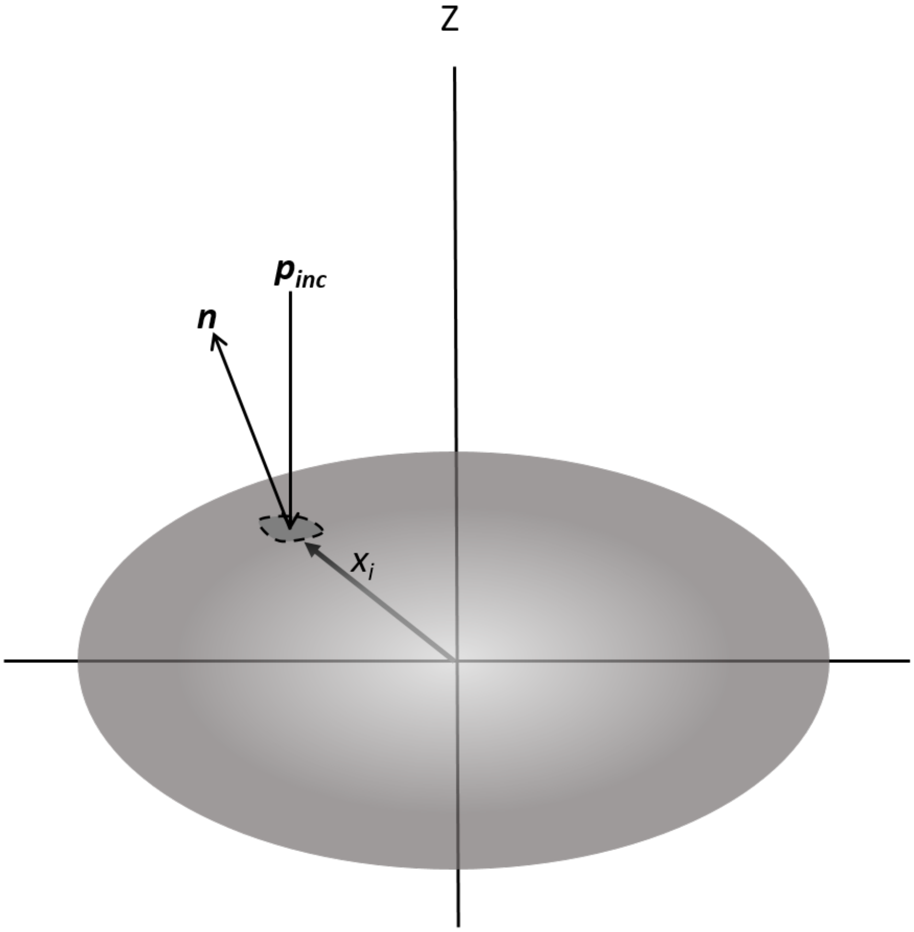

Figure 3.2: Geometery of incident wave, p_{inc}, on a droplet Ω with surface Γ. Γ is divided into surface elements a location $mathbfx_i$ with vector normal to the element surface n. The incident wave travels parallel to the axis of symmetry of the oblate spheroidal droplet.

For computing the BEM, three dimensional models of droplets were generated using Matlab and the surface of the models was meshed using Netgen v5.3. The number of mesh nodes per acoustic wavelength exceeded 10 for the shortest wavelengths used during simulation. Convergence tests were performed with varying mesh densities performed prior to the simulations. The acoustic wave equation was solved using an computational boundary element platform (BEM++ v 2.0.3; Śmigaj *et al.* (2015)) for an plane wave incident on the droplet and traveling parallel to the radius of symmetry of the droplet.

A droplet Ω with surface Γ and sound speed, c_t and density ρ_t was embedded in an infinite homogeneous isotropic medium with sound speed, c_w and density ρ_w. Propagation of time harmonic acoustic waves are described by the Helmholtz equation for the interior and exterior of the droplet as

$$\Delta p(\mathbf{x}) + k_{int}^2\, p(\mathbf{x}) = 0, \quad \forall\, \mathbf{x} \in \Omega \tag{3.7}$$

$$\Delta p(\mathbf{x}) + k_{ext}^2\, p(\mathbf{x}) = 0, \quad \forall\, \mathbf{x} \in R^3 \backslash \Omega \tag{3.8}$$

where k_t and k_w are the acoustic wavenumber of the droplet and embedding medium respectively, and p($\mathbf{x}$) is the pressure perturbation of the element on the droplet surface at $\mathbf{x}$. Boundary conditions on the surface Γ are given by

$$\gamma_0^{int}\, p(\mathbf{x}) = \gamma_0^{ext}\, p(\mathbf{x}), \quad \forall\, \mathbf{x} \in \Gamma \tag{3.9}$$

$$\rho_{int}^{-1}\, \gamma_1^{ext}\, p(\mathbf{x}) = \rho_{ext}^{-1}\, \gamma_1^{ext}\, p(\mathbf{x}), \quad \forall\, \mathbf{x} \in \Gamma \tag{3.10}$$

The backscattered pressure $p_{scat}(\mathbf{x})$, generated by an incident plane wave described by $p_{inc}(\mathbf{x})$ incident on the droplet, fulfills the Helmholtz equation for the embedding domain,

$$p(\mathbf{x}) = p_{scat}(\mathbf{x}) + p_{inc}(\mathbf{x}), \quad \forall\, \mathbf{x} \in R^3 \backslash \Omega \tag{3.11}$$

with the scattered pressure field fulfilling Sommerfeld's radiation condition at infinity

$$\lim_{|x|\to\infty} = \left[\frac{\partial}{\partial|x|}p_{scat}(x) - ik_{ext}p_{scat}(x)\right] = 0. \tag{3.12}$$

The integral-equation formulations utilized for the simulations of backscatter from the oil droplets are described by Kleinman & Martin (1988) which is free from the irregular frequency problem. This implementation was validated for weakly scattering targets against the prolate spheroid modal series model (PSMS) computed from 12 to 200 kHz (Jech *et al.* , 2015).

BEM++ uses Adaptive Cross Approximation to speed up the solution of the Helmholtz equation.

3.4 Experimental Methods

3.4.1 Droplet Generation

A droplet making device was designed and built for the generation of individual oil droplets of a consistent and adjustable size (Figure 3.3). The droplet maker consisted of an oil reservoir and needle manifold. A compressed air source was connected to the reservoir via a precision air pressure regulator that supplied sufficiently high pressure to push the viscous oil through the reservoir and needle manifold while being kept low enough to release only individual droplets. Minor adjustments to air pressure allowed for control of the release rate of droplets, limiting the rate so that only a single droplet was present in the water column at any given time.

Droplet size was controlled by the size of needles through which oil was released. The interior radius of the needle, pressure applied by the air source and surface tension of the oil determined the droplet size. Larger needle size resulted in larger droplets for an individual oil, while an oil with higher surface tension resulted in larger droplets emanating from the same needle size compared to a lower surface tension oil. A circular manifold of four different sized needles was connected to the oil reservoir. A drive belt connected the needle manifold to a stepper-motor that was controlled from the surface, allowing the user to change the needle size without recovering the droplet making system from the bottom of the tank. Once aligned, oil could only pass through the selected needle.

The filled reservoir and needle rosette, along with the imaging system (see below) were deployed to the bottom of the 12 m x m 18 x 6 m (length x width x depth) fresh water tank at UNH and allowed at least an hour to equilibrate with the tank. Tank temperature was measured by two RBR temperature probes, one at the surface and one attached to the droplet making system. Once released, droplets rose to the surface of the tank where they were collected for eventual disposal.

3.4.2 Imaging System

As the droplets were released from the needle manifold the size was measured by a calibrated machine vision camera (Edmond Optics EO-1312 1.3 Megapixel Color USB 3.0 Camera with C Series 25mm Fixed Focal Length Imaging Lens; Figure 3.3). The machine vision camera had a very narrow depth (1.5 cm between the front and back focal planes) of field so that objects in focus in the foreground were of similar size to objects in focus the background. The camera sat atop a platform that allowed the camera to be moved in two-dimensions parallel to the tank bottom. Two stepper motors controlled from the surface of the tank were used to position the camera. One motor was used to focus the fixed focal length camera by moving the camera toward and away from a target and the other motor is used to move the camera in the perpendicular direction to position the target in the center of the frame.

The camera system was calibrated by focusing on a 3-D printed checkerboard of two-millimeter boxes that filled the camera frame, positioned at the same range from the camera face as the oil-releasing needle. The camera position was adjusted so that the target was in the center of the focal plane. The camera recorded a still-frame image of the checkerboard

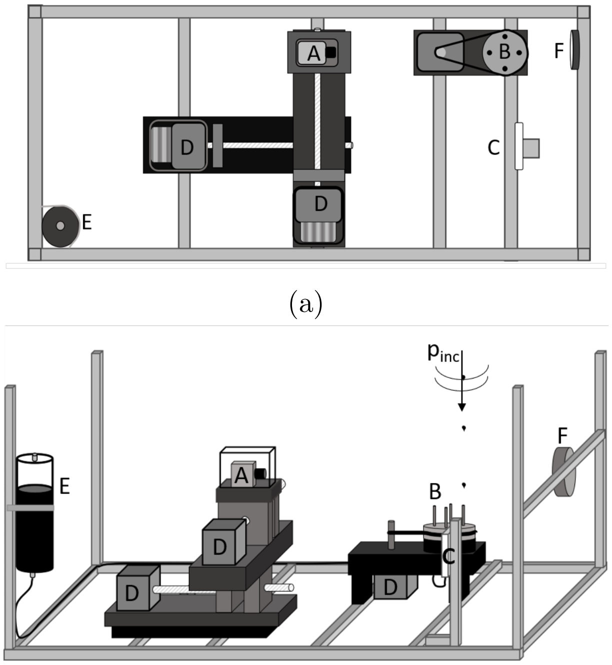

(a)

(b)

Figure 3.3: a. Top down view and b. side on perspective of droplet making and imaging system. 1: High definition machine vision camera. 2: Needle rosette. 3: Calibration target. 4: Stepper motors. 5: Oil Reservoir. 6. LED light panel. The stepper motors on the camera platform move the camera in two dimensions parallel to the bottom of the platform. The camera is moved perpendicular to the face of the calibration target to focus on the plane containing the target and needle. The camera is then moved from the calibration to the target to the needle rosette. p_{inc} indicates the direction of the incident wave from the echo sounders at the tank surface.

at the bottom of the tank, and the vertical and horizontal pixel size of the image was calibrated and analyzed to check for image distortion. The mean pixel size for both vertical and horizontal pixels was found to be 0.0476 ± 0.0006 mm/pixel and no distortion in the rectified images was detected. The error in the pixel size measurement (± 0.0006 mm/pixel) was equal to the difference in pixel size between the foreground and background focal planes (0.0012 mm/pixel).

An LED light panel backlit the droplets to maximize the contrast between droplets and the background. Individual frames from the recorded video were analyzed in MATLAB. Each frame containing a droplet was converted to gray scale, normalized to the maximum intensity

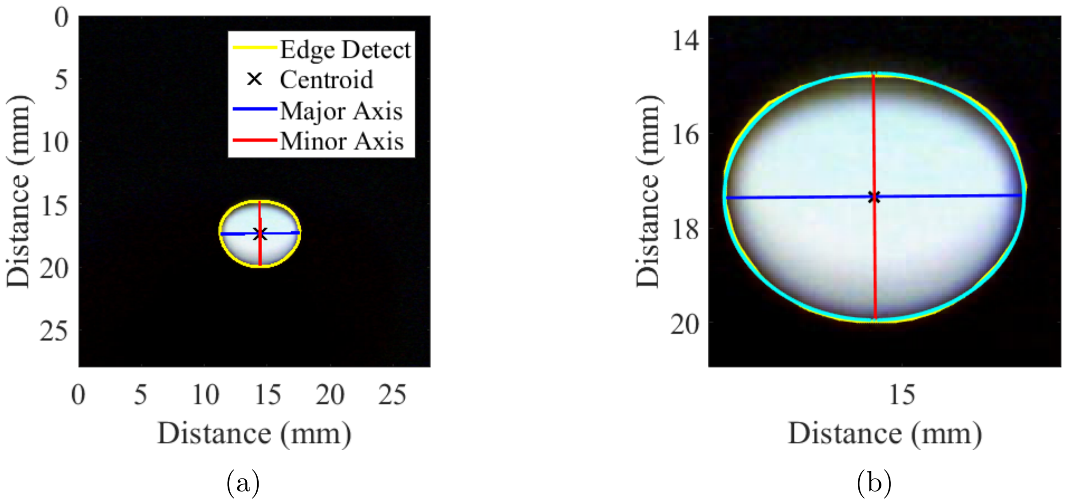

Figure 3.4: a: Image processing example for oil droplet. Droplets are released at a rate so that only a single droplet is in frame. b: Zoom in on the droplet from A with the outline of the assumed oblate spheroid shape overlaid (cyan line) showing how well the oblate shape fits the edge detect (yellow line)

in the frame and then converted to a binary image with threshold of 0.17. Droplets were defined by finding components with a connectivity of eight pixels. The boundary, centroid, major radius, minor radius, and orientation of the radii were then estimated for each droplet (Figure 3.4). Images containing droplets were manually scrutinized to remove erroneous detections (e.g., where the droplet was too far to the side of the frame to be adequately characterized, another object was in frame, or some other anomalous issue resulted in an inadequate characterization of a droplet).

The calibration of the imaging system was verified using opaque black spherical beads. Individual beads were manually dropped through a syringe and fell through water in the focal plane of the camera. Three or four frames were captured for each bead. The major and minor radius for each frame containing a bead was calculated using the above method, and the three or four measurements of each bead averaged together. The major and minor radii calculated by the imaging system were then compared to measurements made by a Mitutoyo PH-A14 Horizontal Profile Projector, in air. Two different bead size ranges were used. The major radius of the larger calibration spheres varied from 1.024 to 1.247 mm (0.910 to 1.081

mm minor radius) and the smaller spheres had a major radius range of 0.616 to 0.694 mm (0.539 to 0.673 mm minor radius), according to the Projector. For all targets the RMS error between the camera and microscope measurements of the major and minor radii was 0.028 mm (a little over half a pixel), and there was no relationship between error and target size.

3.4.3 Broadband Acoustic System

Three Kongsberg split-beam, piston-type transducers, an ES120, ES200 and ES333, were deployed at the surface of the UNH fresh-water tank inside of an oil collection ring. Each of the three transducers has a 7° (1-way) beam pattern at its center frequency (120 kHz, 200 kHz and 333 kHz). The transducers were connected to Kongsberg EK80 wide band transceivers (WBTs) enabling broadband transmission and reception on the three echo sounders. One millisecond linear frequency modulated (LFM) pulses were sequentially transmitted from each transducer with bandwidths covering 95-150 kHz, 160-250 kHz and 280-450 kHz. The WBTs apply a Tukey window to the transmit signal, resulting in tapered regions within the transmitted frequencies. The low SNR in the tapered region resulted in the exclusion of those frequencies from analysis. The ratio of the tapered bandwidth to total transmitted bandwidth was 0.20, 0.13 and 0.11 for the ES120, ES200 and ES333, respectively. Data analysis was restricted to frequencies not in the tapered region: 100.5-145.5, 166.5-244.5 and 290-442 kHz for the ES120, ES200 and ES333 respectively. The transducers were calibrated according to the method described by (Demer *et al.* , 2015). Transducers were positioned directly above the droplet making system so that droplets were ensonified from above as they rose to the tank surface.

The waveforms from the four quadrants recorded by the WBTs were summed and match filtered using an idealized transmit signal (Weber & Ward, 2015). Droplets were identified in the echogram and the Fourier transform computed for 250 samples around each droplet, avoiding the transmit pulse and bottom return. The resulting frequency resolution for the ES120 and ES200 was 500 Hz and 1 kHz for the ES333. The frequency domain results were range corrected for spherical spreading and frequency dependent absorption (Francois & Garrison, 1982).

3.5 Results

3.5.1 Droplet Size

An average of 4.5 video frames were recorded for each droplet. The major and minor radius were measured for each frame and averaged together for each droplet in the same manner as the bead calibration. The radius of a sphere of equivalent volume was calculated for each frame from the major and minor radii and averaged together in the same manner.

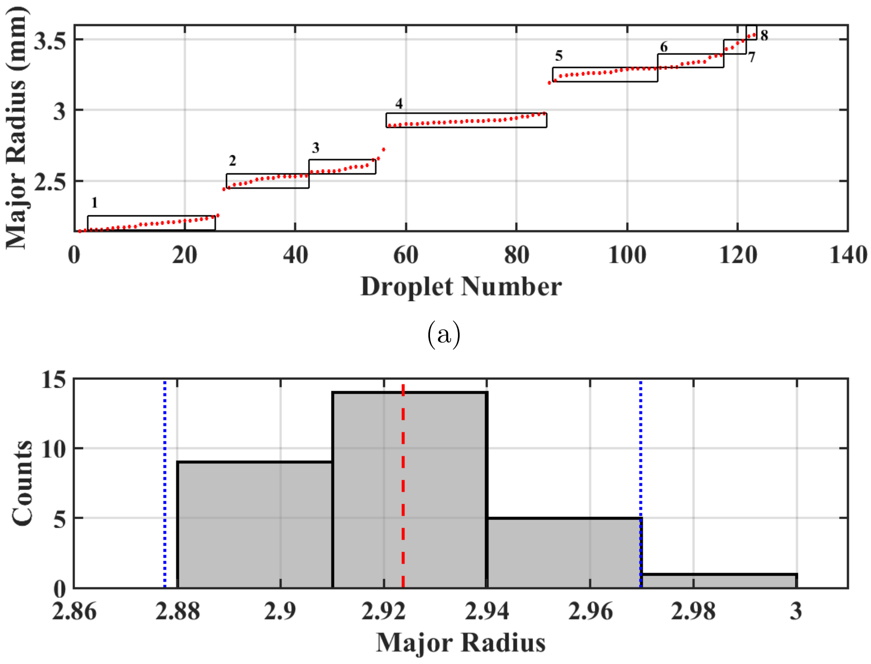

(a)

(b)

Figure 3.5: Grouped major radius results for XIK. a. Sorted major radii for all droplets (red circles) organized into 100μm wide groups (black boxes) with group number labeled, showing the uneven distribution of radii across the size range and within groups. b. Distribution of radii measurements in group four showing the approximately normal distribution of droplets within a group. The mean (red dashed line) and 95% confidence intervals (blue dotted line) are shown.

Droplet size was not evenly distributed across the range of sizes. There are four main divisions of droplets, one for each of the four needles. Within each of the main divisions, droplets were sorted into $100\mu m$ (approximately 2 pixel) wide groups by their mean major radius (Figure 3.5A). The droplets were grouped to save computing time for BEM. The occurrence of multiple groups of droplets for a single needle were the results of pressure changes during droplet formation. Droplets were approximately normally distributed about the mean radius within each group (Figure 3.5B), the majority of droplets in a group were of the mean size, while a smaller number of droplets were larger or smaller than the mean by about a pixel. The mean and standard deviation of the major radius, minor radius, and radius of a sphere of equivalent volume for the droplets in a group was calculated and used to determine the 95% confidence interval (Tables 3.2, 3.3, 3.4). The 95 % confidence interval was calculated assuming that all grouped droplets were normally distributed about the group mean. BAV, which had the highest viscosity and surface tension, resulted in the largest droplets for a given needle size, while ANS and XIK resulted in similar distributions of droplets that were smaller than BAV. The eccentricity,

$$\epsilon = \sqrt{1 - \frac{a_{min}^2}{a_{maj}^2}}, \tag{3.13}$$

where a_{min} is the minor radius and a_{maj} is the major radius, was then calculated for each binned droplet. The oil droplets were oblate spheroids with eccentricities between 0.42 and 0.63. BAV was the least eccentric oil, with no values above 0.5, and eccentricity increased with droplet size for all oils.

Table 3.2: Droplet size and shape for ANS according to machine vision camera system. Equivalent radius is for a sphere of equivalent volume. N is the number of observations in the 100μm group. All radii and confidence intervals are in mm. All confidence intervals are calculated for $\alpha = 0.05$. Rise velocity (U) is in m/s

a_{maj}	a_{min}	r_{eq}	ϵ	N	Re/Eo/log(M)	U
2.39 ± 0.07	2.08 ± 0.04	2.28 ± 0.06	0.49	6	480/0.9/-10.3	0.100±0.005
2.47 ± 0.05	2.14 ± 0.06	2.35 ± 0.05	0.50	9	470/1.0/-10.3	0.096±0.004
2.59 ± 0.04	2.24 ± 0.07	2.47 ± 0.05	0.50	6	500/1.1/-10.3	0.097±0.004
2.74 ± 0.05	2.31 ± 0.06	2.59 ± 0.04	0.54	26	570/1.2/-10.3	0.105±0.009
2.85 ± 0.06	2.37 ± 0.09	2.68 ± 0.07	0.56	15	610/1.3/-10.3	0.108±0.007
2.95 ± 0.06	2.44 ± 0.03	2.77 ± 0.04	0.56	6	620/1.4/-10.3	0.108±0.007
3.14 ± 0.06	2.55 ± 0.09	2.93 ± 0.04	0.58	8	700/1.5/-10.3	0.114±0.007
3.23 ± 0.04	2.56 ± 0.12	2.99 ± 0.06	0.61	8	710/1.6/-10.3	0.114±0.009
3.50 ± 0.01	2.87 ± 0.04	3.27 ± 0.02	0.57	5	720/1.9/-10.3	0.105±0.002

Table 3.3: Droplet size and shape for XIK according to machine vision camera system. Equivalent radius is for a sphere of equivalent volume. N is the number of observations in the 100μm group. All radii and confidence intervals are in mm. All confidence intervals are calculated for $\alpha = 0.05$. Rise velocity (U) is in m/s

a_{maj}	a_{min}	r_{eq}	ϵ	N	Re/Eo/log(M)	U
2.19 ± 0.05	1.90 ± 0.07	2.09 ± 0.06	0.50	23	380/0.9/-10.1	0.087±0.006
2.51 ± 0.05	2.08 ± 0.07	2.36 ± 0.05	0.56	15	450/1.1/-10.1	0.091±0.004
2.59 ± 0.05	2.13 ± 0.07	2.42 ± 0.05	0.57	12	470/1.2/-10.1	0.093±0.004
2.92 ± 0.05	2.39 ± 0.12	2.73 ± 0.06	0.58	29	540/1.5/-10.1	0.095±0.005
3.27 ± 0.05	2.58 ± 0.13	3.02 ± 0.06	0.61	19	660/1.9/-10.1	0.105±0.006
3.34 ± 0.06	2.59 ± 0.11	3.07 ± 0.07	0.63	12	690/1.9/-10.1	0.108±0.006
3.46 ± 0.06	2.77 ± 0.23	3.21 ± 0.11	0.60	4	750/2.1/-10.1	0.112±0.007
3.51 ± 0.05	2.81 ± 0.03	3.26 ± 0.04	0.60	2	750/2.2/-10.1	0.110±0.006

Table 3.4: Droplet size and shape for BAV according to machine vision camera system. Equivalent radius is for a sphere of equivalent volume. N is the number of observations in the 100μm group. All radii and confidence intervals are in mm. All confidence intervals are calculated for $\alpha = 0.05$. Rise velocity (U) is in m/s

a_{maj}	a_{min}	r_{eq}	ϵ	N	Re/Eo/log(M)	U
3.33 ± 0.04	3.01 ± 0.11	3.22 ± 0.06	0.42	20	520/0.9/-10.6	0.077±0.006
3.39 ± 0.07	3.07 ± 0.07	3.28 ± 0.05	0.43	10	530/0.9/-10.6	0.077±0.003
4.06 ± 0.05	3.68 ± 0.07	3.93 ± 0.04	0.43	3	710/1.3/-10.6	0.086±0.002
4.15 ± 0.05	3.73 ± 0.15	4.01 ± 0.07	0.44	7	740/1.3/-10.6	0.089±0.008
4.25 ± 0.06	3.84 ± 0.08	4.11 ± 0.06	0.43	9	800/1.4/-10.6	0.094±0.004
4.35 ± 0.03	3.88 ± 0.20	4.18 ± 0.07	0.45	4	820/1.4/-10.6	0.094±0.012
4.62 ± 0.04	4.23 ± 0.11	4.48 ± 0.06	0.40	8	850/1.7/-10.6	0.091±0.004
4.70 ± 0.06	4.26 ± 0.11	4.55 ± 0.07	0.43	6	870/1.7/-10.6	0.091±0.013
4.81 ± 0.09	4.34 ± 0.06	4.65 ± 0.05	0.43	6	890/1.8/-10.6	0.091±0.006
4.91 ± 0.06	4.38 ± 0.15	4.72 ± 0.09	0.45	4	910/1.8/-10.6	0.093±0.011
5.00 ± 0.02	4.39 ± 0.05	4.79 ± 0.03	0.48	4	930/1.9/-10.6	0.093±0.010

The droplet measurements were compared to the droplet shape and size predicted by Clift *et al.* (1978), who used three non-dimensional numbers to describe the shape of particles: the Reynolds (Re), Eötvös (Eo) or Bond, and Morton (M) numbers. Each number is a function of the physical properties of the particle and the surrounding medium:

$$Re = \frac{\rho_w d_e U}{\mu_w} \qquad Eo = \frac{G \Delta \rho_w d_e^2}{\sigma} \qquad M = \frac{g \mu_w^4 \Delta \rho}{\rho_w^2 \sigma^3}, \tag{3.14}$$

where d_e is the diameter of the particle (major diameter for rising oblate spheres), U is the rise rate, μ_w is the viscosity of the surrounding medium, g is gravitation acceleration, $\Delta\rho$ is the difference in density between the particle and surrounding medium and σ is the interfacial tension of particle in the surrounding medium. The rise rate was calculated from the transducer observations by dividing the distance risen by a droplet between pings by the time between pings. The three non-dimensional numbers converge as predicted by Clift *et al.* (1978) in the region between spheres and wobbling ellipsoidal particles. This agrees well with the oblate spheroid shape measured by the camera.

3.5.2 Frequency Response

The two features of the broadband frequency response used to quantify targets are the amplitude of peaks, and frequency of nulls. These two features were identified in the measured backscatter as well as in the three models. The amplitude of the peak and frequency of nulls in the measurements were then compared to the modeled peaks and nulls to determine whether or not those features differed significantly between the model and measured backscatter. Differences between the measured and modeled results indicate that inversions of the models would result in errors in predicting the droplet size based on the broadband backscatter.

The intensity at each frequency for all pings of an individual droplet was averaged together. Figure 3.6 shows the TS calculated for each of 20 pings incident on a 2.93 mm equivalent radius ANS droplet as well as the average intensity of those 20 pings in dB. 83% of the backscatter measurements at a given frequency were within 30% of the mean intensity (corresponding to the mean TS $+1.1dB/-1.5$ dB). As TS decreased (near nulls), the width of the distribution of TS measurements about the mean increased. When the mean TS value at a given frequency was below -85dB, 74% of measurements were within 30% of the mean intensity.

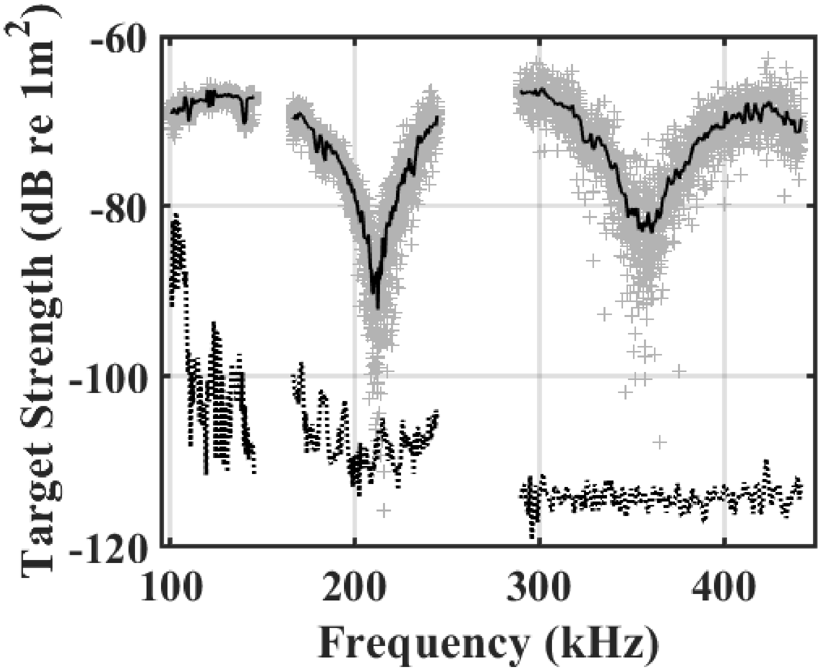

Figure 3.6: Frequency response for a single ANS droplet of equivalent radius 2.93 mm. Gray crosses are from individual pings, and the black line is the mean intensity calculated at each frequency in dB. The dotted lines indicate the noise floor of the three transducers.

The imaging system and broadband acoustic system were time synced so that the droplet size and shape from the imaging system for a single droplet was directly correlated with the TS measurement from the broadband acoustic system. The TS measurements were sorted with the droplet size and shape data into groups by the major radius as described above. The intensity was then averaged for all droplets in a group. Examples of acoustic results from a grouped droplet of each oil are shown in Figure 3.7.

The DWBA and BEM model were then calculated for an oblate sphere with dimensions

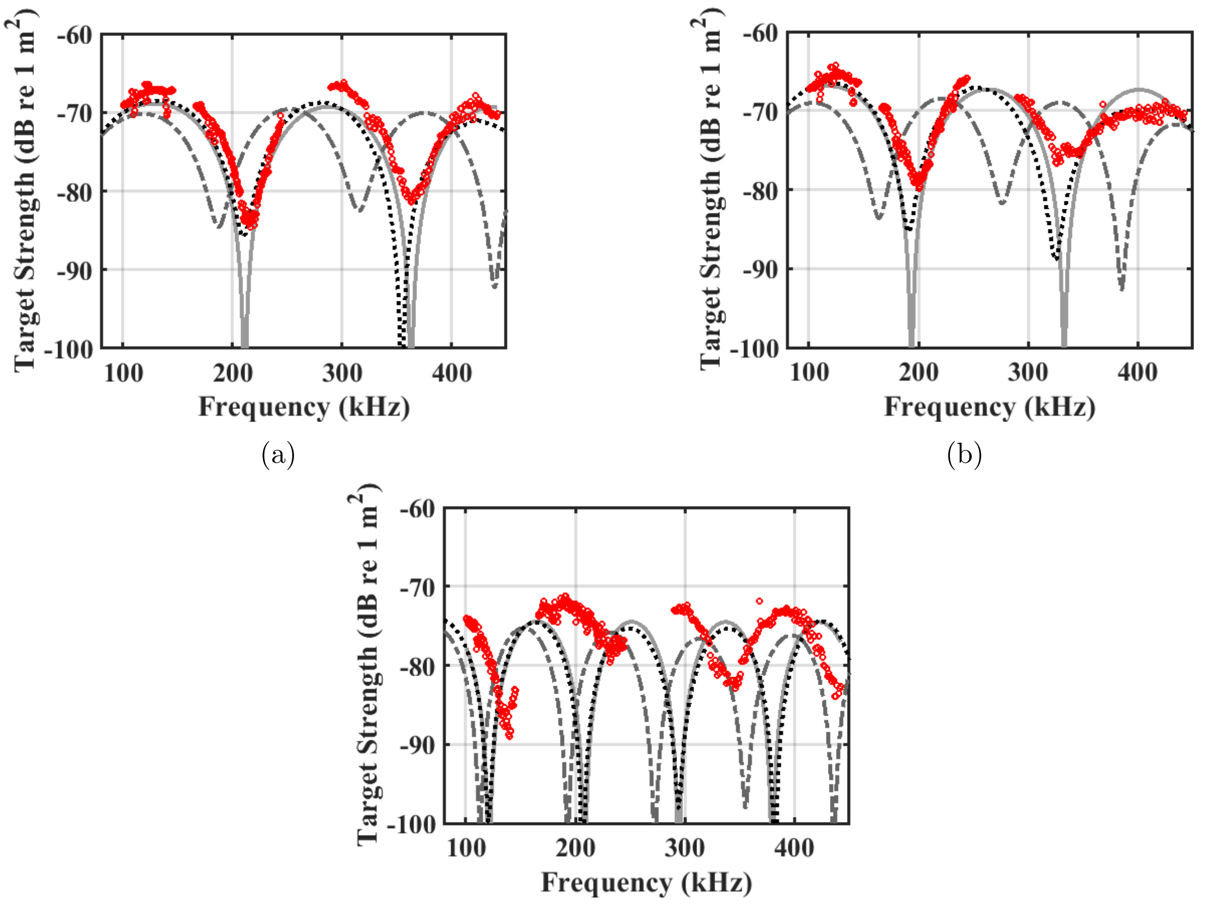

(a)

(b)

(c)

Figure 3.7: Recorded scattering (red circles) compared to Anderson 1950 (dashed gray line), DWBA (solid gray line) and BEM (dotted black line). (a) **ANS:** Equivalent radius: 2.68mm (b) **XIK:** Equivalent radius: 3.07mm (c) **BAV:** Equivalent radius: 4.65mm

equal to the grouped major and minor radius, while the Anderson (1950) model was calculated for the grouped radius of a sphere of equivalent volume (Figure 3.7). The peak of the modeled TS of each droplet was compared to the peak of the measured TS (Figure 3.8). All models were computed for 80 kHz to 450 kHz with 500 Hz spacing for the Anderson (1950) model and DWBA and 2 kHz spacing for the BEM. The BEM was computed at larger frequency spacing due to constraints on available computational time. The peak of the measured response was determined by the MATLAB mspeaks function which uses wavelet de-noising to smooth the signal and then finds the center of mass of peaks using a user defined peak proportion (20% for this study) to determine the centroid of the peak

(Coombes *et al.* , 2005; Morris *et al.* , 2005). Measured peaks within 10 kHz of the gap in frequencies between transducers were excluded because it was not possible to determine whether the peak was in the gap or not.

To determine the accuracy of each model when inverted for droplet size Figures 3.9, 3.10 and 3.11 compare the frequency of nulls from the modeled TS to the frequencies of nulls determined experimentally. An offset between the modeled and measured TS indicates that the inversion would results in an error in droplet size estimate. Null frequency was determined by inverting the TS plot and using the MATLAB mspeaks function as described above. Experimental data with nulls within 10 kHz of the gap in frequencies between transducers were excluded because it was not possible to reliably determined if the null was in the gap or not.

To determine the variability of the predicted null frequency due to measurement error the three models were run for grouped droplet sizes measured by the imaging system at the 95% confidence limits (Tables 3.2, 3.3, 3.4). For the Anderson (1950) model, these limits represent two simple cases; droplet size was either underestimated or overestimated. These cases represent the frequency range over which the null would be expected to occur for a droplet with an equivalent radius within the 95% confidence limit of the measured droplet size (Figures 3.9,3.10 and 3.11). For oblate shapes the confidence limits were evaluated for four different cases: case 1 - droplet size is underestimated by both the minor and major radius, case 2 - droplet size is overestimated by both the minor and major radius, case 3 - the droplet is more oblate than measured by underestimating the major radius and overestimated the minor radius, and case 4 - the droplet is more spherical than measured due to overestimating the major radius and underestimating the minor radius. These cases were evaluated at the 95% confidence limits for the mean major and minor radius as appropriate. According to the model results, cases 3 and 4 represent the more extreme limits of the confidence interval and are shown in Figures 3.9, 3.10 and 3.11.

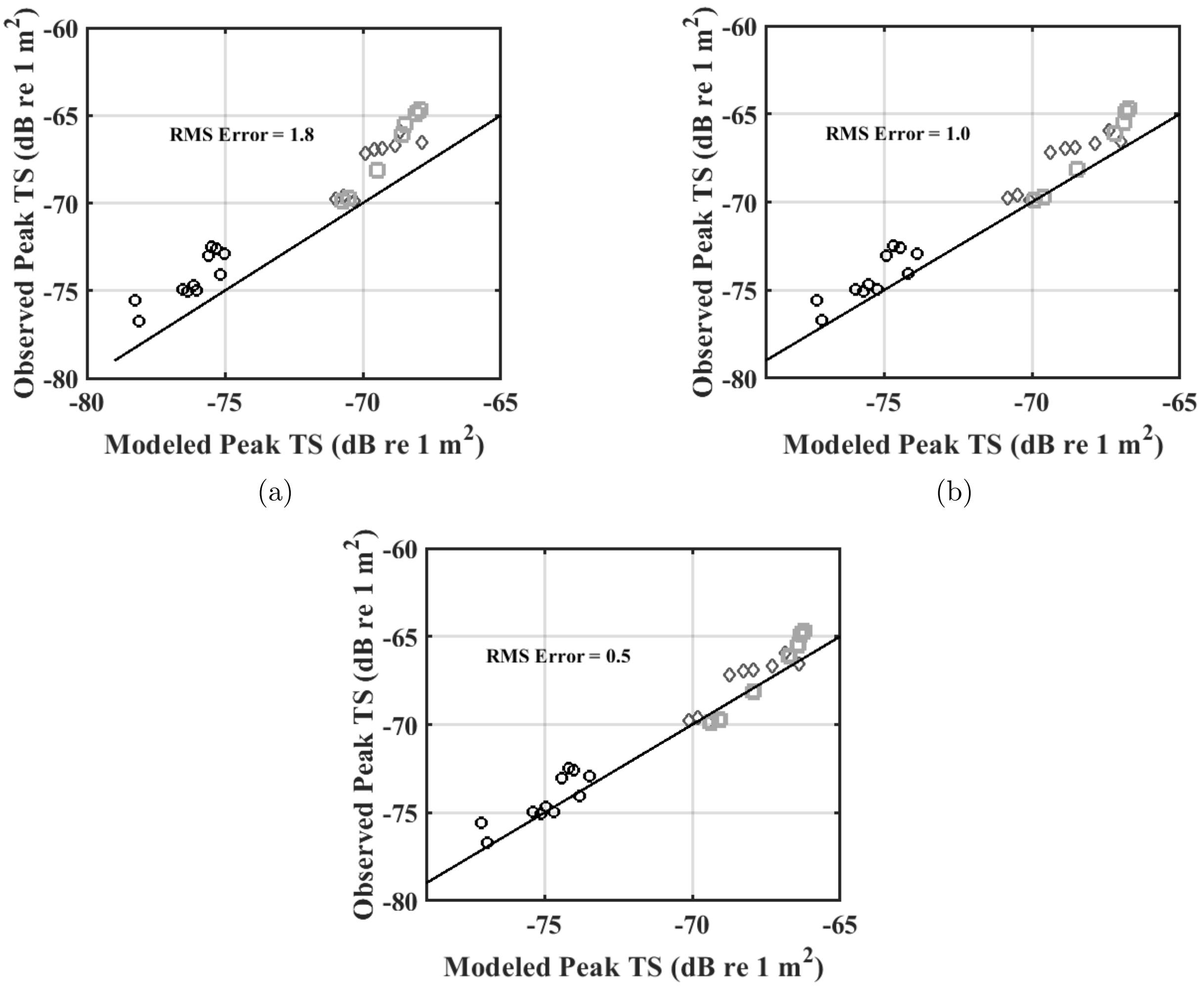

(a) (b) (c)

Figure 3.8: Peak amplitude of the measured TS compared to the peak of (a) Anderson (1950), (b) the DWBA, and (c) the BEM. ANS (dark gray diamonds), XIK (light gray squares), and BAV (black circles) are compared to unity (black line). The RMS error between all measurements and the modeled peak is listed for each model.

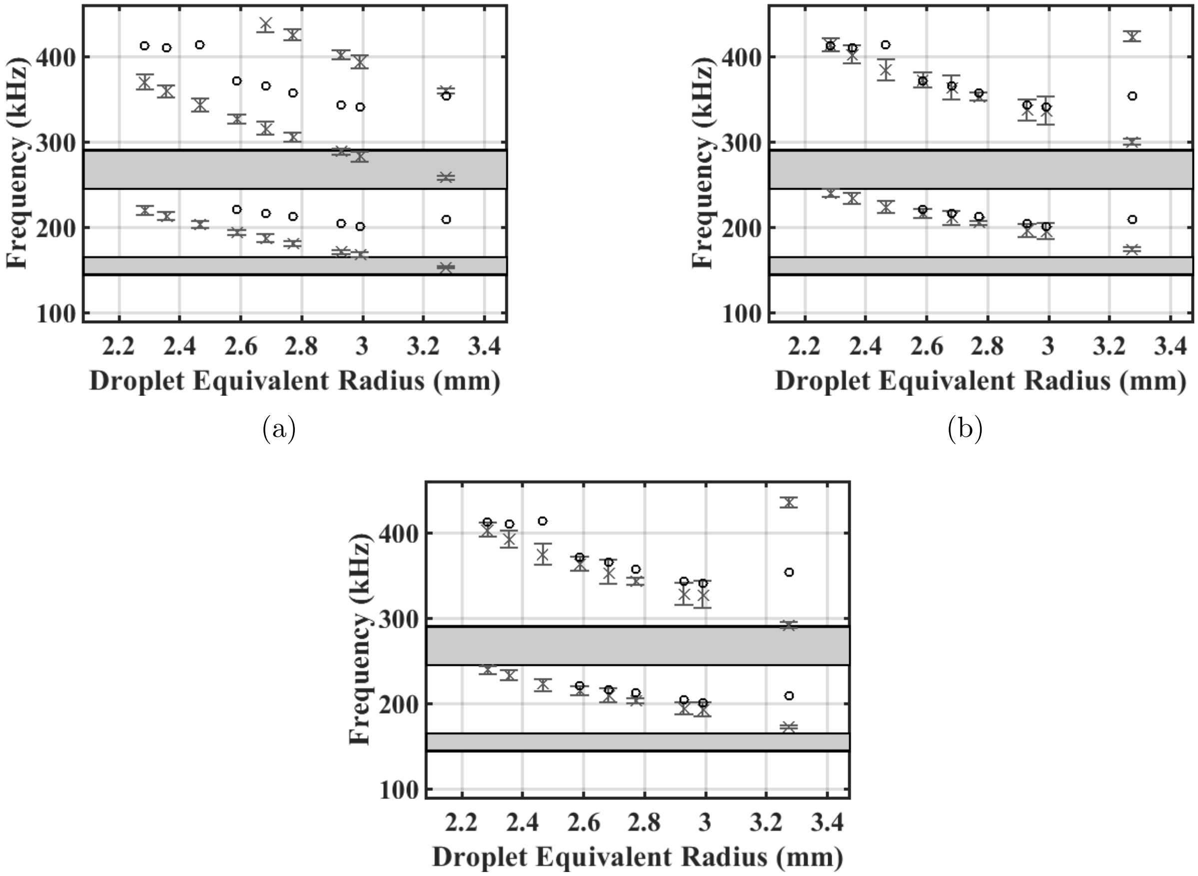

(a)

(b)

(c)

Figure 3.9: Frequency of the null in ANS for measured (black circle) and modeled (gray x) TS according to (a) Anderson (1950), (b) DWBA, (c) BEM. The null frequency for models computed at the 95% confidence limits of droplet size are indicated by bars above and below model markers. Gray boxes show the gap in ensonified frequencies between transducers. For recorded data, nulls detected within 10 kHz of the gap in frequencies between transducers are excluded.

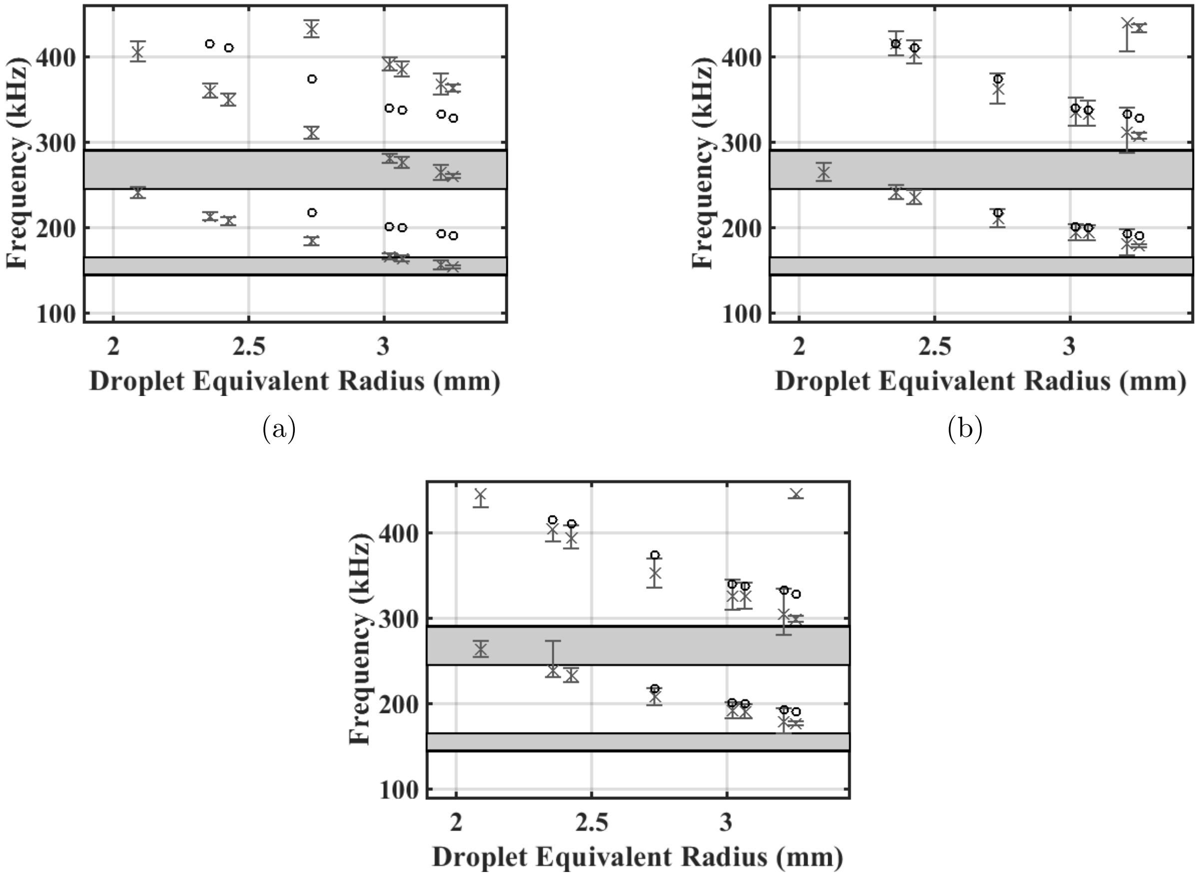

(a)

(b)

(c)

Figure 3.10: Frequency of the null in XIK for measured (black circle) and modeled (gray x) TS according to (a) Anderson (1950), (b) DWBA, (c) BEM. The null frequency for models computed at the 95% confidence limits of droplet size are indicated by bars above and below model markers. Gray boxes show the gap in ensonified frequencies between transducers. For recorded data, nulls detected within 10 kHz of the gap in frequencies between transducers are excluded. Note that no nulls were detected for the measured TS of the smallest XIK droplet.

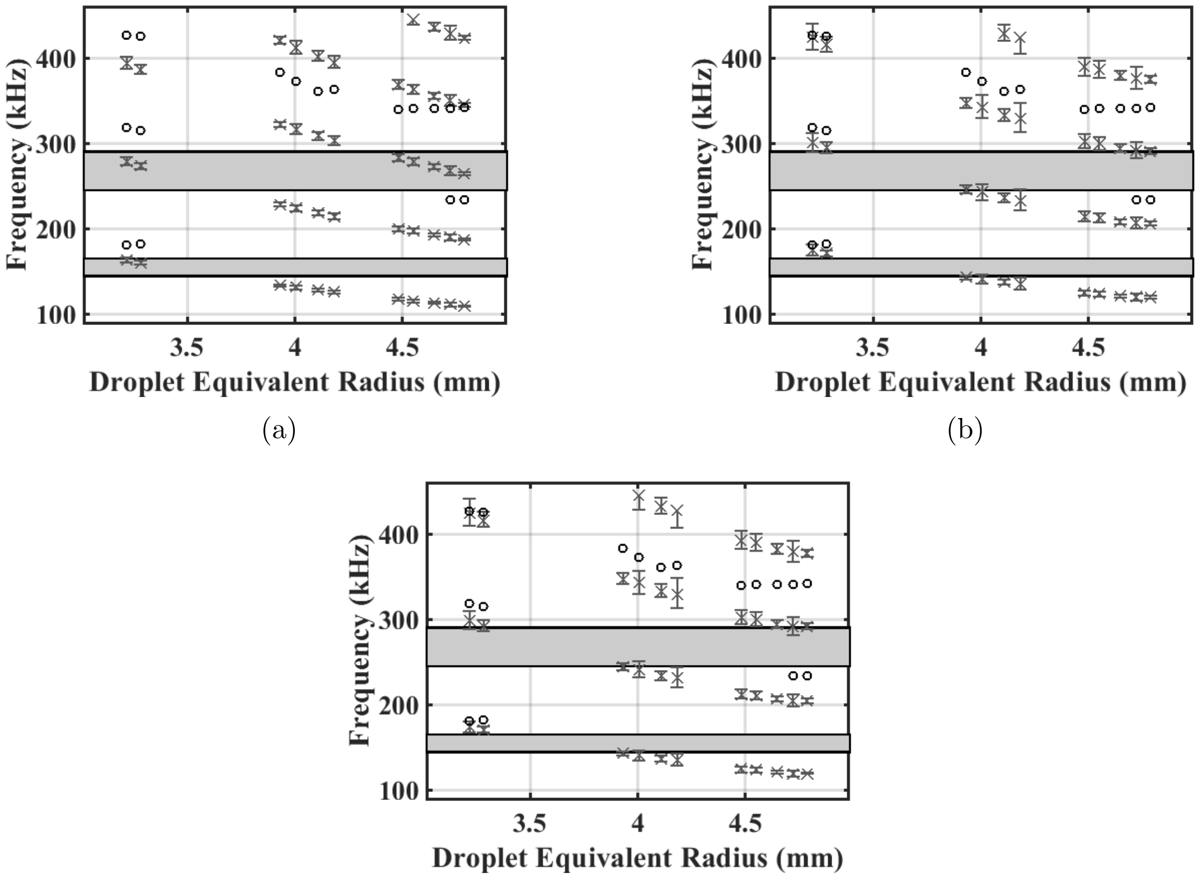

(a)

(b)

(c)

Figure 3.11: Frequency of the null in BAV for measured (black circle) and modeled (gray x) TS according to (a) Anderson (1950), (b) DWBA, (c) BEM. The null frequency for models computed at the 95% confidence limits of droplet size are indicated by bars above and below model markers. Gray boxes show the gap in ensonified frequencies between transducers. For recorded data, nulls detected within 10 kHz of the gap in frequencies between transducers are excluded.

3.6 Discussion

The BEM is a slightly better predictor of the amplitude of the peak of the TS response than the DWBA, and both the BEM and DWBA are slightly better predictors of peak TS than Anderson (1950). The RMS error between the modeled and predicted peak backscattering cross section for all peaks (excluding peaks within 10 kHz of the gap in frequencies between transducers) was 1.8 dB, 1.0 dB, and 0.5 dB for Anderson (1950), the DWBA, and the BEM respectively. The Anderson (1950) model does not accurately predict the null frequency for the oblate oil spheres in this study. RMS error between the measured and modeled frequency of nulls for all measured nulls (excluding nulls within 10 kHz of the gap in frequencies) predicted by Anderson (1950) was 51 kHz, 53 kHz and 52 kHz, for ANS, XIK and BAV respectively. The DWBA and BEM provide better agreement between frequency of the predicted and observed null for ANS and XIK droplets, with RMS error between the measured null frequency and null frequency predicted by the BEM of 23 kHz and 17 kHz for ANS and XIK respectively. For the DWBA, RMS error between the measured null frequency and predicted null frequency was 19 kHz and 11 kHz, for ANS and XIK respectively. If the largest ANS droplet is excluded, RMS error for ANS drops to 15 kHz and 10 kHz for the BEM and DWBA respectively. The lower RMS error for the DWBA indicated that it is a slightly better predictor of null frequency. The frequency of the nulls for BAV, on the other hand, do not agree with the DWBA or BEM over most of the size range. The RMS error between the measured null frequency and the null predicted were 31 kHz and 32 kHz for the DWBA and BEM respectively (assuming that the predicted null was always lower in frequency than the measured). The discrepancy between the measured and modeled null frequency increases with increasing droplet size.

To determine the impact of the discrepancy between the frequency of the modeled and measured null, the difference between the measured droplet size and the size of a droplet predicted by each model was determined. For a given measured droplet size, the frequency of nulls associated with that droplet were used to invert the three scattering models and determine droplet size. For the Anderson (1950) model, nulls at 216 kHz and 365 kHz occur for an ANS droplet with equivalent radius 2.36 mm, which is 33 % smaller than the volume of the observed droplet. Following this example, the % difference in the predicted volume was calculated for all droplet groups and all three models (Figure 3.12). All models under-predict the measured droplet volume. The volume error for a given oil increases with increasing droplet size and eccentricity. For XIK and ANS, when compared to the DWBA and BEM, the difference between the predicted and measured droplet size was often within the 95% confidence limits (Figures 3.9,3.10 and 3.11), therefore the predictions agreed with the direct measurements within the accuracy of the imaging system.

In modeling the frequency response, it was assumed that the impact of dispersion in sound speed was negligible. The sound speed of all oils was measured at 750 kHz (Loranger *et al.* , 2018), and there is potential for changes to that sound speed at the frequencies in this study due to dispersion. However, the relationship between sound speed (and attenuation) and frequency for all of the oils is not known, and therefore could not be included in the model. BAV produced the largest droplets and had the highest viscosity oil by an order of magnitude and therefore attenuation is likely to be most pronounced in BAV droplets. The offset in the null frequency in BAV between the measurements and both the DWBA and BEM could be the result of such dispersion. The frequency dependence of the sound speed for these oils is an area requiring further research.

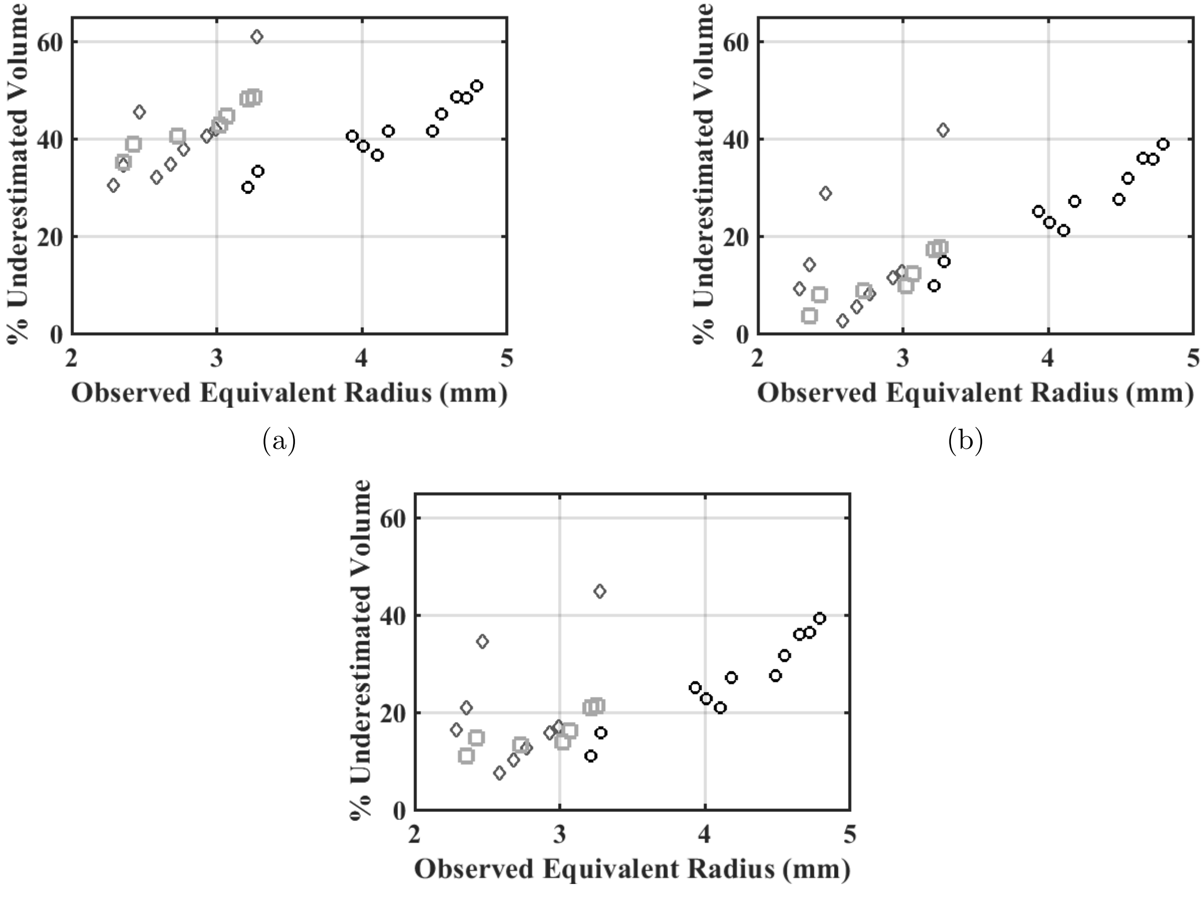

(a)

(b)

(c)

Figure 3.12: % Error in the estimated droplet volume of a droplet when using the null frequency to determine droplet size with (a) Anderson (1950), (b) the DWBA and (c) the BEM for ANS (dark gray diamonds), XIK (light gray squares), and BAV (black circles).

3.7 Conclusions

The BEM, DWBA and Anderson (1950) are good predictors of the peak of the TS; the RMS difference in backscattering cross section between the observation and models is equivalent to 1.8 dB, 1.0 dB and 0.5 dB for Anderson (1950), the DWBA and the BEM respectively. The DWBA and BEM predict the null frequency for an oblate sphere of ANS and XIK crude oil within the accuracy of the droplet measuring system. BAV, the DWBA and BEM predict a droplet within 20% of the observed volume for the smallest droplets, however, as droplet size increases the DWBA and BEM increasingly under-predict the volume with a maximum under-prediction of almost 40% for the largest droplet. The Anderson model tends to under-predict droplet volume by between 30 - 50%, with increasing error as droplet size and eccentricity increase for an individual oil.

If using the broadband frequency response to invert scattering models and predict droplet shape, the DWBA and BEM are good predictors of droplet volume for ANS and XIK, which are lower viscosity oils and droplet sizes were smaller than BAV. For the higher viscosity oil, BAV, which produced larger droplets, significant errors were observed between the predicted and measured size with increasing discrepancy between predicted and measured sizes as droplet size increases. A potential source of this discrepancy is dispersion, which was not accounted for here and further research on these processes is necessary to determine if they significantly impact broadband backscatter from oil droplets.

Acknowledgement

We thank the Center for Complex Fluids at Carnegie Mellon Universtiy for providing the surface tension analysis; Paul Lavoie from the University of New Hampshire for assistance in the design and construction of the droplet making system; Peter Vrolijk and John Blum from Exxon Mobile and Andone Lavery of Woods Hole Oceanographic Institution for providing crude oil samples. The work was supported by the National Oceanic and Atmospheric Administration (Grant # NA15NOS4000200).

Chapter 4

Hydrocarbon detection and quantification at a marine oil and gas seep

Scott Loranger[1], **and Thomas C. Weber**[3]

[1] Department of Earth Sciences, University of New Hampshire, Durham, NH 03824

[4]Department of Mechanical Engineering, University of New Hampshire, 105 Main Street, Durham, NH 03824

Abstract

In order to determine the fate and transport of oil from anthropogenic spills and to understand the role that natural oil seepage plays in the marine environment it is crucial be able to determine the flow rate of oil from anthropogenic and natural sources on the seafloor. Current instrumentation used for oil detection and quantification in the water column is limited to short ranges on the order of centimeters to meters. Broadband acoustics have the potential to detect and quantify oil from greater distances and sample larger volumes more rapidly, and more synoptically than the point measurements made by current instrumentation. In September 2017 an acoustic Doppler current profiler (ADCP) and a high frequency (90 kHz to 154 kHz) broadband echo sounder were deployed to asses the flow rate of oil and gas from a seep site in the northern Gulf of Mexico. Gas is much more efficient scatterer of sound and when gas and oil are collocated gas will mask the return from oil droplets, unless the density of oil in acoustic sample is very high compared to the gas. The plume was divided into two regimes by the rise rate of targets, a gas only regime where the rise rate was above the predicted maximum rise rate of oil droplets, and the oil droplet rise rate regime where oil droplets and gas bubbles could both occur. The plume was evaluated for two scenarios, one where the acoustic scattering in the oil droplet rise rate regime was due solely to oil droplets and the case where scattering was due solely to methane bubbles. For the assumption that the section of the plume within the predicted rise rate range of droplets was filled with only oil droplets, flow rate was between 156 - 341 barrels per day at the 95% confidence interval with a mean of 249 barrels per day. If that same region was comprised solely of methane gas bubbles, flow rate was 3.84 - 13.7 m^3 /day with a mean of 8.78 m^3 / day. The total flow rate for different gas to oil ratios was also determined.

4.1 Introduction

The fate and transport of oil droplets from natural and anthropogenic sources is key to understanding the impact of anthropogenic spills and the resilience of marine communities. Without knowledge of both natural background levels of hydrocarbons and the flow rate into the water column from anthropogenic sources, it is difficult to quantify the impact of oil spills on the marine environment. Improved *in-situ* measurements of flow rate from seafloor sources of hydrocarbons, both naturally and anthropogenically released, will help to advance our understanding of the response of the ocean to oil spills. In this study, shipboard broadband acoustic echo sounders were used to estimate the flow rate of hydrocarbons from a seafloor seep site in the Northern Gulf of Mexico.

Satellite and surface observations of surface oil slicks have been used to estimate the flow rate of oil from seafloor seeps (Hu *et al.* , 2018; MacDonald *et al.* , 2015; Fingas & Brown, 2018), however, measurements of the surface slick only examine the oil and/or gas that has reached the surface, and cannot directly determine the flow rate in the water column. Acoustic methods have been used in the water column to determine the flow rate of liquid hydrocarbons from anthropogenic seeps (Camilli *et al.* , 2012; Weber *et al.* , 2012) and to determine the flow rate of methane from natural seeps (e.g. Weber *et al.* (2014); Wiggins *et al.* (2015); Hornafius *et al.* (1999)). One of most significant impediments to determining the flow rate of oil from seafloor sources is the fact that gas bubbles and oil droplets are often collocated. Hydrocarbons enter the marine environment either as oil droplets, gas bubbles, or combined in oil coated gas bubbles. Gas is a much more efficient scatterer of sound and the backscatter from gas often masks the response from oil. Broadband acoustic backscatter has been used to differentiate between and identify different targets in the water column (Lavery *et al.* , 2010; Medwin & Breitz, 1989; Terrill & Melville, 2000; Vagle & Farmer, 1992; Holliday, 1972; Thompson & Love, 1996; Stanton *et al.* , 2010), and it shows promise for quantification and differentiation between oil droplets and gas bubbles. Broadband acoustic classification of targets takes advantage of the difference in the shape of the frequency dependent backscatter for different targets (Figure 4.1). The resonance peak and high amplitude scatter at low frequencies are characteristics used to quantify the size and number of bubbles. For weak scatterers such as oil droplets, the transition from Rayleigh scattering, where the wavelength of the sound wave is larger than the radius of the target, to geometric scattering, where the wavelength is smaller than a target, can be used for quantification as can the peak and null structure in the geometric scattering regime (Loranger *et al.* , In review). Broadband acoustic echo sounders also provide for improved range resolution (Weidner *et al.* , 2019) over narrow band systems, an important consideration for mixed targets such as oil droplets and gas bubbles.

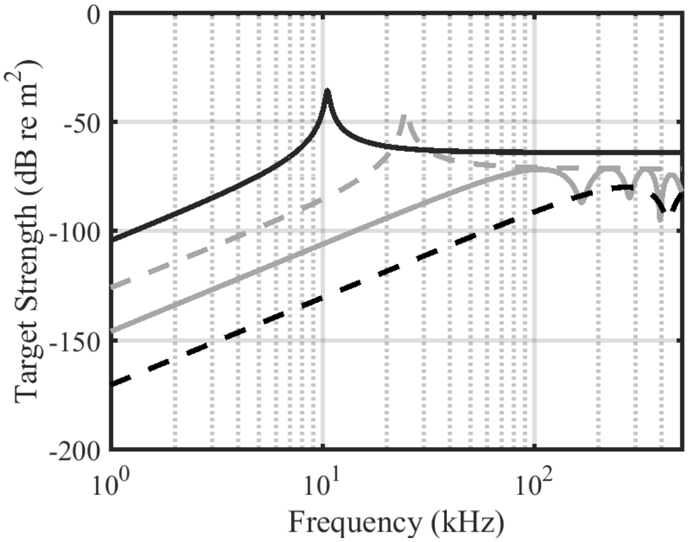

Figure 4.1: The predicted target strength (TS) of gas bubbles and oil droplets. The target strength for a methane bubble of radius 0.65 mm (solid black line) and a bubble with radius 0.28 mm (grey dashed line) show the distinct resonance peak and high amplitude scattering at low frequencies typical of gas bubbles. A 3.0 mm radius droplet (grey solid line) and 1.2 mm radius droplet (black dashed line) show a much lower target strength at low frequencies and the distinct peak and null structure of weak fluid scatterers at higher frequencies.

To evaluate the application of broadband acoustic methodologies to quantification and classification of oil and gas in the ocean, an opportunistic survey was performed at a site of a persistent oil and gas seep in the Northern Gulf of Mexico. The plume is adjacent to an oil production platform that was toppled by Hurricane Ivan in 2004. The platform sits at a depth of about 140 meters and a persistent plume producing a surface oil slick is emanating from the area immediately surrounding the downed platform. The site is near the mouth of the Mississippi River in a biologically productive and sediment laden environment.

The survey was conducted in September 2017 with an acoustic Doppler current profiler (ADCP) and a broadband echo sounder to asses the flow rate of oil and gas from the site described above. This work explores what the surface-based acoustic survey can determine about the magnitude of the flow rate of hydrocarbons. The horizontal currents measured by the ADCP were combined with measurements by the echo sounder of the depth of the plume as a function of distance downstream to determine the rise rate. A model of the rise rate of bubbles and droplets (Zheng & Yapa, 2000) was used to determine the size of oil droplets and methane bubbles as a function of the rise rate. The acoustic backscatter from the plume was combined with the target size estimate to determine the number of targets of a given size. The number and size of targets was integrated to provide bounds for the volumetric flow rate of oil and of gas at eleven cross sectional views of the plume.

4.2 Surveys

4.2.1 ADCP

Horizontal current profiles were measured by a 300 kHz Teledyne-RDI Sentinel V Workhorse acoustic Doppler current profiler (ADCP). The ADCP was pole mounted on the port side of the M/V Gerry Bordelon and deployed at a depth of about 1.5 meters. Raw broadband data was recorded in 6-meter depth bins. Vessel location was determined by a WAAS-enabled GPS. Each ADCP survey consisted of four approximately 800 meter long lines run perpendicular to the nominal current direction ($\sim 60°$) during the time of the experiment (Figure 4.2). A preliminary ADCP survey determined the nominal current direction and informed survey locations. Four total lines were run for each survey; two lines downstream to the south west of the downed platform and two lines upstream to the northeast of the platform. At each location, one line was run heading northwest and then another line was repeated over the same area heading southeast. The sets of lines at each location were run at a speed over ground of about 4 knots. ADCP Surveys were run prior to and then again following the WBT survey. The times of surveys (GMT) are listed in Table 2.1.

Table 4.1: Survey times (GMT) for surveys run on September 23 2017.

First ADCP	Echo sounder Perpendicular	Echo sounder Parallel	Second ADCP
0120 - 0136	0227 - 0652	0704 - 0838	0848 - 0921

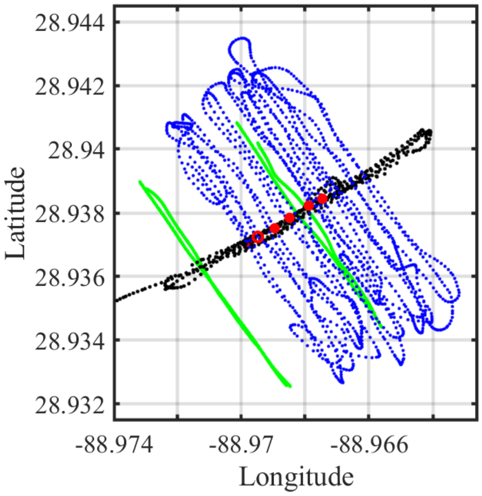

Figure 4.2: ADCP and WBT Survey locations; WBT cross sectional survey lines run perpendicular to the nominal flow direction (blue), WBT down-stream survey lines run parallel to flow (black) and ADCP survey lines run perpendicular to flow (green). Most WBT lines were run downstream of the plume origin (red o). The red dots show the location of the echograms in Fig 4.3, where echogram A is the cross sectional pass closest to the origin, echogram B then next farthest and D is the cross sectional pass farthest from the origin of the echograms shown. Echogram A is the first pass where the entire plume was within the range of the ADCP data and it shows a cross section of the plume as well as the platform lying on the seafloor. Echograms B-D show the two separate seeps at shallow depths.

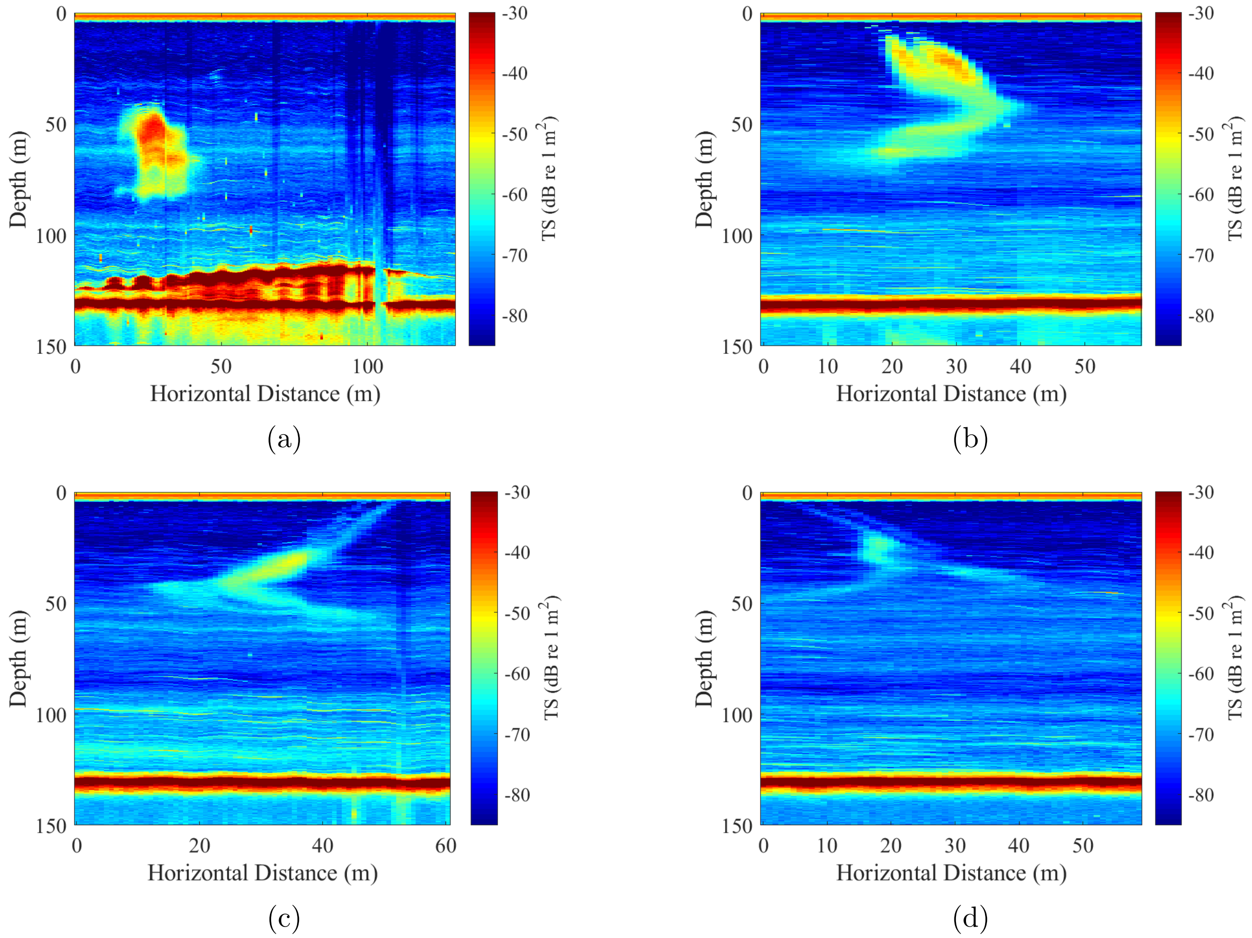

(a) (b) (c) (d)

Figure 4.3: Echograms for cross sectional passes downstream of the northern seep origin (see Plume Origin section) at the locations shown in Fig 4.2. (a) is the echogram closest to the origin (58 m), followed by (b) (115 m) then (c) (187 m) and (d) is the cross sectional pass furthest from the northern seep origin (235 m) of the four echograms shown here.

4.2.2 Broadband Echosounder

A Kongsberg ES120 echosounder was deployed on the same pole mount as the ADCP on the port side of the R/V Gerry Bordelon. The ES120 (center frequency 120 kHz) was connected to a Kongsberg Wide Band Transciever (WBT) to enable broadband transmission and reception. A four millisecond linear frequency modulated (LFM) pulse was transmitted with bandwidth 90-154 kHz. The WBTs apply a Tukey window to the transmit signal, resulting in tapered regions within the transmitted frequencies. The ratio of the tapered bandwidth to total transmitted bandwidth was 0.09. Data analysis was restricted to frequencies not in the tapered region: 94-153.5 kHz. The ES120 was calibrated in a 12 m x 18 m x 6 m (length x width x depth) fresh water tank at the University of New Hampshire according to the method described by Demer *et al.* (2015).

One kilometer long cross sectional survey lines were run perpendicular to the nominal current direction with 50 meter line spacing (Figure 4.2). Cross sectional lines were run northwest to southeast and then repeated coming back from southeast to northwest. The next pair of lines was then run 50 meters to the northeast of the previous line and the survey was then repeated starting with lines farthest to the northeast and coming back southeast. The cross sectional lines were used to estimate the position of the hydrocarbon plume after each survey line by visually assessing the recorded echogram (Fig 4.3) and manually estimating the center of the acoustically observed plume (red dots in Fig 4.2). These lines were also used to determine the rise rate of the plume and the total volumetric flow rate. The plume locations determined by the cross sectional lines were used to estimate the position of the hydrocarbon plume as it moved downstream from the origin. Downstream lines run over the estimated plume position were then run to achieve three main objectives: 1. to visualize the entire plume, 2. to determine an estimate of the origins of seeps and 3. to confirm that the plume recorded in the cross sectional passes was the same plume emanating from near the downed platform (Figure 4.4).

The downstream echograms show a plume where the fastest rise rate targets at the top of the plume have a strong target strength compared to the lower rise rate targets. This causes the appearance of a high backscattering "spine" of targets at the top of the plume, and a lower backscattering section below the plume. The current varied by around 15° as a function of depth (See Horizontal Current section below), and this variation in current resulted in the plume coming in and out of the beam on individual downstream passes different passes; for example in Fig 4.4A the plume moves out of the beam at around 200 m horizontal distance. However, at distances where the plume moved out of the beam, it was detected by at least one other downstream pass due to slight variations in the location of lines run during downstream passes. There is also the indication of a counter current at depths below 100 m. At these depths, the plume bends to the left in the echograms (in the ”upstream” direction) before the plume continues to move ”downstream” for shallower depths.

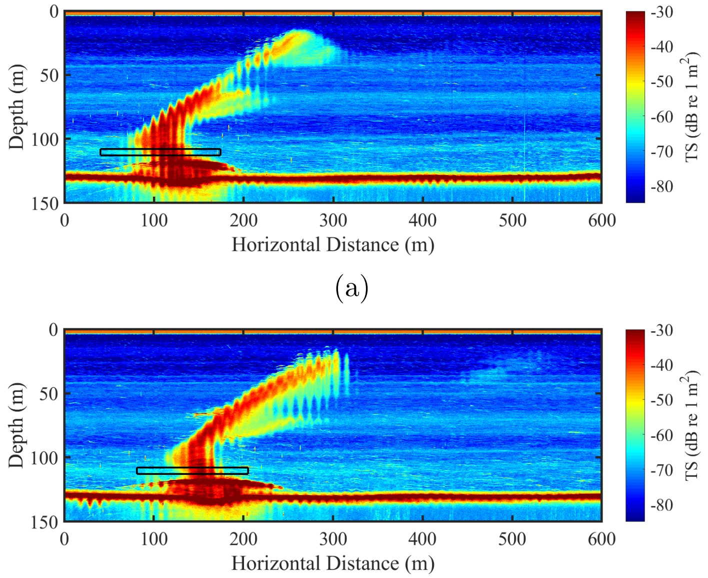

(a)

(b)

Figure 4.4: Down-stream WBT survey echograms for lines run parallel to flow. These are examples of two of eight lines run parallel to the nominal direction of flow connecting the locations of the plume determined by the cross section survey. The downed platform is visible on the seafloor. The black box shows the area of the echogram used to determine the origin of seeps. In echogram a, the plume was out of the beam for horizontal distances between 190 and 220 meters, due to variation in the current direction and position of the vessel during down-stream passes.

4.3 Horizontal Current

The ADCP was oriented so that beam 3 (the “forward” beam in beam coordinates, Fig. 4.5) was oriented 45° to port of the forward direction of the vessel. Each beam of the ADCP is oriented 20° from nadir. Raw beam coordinate data was first transformed to ships coordinates to obtain the forward (V_{fwd}), starboard (V_{stbd}) and vertical velocities (V_v) according to:

$$V_{stbd} = \frac{1}{2}\left[\frac{b_3 - b_4}{sin(20)}\right] sin(45) + \frac{1}{2}\left[\frac{b_1 - b_2}{sin(20)}\right] cos(45), \tag{4.1}$$

$$V_{fwd} = \frac{1}{2}\left[\frac{b_4 - b_3}{sin(20)}\right] cos(45) + \frac{1}{2}\left[\frac{b_1 - b_2}{sin(20)}\right] sin(45), \tag{4.2}$$

$$V_v = \frac{b_1 + b_2 + b_3 + b_4}{4\, sin(20)}, \tag{4.3}$$

where b_1, b_2, b_3 and b_4 are beams 1, 2, 3 and 4 respectively. The velocity measurement at the seafloor was then subtracted from the recorded velocities to account for the movement of the vessel. Finally, the ships coordinate data was transformed to earth coordinates using the heading recorded by the ADCP, plus an offset of 45°. The ADCP records the heading as if the instrument were oriented with b_3 facing forward, and the 45° adjustment accounts for the actual orientation of the ADCP. The error velocity and percent good were also calculated. The error velocity is a measure of the heterogeneity of the vertical velocity measurements. ADCP measurements assume that the flow is homogeneous within a sample and a high error velocity indicates that the flow at a given depth is heterogeneous resulting in errors in estimates of the horizontal velocity for high error velocity values. The percent good is a measure of the percent of pings that pass a correlation threshold, set to the manufacturers suggested value of 120 (correlation is a unitless value determined by the correlation performed by the instrument). Any pings with an error velocity above 0.3 m/s were rejected. Pings were then ensembled into 20 ping ensembles at each depth. Any depth measurements with ensembles that had fewer than 30% of measurements pass the correlation threshold and error velocity threshold were rejected.

Two ADCP surveys were performed, one before and one after the WBT survey (Table 1). Current profiles were observed up to a depth of 95.2 m in the pre-WEBT ADCP survey and 77.2 m for the post-WBT ADCP survey. The post-WBT ADCP survey was performed in higher seas than the pre-WBT ADCP survey, which likely increased the background noise in the measurement, decreasing the correlation in lower ADCP bins for and resulted

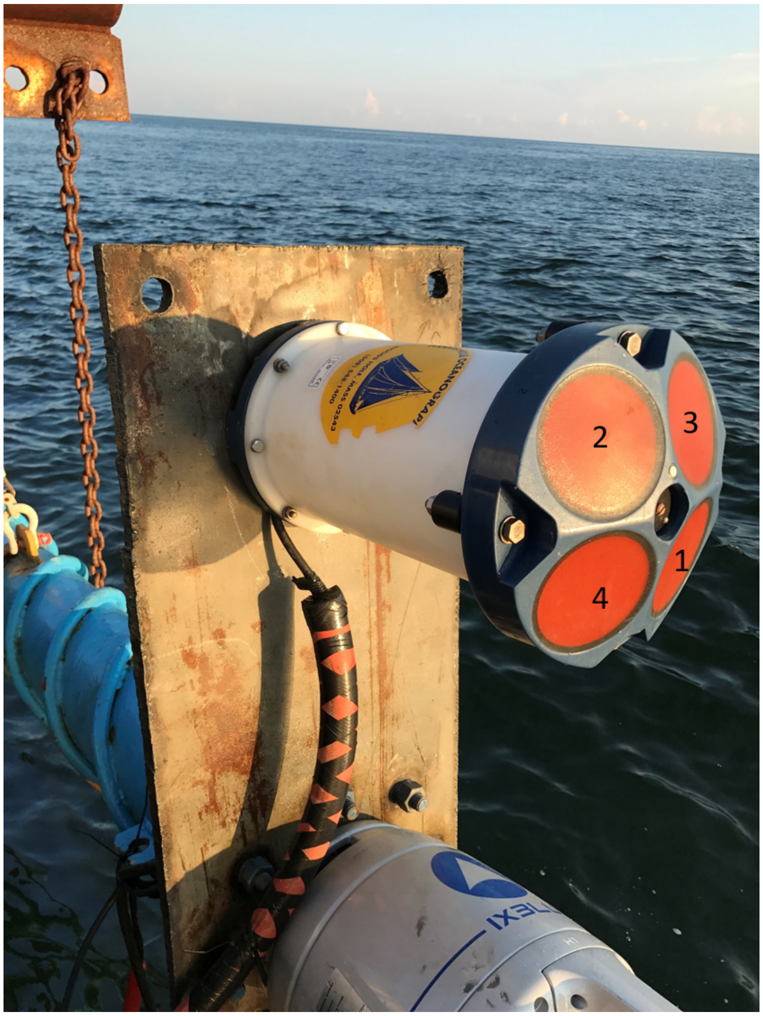

Figure 4.5: The orientation of the beams of the ADCP. The ADCP is pointing towards the bow of the vessel and is on the port side of the vessel in this image. The beams are labeled 1-4, with beam 3 the ”forward” beam in beam coordinates.

in rejection of measurements below 77.2 m in the second survey. Both surveys revealed a velocity profile with gradually decreasing magnitude current with depth (Figure 4.6). The ADCP survey performed after the WBT survey showed a stronger shallow current (from 20 to 60 meters depth). The two surveys measured current directions that were consistent with each other, within 10 ° over the upper 77.2 m of the water column where both surveys reported valid results. For each survey, the current direction varied by as much as 15° as a function of depth. This variation in depth contributes to difficulty in steering track lines that were constantly ensonifying the entire plume during the down-stream passes as seen in Fig 4.4A. Depths measured only by the pre-WBT ADCP survey (83.2 - 95.2 m) show a deep water, low magnitude, current 90° offset from the shallower currents heading to the southeast. Because of the close agreement in magnitude and direction of flow between the two surveys,the profiles were averaged together to approximate the current during the WBT survey. For depths greater than 77.2 m, the values from the pre-WBT ADCP survey were used.

4.4 plume Origin

The WBT survey lines run parallel to the nominal flow direction, or down-stream lines, were used to determine the origin of seeps. Nine down-stream seep survey lines were run over the downed platform. TS was averaged over a five meter depth bin between 108 - 113 m depth, at a height just above the platform (Fig 4.4). The very strong backscatter from the downed platform masks any signal from the plume at greater depths, and therefore the origin is determine for the height above the platform. Average TS in the five meter depth bin was computed for all pings within a 120 m east-west by 70 m north-south area A three dimension local linear interpolation was fit to the depth averaged TS as a function of position (Fig. 4.7). The interpolation revealed the presence of two main peaks, potentially due to the presence of two seeps. Peaks of the interpolation are defined as points within 3dB of the maximum TS. The center of mass of each of the two peaks was found to determine the “origin” of each seep. At a range of 110.25 meters, the beam has a diameter of 10 meters, and the location of the peaks of the interpolation have a maximum accuracy of 10 meters. The northern seep origin according to the interpolated data is located at 28.93728 N x -88.96948 W ±10 m and the southern seep origin at 28.93714 N x -88.96950 W ±10 m. The two seep origins are 15.5 meters apart. The two distinct seeps will be referred to as seeps, while when discussing the two seeps together it will be referred to as the ”plume”. The seep origins are an estimate of the position of the seeps at the center of the depth bin (110.25 m), and not an estimate of the position of the seeps on the seafloor.

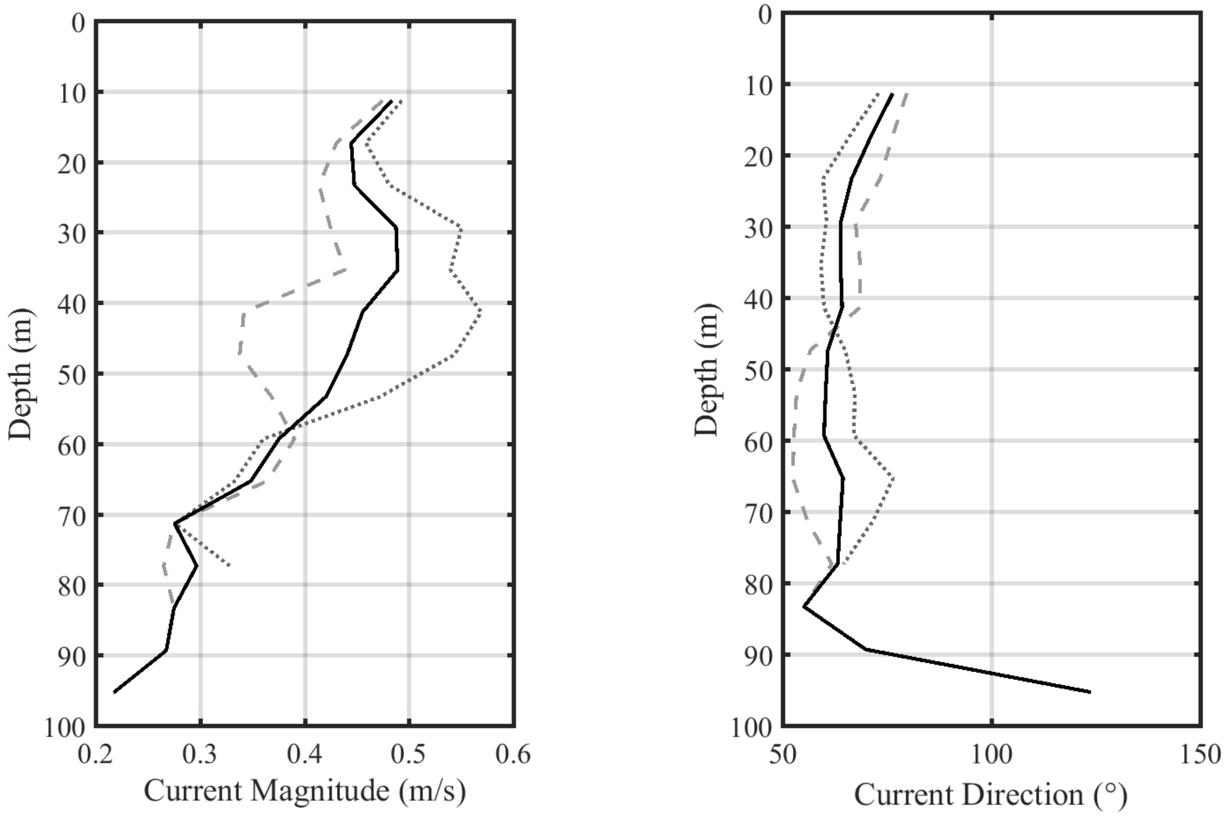

(a) (b)

Figure 4.6: ADCP survey results. (A) the magnitude of the current for the survey run before the WBT survey (grey dashed line) and ADCP survey run after the WBT survey (grey dotted line). The last good depth of the ADCP for the survey before the WBT survey was 95.2 meters and 77.2 meters for the ADCP survey after the WBT survey. The two surveys were averaged together to estimate the current over the WBT survey period (black sold line) for depths less than 77.2 m. For greater depths the pre-WBT survey measurements were used. (B) the direction of the flow as a function of depth varied by about 15 ° for most the water column for the surveys conducted before the WBT survey (grey dashed line), after the survey (grey dotted line) and the mean of the two surveys (solid black line). At depths measured only by the pre-WBT survey, there appears to be a low magnitude current to the southeast, about 90 ° offset from the upper water column.

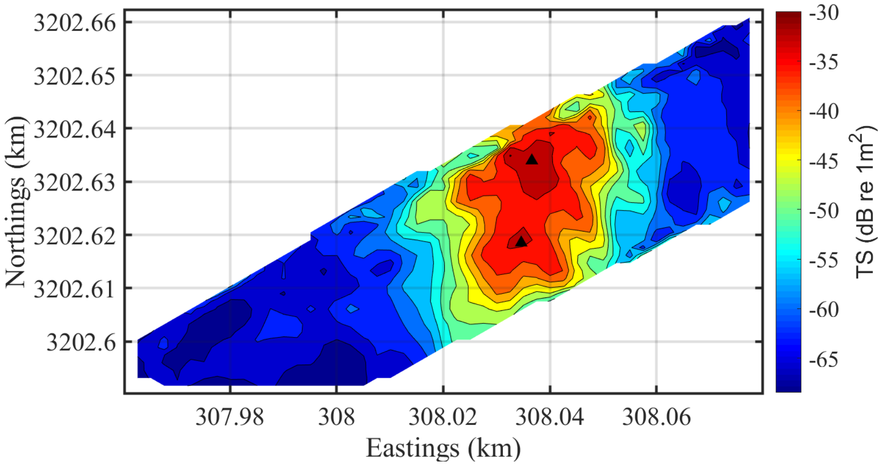

Figure 4.7: Linear interpolation of the TS averaged over 108 - 113 m depth for the area surrounding the downed platform. The black triangles indicate origins of the two seeps. The origins are the areas of maximum backscatter at depths immediately above the downed platform. The platform itself masked the return from the seep at depths below 113 m. Contour lines are equal a change of 3 dB.

4.5 Phase Angle

The split-beam echo sounder used in this experiment uses the phase difference of the backscatter to determine the location of a target within the beam. For a discrete target occupying a space smaller than the beam footprint, this angle information shows how the target moves relative to the position of the echo sounder. When crossing over a stationary target, the along-track beam angle will go from the minimum angle as the target enters the beam and the angle will increase as the target crosses the beam to the maximum angle before the target is no longer detected. Targets were limited to beam angles within ±5°. The beam angle information for cross-sectional passes over the plume agrees with the plume origin determination of two distinct individual seeps. Figure 4.8 shows the beam angle for a pass over the plume. The first seep goes from a negative angle to positive as the vessel moves over the seep and then the beam angle transition repeats for the second seep. This adds further evidence that there are two distinct seeps in the water column emanating from the seep origins discussed above.

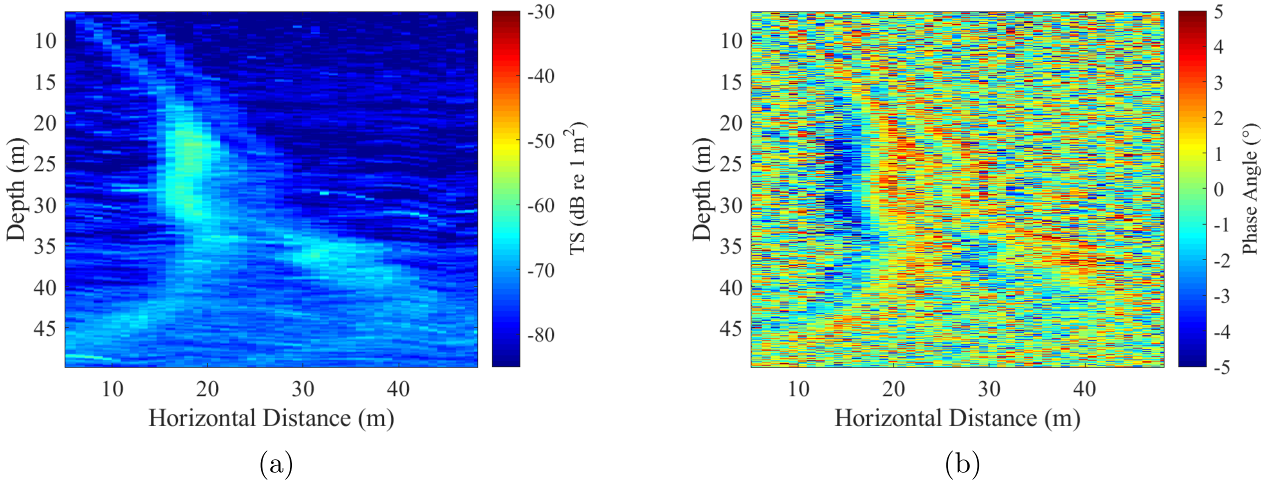

(a) (b)

Figure 4.8: A. A zoomed in version of the echogram in Figure 4.3D focused on the seeps. B. The phase angle for the seeps as the vessel crosses over them. The angle goes from negative to positive as the seep transitions across the beam, and then the transition from negative to positive repeats for the second seep. Combined with the seep origin analysis, this indicates the presence of two distinct seeps in the water column.

4.6 Rise Rate

The depth of the plume as a function of distance downstream, determined by perpendicular passes over the plume, or ”cross sectional passes” was used to determine the rise rate. For an individual pass, the minimum depth of the plume represents the fastest rising targets, while the maximum depth of the plume represents the slowest rising targets. Echograms of the cross sectional passes were visually analyzed to determine the top and bottom of the plume at increasing distances downstream.

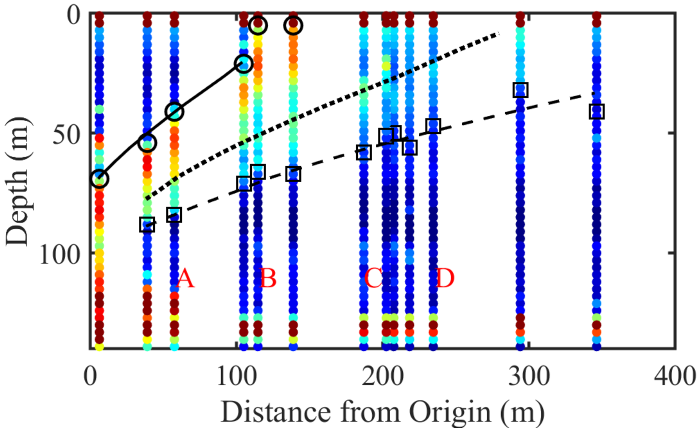

Figure 4.9: The visually picked top (black triangles) and bottom (black squares) of the plume at distances from the first pass over the plume where the plume was above the last good depth of the ADCP. The depth of a target as a function of distance from the first pass account for the depth dependent current for a target rising with a rise rate of 23.2 cm/s (solid black line), 12 cm/s (dotted black line), and 6.7 cm/s (dashed black line). The plume extents and target trajectories are overlaid on the TS ($\hat{TS}$) averaged in a 3 meter depth bin and for all pings containing the plume at each perpendicular pass. The letters, to the right of the integrated TS column they represent, correspond to the echograms in Fig 4.3.

Analysis of the rise rate was limited to depths within the valid depth range of the ADCP. The maximum depth range of the ADCP was 95.2 meters, and rise rate was determined from cross sectional passes over the plume where the bottom of the plume was above the maximum depth range of the ADCP. Therefore, the starting point for the rise rate calculations was the first pass where the bottom of the plume was within the valid measurements of the ADCP (95.2 m), and this starting point is referred to as the “first pass”. Analysis was also limited to a minimum depth of 8.2 meters - the top of the shoalest six meter deep ADCP depth bin centered at 11.2 meters. The maximum rise rate was determined by fitting a line to the top of the plume as a function of distance from the first pass. A line was also fit to the bottom of the plume as a function of downstream distance to determine the minimum rise rate.

The slope of the fit line represents the vertical distance, Δz that a target rose over the horizontal distance traveled Δx. Δx and Δz represent the distance between two points, (x_1, z_1) and (x_2, z_2) on the fit line. The time that it took for a target to travel Δx was determined by dividing the horizontal distance traveled by the horizontal current measured by the ADCP at a given depth ($u(z)$),

$$\Delta t(z) = \frac{\Delta x}{u(z)}, \tag{4.4}$$

where $\Delta t(z)$ is the time it took for a target to travel Δx. The horizontal current, $u(z)$, used in the calculation for a given Δx was the ADCP depth bin closest to the depth of the first point, z_1. Δx was one meter in order to maintain a Δz less than half of a ADCP depth bin (6 m) between any two points on the fit line. The rise rate ($w(z)$) was then calculated according to,

$$w(z) = \frac{\Delta z}{\Delta t(z)}. \tag{4.5}$$

The average rise rate of the top of the plume was 21.3 ± 2.4 cm/s and the average rise rate of the bottom was 6.3 ± 1.3 cm/s. To determine the rise rate at depths other than the top or bottom of the plume, it was assumed that the rise rate was linearly distributed between the maximum and minimum depth of the plume.

For the first pass, the maximum rise rate was the rise rate of targets at a depth of 54 meters (the top of the plume) and the minimum rise rate was the rise rate for targets at the bottom of the plume, 90 meters. It was assumed that rise rates between the maximum and minimum were linearly distributed across depths between 90 and 54 meters, at the location of the first pass; 36 m downstream of the origin of the northern seep. The linear distribution of rise rates was used to determine the depth at the first pass, z_o associated with a given rise rate, w. For example, droplets with a rise rate of w = 6.3 cm/s, had an initial depth of $z_o =$ 90 meters, while droplets with a rise rate of w = 11.3 cm/s had an initial depth of $z_o = 80$ meters. The depth, z_r, of a target at range downstream, r, was then calculated according to,

$$z_r = (\sum_{i=1}^{r} \frac{w}{u_{z_{i-1}}} \Delta x) + z_o, \tag{4.6}$$

where $u_{z_{i-1}}$ is the horizontal velocity at depth z_{i-1}, and Δx is 1 meter. The distance, Δx, of each increment of z_i is limited to 1 meter so that the distance risen is less than half of an ADCP six meter bin. Figure 4.9 shows the depth of a target with a constant rise rate as it moves downstream with three rise rates; the average rise rate from the fit to the top of the plume (21.3 m/s), a rise rate of 11.3 cm/s (the maximum rise rate for oil droplets: see Droplet and Bubble Size) and a rise rate equal to the average rise rate for the fit to the bottom of the plume, 6.3 cm/s. To determine if the top and bottom of the plume were rising with a constant rise rate, the fit was computed between the predicted depth of a target (equation 4.6, solid and dashed black lines in fig 4.9) and the top and bottom of the plume determined visually (circles and squares in fig 4.9). The top and bottom of the plume had r^2 values of 0.99 and 0.91 and p-values equal to 3.7×10^{-3} and 1.5×10^{-5} respectively.

4.7 Oil and Gas Material Properties

Information on the material properties of oil and gas at this seep site was unavailable. To model the rise rate and backscatter from oil droplets and gas bubbles likely to be present in the plume, it was assumed that the oil had the same properties as Angolan Xikomba (see Loranger *et al.* (2018) and Loranger *et al.* (In review)). For gas bubbles it was assumed that the bubbles were comprised of pure methane, and that there was no diffusion of gases into or out of the bubble so that the bubbles were pure methane throughout the water column. These assumptions have the potential for significant impacts on the results of this study, however, without information on the material properties at this site, the assumptions are necessary.

4.8 Droplet and Bubble Size

Models of the rise rate of fluid particles (both liquid oil droplets and gaseous methane bubbles) were inverted to determine the rise rate of oil droplets and gas bubbles in the plume predicted to be present in the plume. Zheng & Yapa (2000) derived an integrated approach to determining the rise rate of spherical and non-spherical bubbles and droplets from correlation formulations developed by Clift *et al.* (1978) for bubbles and droplets in contaminated fluids. The equations for rise rate encompass three different shape regimes; spherical, ellipsoidal and spherical-cap. For spheres the ambient fluid viscosity is the most important factor determining rise velocity, and for spherical-cap particles the rise velocity is driven by the density contrast between the bubble or droplet and the ambient fluid.

For ellipsoidal particles, internal circulation within the particle plays an important role in determining the rise rate. For oil droplets the ratio of target viscosity to the viscosity of the ambient fluid is assumed sufficiently high to inhibit internal circulation. For gas bubbles, on the other hand, the viscosity is much lower in the target, and internal circulation can influence rise rate. However when surfactants are present, they can adhere to the bubble surface and retard the rise rate of bubbles by immobilizing the bubble surface thereby inhibiting internal circulation Clift *et al.* (1978). The impact of contamination on the rise velocity is dependent on the identity of the surfactants and their concentration. As the concentration of surfactants in the ambient fluid increases the rise rate decreases until contaminants reach a critical concentration. At the critical concentration, internal circulation ceases and the rise rate of the bubble approaches the rise of a solid sphere (Kulkarni & Joshi, 2005). Zheng &

Yapa (2000) compared the correlation formulations from Clift *et al.* (1978) to experimental measurements of air and carbon dioxide bubbles rising in tap water and found that surfactants in tap water were present in sufficient quantity to result in rise velocities described by the equations for contaminated bubbles with no internal circulation. For this study it was assumed that the ambient seawater had sufficiently high concentrations of surfactants to be beyond the critical concentration, and therefore rise velocities of ellipsoidal bubbles can be described by the equations for contaminated bubbles. Given the highly productive waters in the area surrounding the plume combined with the likelihood of a high sediment load due to the proximity of the site to the mouth of the Mississippi River it is likely that there were sufficient surfactants to be beyond the critical concentration.

The equations in Zheng & Yapa (2000) were calculated for the physical properties of methane gas as a function of the pressure at that depth. A separate solution to the equations exists for each depth, determined by the density of methane as a function of hydrostatic pressure. The bubble size associate with a rise rate at a given depth is therefore the size of a bubble with density equal to the density of methane at hydrostatic pressure. Oil droplets are assumed to be incompressible. It was conservatively assumed that the maximum expected droplet radius for oil droplets was 3 mm (Zhao *et al.* , 2014), the droplet size corresponding to the maximum rise rate of 11.3 cm/s (Figure 4.10). It is possible that larger oil droplets are present at the higher rise rates, and if this were the case, the estimate of oil volumetric flow rate would be biased low. The minimum oil droplet radius, the radius associated with the lowest rise rate (6.3 cm/s), was 1.2 mm. The equivalent bubble size for the same rise rates (11.3 and 6.3 cm/s) was 0.49 and 0.29 mm respectively. The transition between the spherical and ellipsoidal regimes is a radius of 0.5 mm (Clift *et al.* , 1978). Therefore, all droplets were in the ellipsoidal regime, and all bubbles with rise rates below 11.3 cm/s were in the spherical regime. For rise rates above 11.3 cm/s, it is assumed that all targets must be bubbles since the rise rate exceeds that predicted for all oil droplets. The bubble radius for the maximum rise rate (21.3 cm/s) 1.2 mm, and therefore bubbles within the plume are predicted to vary in size from 0.29 to 1.2 mm.

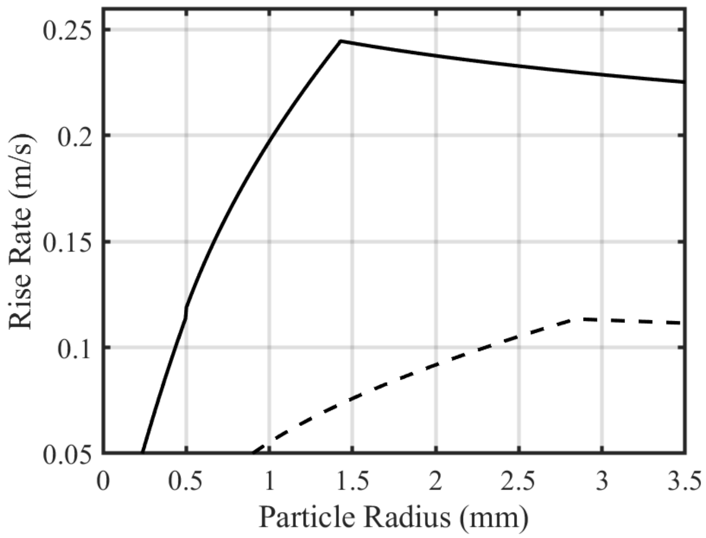

Figure 4.10: The rise rate and target radius predicted by Zheng and Yapa (2000) for oil droplets (dashed line) and methane bubbles (solid line) in seawater at a depth of 40 meters. The maximum predicted rise rate for droplets was 0.113 m/s which equates to a 2.82 mm radius droplet, and 0.49 mm bubble. The minimum rise rate determined from the fit to the echo sounder data was 0.063 m/s which equates to a 1.17 mm droplet and a 0.29 mm bubble. The maximum rise rate from the fit to the echo sounder data was 0.216 m/s, equivalent to a 1.16 mm bubble.

4.9 Volumetric Flow Rate

The acoustic backscatter from the cross sectional passes was used to determine the number of targets of a given size in the plume. The raw wave forms from the four quadrants of the ES120 recorded by the WBT were summed and match filtered to obtain the match filtered signal, S_{mf}. S_{mf} was calibrated using the match filtered calibration factor, C_{mf}. The target strength (TS) in an acoustic sample is equal to the sum of the backscattering cross section, $\theta_{bs,i}$ from each of the i targets in the sample such that,

$$TS = 10log_{10}(\sum_{i=1}^{N} \sigma_{bs,i}), \tag{4.7}$$

where N is the total number of targets in the sample volume. The sum on the right-hand side of equation 4.8 is the total backscatter from all X targets, σ_T,

$$\sigma_T = \sum_{i=1}^{X} \sigma_{bs,i}. \tag{4.8}$$

σ_T, is the backscatter from all sources in the ensonified volume including the backscatter from the targets of interest, σ_t, as well as the contribution from other background scatterers (such as biological scatterers) and other sources of noise, σ_{bg}, such that

$$\sigma_T = \sigma_t + \sigma_{bg}. \tag{4.9}$$

For weak scatterers, such as oil droplets, the contribution from σ_{bg} to the total scattering can be significant. For a bimodal distribution of σ_t, such as a scattering volume comprised of oil droplets and methane bubbles, the sum can be estimated from

$$\sigma_t \approx N\overline{\sigma}_{bs,N} + M\overline{\sigma}_{bs,M}, \tag{4.10}$$

where $\overline{\sigma}_{bs,N}$ is the average backscattering cross sectional area of the N targets of the first mode of the distribution, and $\overline{\sigma}_{bs,M}$ is the average backscattering cross sectional area of the M targets of the second mode. While σ_{bg} is the backscatter from all other scatterers in the ensonified volume,

$$\sigma_{bg} \approx P\overline{\sigma}_{bs,P}, \tag{4.11}$$

where P is the total number of scatterers other than the targets of interest.

The total volumetric flow rate, Q, of targets through the sample volume is then equal to,

$$Q = \Big(N\frac{4}{3}\pi\frac{a_N^3}{h}w\Big) + \Big(M\frac{4}{3}\pi\frac{a_M^3}{h}w\Big), \tag{4.12}$$

where a_N is the radius of targets in one of the modes and a_M is the radius of targets in the other distribution, h is the height of the sample volume and w is the rise rate. For oblate spheroids such as oil droplets of the size determined by the rise rate, the radius a is the radius of a sphere of equivalent volume to the oblate spheroid.

Weber & Ward (2015) showed that, for a deterministic signal target,

$$\sigma_{bs} = \frac{|S_{mf}|^2}{C_{mf}} \frac{r^4}{e^{-4ar}}, \tag{4.13}$$

where S_{mf} is the matched filter signal recorded by the echo sounder, C_{mf} is the matched filtered correction factor, r is the range to the target in meters and a is the absorption coefficient in nepers/m. For multiple scatterers, the right hand side of the equation stays the same (it is the calibrated and range correct signal recorded by the echo sounder) but the left becomes σ_T. Combining equation 4.13 modified for multiple scatterers with equation 4.9, σ_t for a matched filter calibrated signal is,

$$\sigma_t = \frac{|S_{mf}|^2}{C_{mf}} \frac{r^4}{e^{-4ar}} - \sigma_{bg}, \tag{4.14}$$

The Fourier transform of S_{mf} over 0.5 meter depth bins within the plume area was calculated encompassing 63 samples and a frequency spacing of about 1.5 kHz. The intensity as a function of frequency for all pings within a depth bin was averaged to determine the frequency dependent average match filtered signal as a function of depth $\hat{S_{mf}}$. $\hat{S_{mf}}$, was converted to σ_t, as a function of frequency according to equation 4.14 with the absorption coefficient, a for each frequency determined by (Francois & Garrison, 1982).

To prevent integrating the backscatter from scatterers present in the water column that are not part of the plume, σ_N was removed from σ_T using a method similar to that described by De Robertis & Higginbottom (2007). The same process for calculating σ_t described above was used, but for pings adjacent to the plume, where the plume was not present. $\hat{S_{mf}}$, was calculated by averaging S_{mf} in 0.5 m depth bins and over 104 pings adjacent to the plume to determine the total backscatter contribution from ambient noise σ_N, as a function of frequency (fig 4.11). σ_N was then subtracted from σ_T to obtain the backscattering cross sectional area of all targets of interest in the sample volume, σ_t

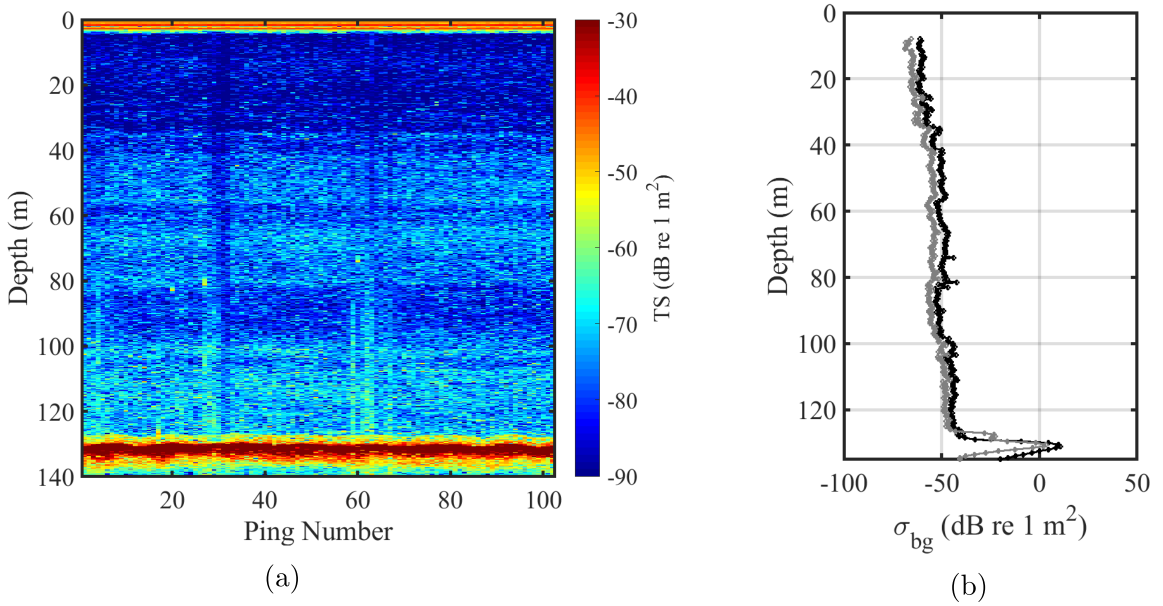

(a)

(b)

Figure 4.11: a. an echogram of the 104 pings used in the noise calculation showing the stratified water column. b. Noise profiles for the minimum frequency (94 kHz, gray) and maximum frequency (153.5 kHz, black) average into 0.5 meter depth bins and over 104 pings.

For the plume in this study, σ_t was assumed to be comprised of N oil droplets and M methane bubbles. $\overline{\sigma}_{bs,N}$ was the predicted average backscatter from methane bubbles, and $\overline{\sigma}_{bs,M}$ the predicted average backscatter from oil droplets. Backscatter from oil droplets and gas bubbles were predicted by two different models. Backscatter from gas bubbles was modeled by the model derived by (Clay & Medwin, 1977), with a modification to the natural frequency derived by (Ainslie & Leighton, 2009). For oil droplets, the distorted wave Born approximation (DWBA, Stanton *et al.* (1998)) was used. Loranger *et al.* (In review), showed that predicting the broadband backscatter from oblate spheroidal shaped medium crude oil droplets by the DWBA resulted in minimal errors in predicting the volume of droplets. The models were computed for oil droplets and gas bubbles with the properties listed above and for the size determined by the rise rate at a given depth.

For each cross sectional pass, the plume was broken up into two rise rate regimes; a gas

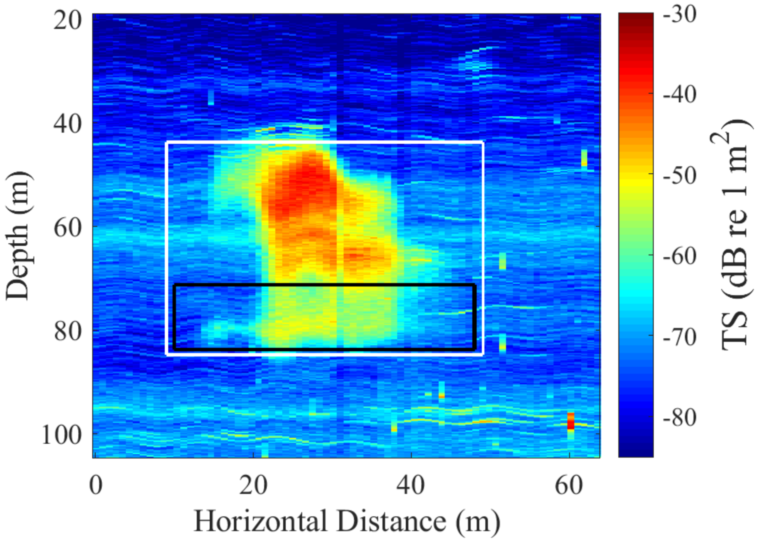

Figure 4.12: A section of the echogram in Fig 4.3A zoomed in to the plume area. The black boxes outlines the area of the plume predicted to contain oil droplets. Targets in this area rose with a rise rate equal to or less than 11.3 cm/s. The white box outlines the area of the plume predicted to contain gas bubbles. There is no predicted maximum or minimum rise rate for methane bubbles according to (Zheng & Yapa, 2000) and therefore the entirety of the plume is predicted to potentially contain gas bubbles.

only regime and a regime where the rise rate was below the maximum rise rate of oil droplets (11.3 cm/s) and therefore both oil droplets and methane bubbles could occur (fig 4.12). For the methane bubble only rise rate regime, only the end member of 100% of the volume in the plume comprised of methane bubbles was considered. In the oil droplet rise rate regime, the condition that 100% of the volume was comprised of oil and that 100% of the volume was comprised of methane were considered. In this regime where oil and gas could both be present, different ratios of the total volume of gas to total volume of oil ratios (GOR) were also considered. For each 0.5 meter depth bin in each cross-sectional pass, the number of scatterers (N and M) was iteratively increased and the mean square error between the right and left sides of equation 4.10 determined. N and M ranged from 1 to 1,000,000 in increments of 10. The value of N and M that produced the minimum mean square error for each gas to oil volume ratio was determined to be the number of targets at a given depth (4.13). There was no significant difference between the mean square errors for the different

GOR's.

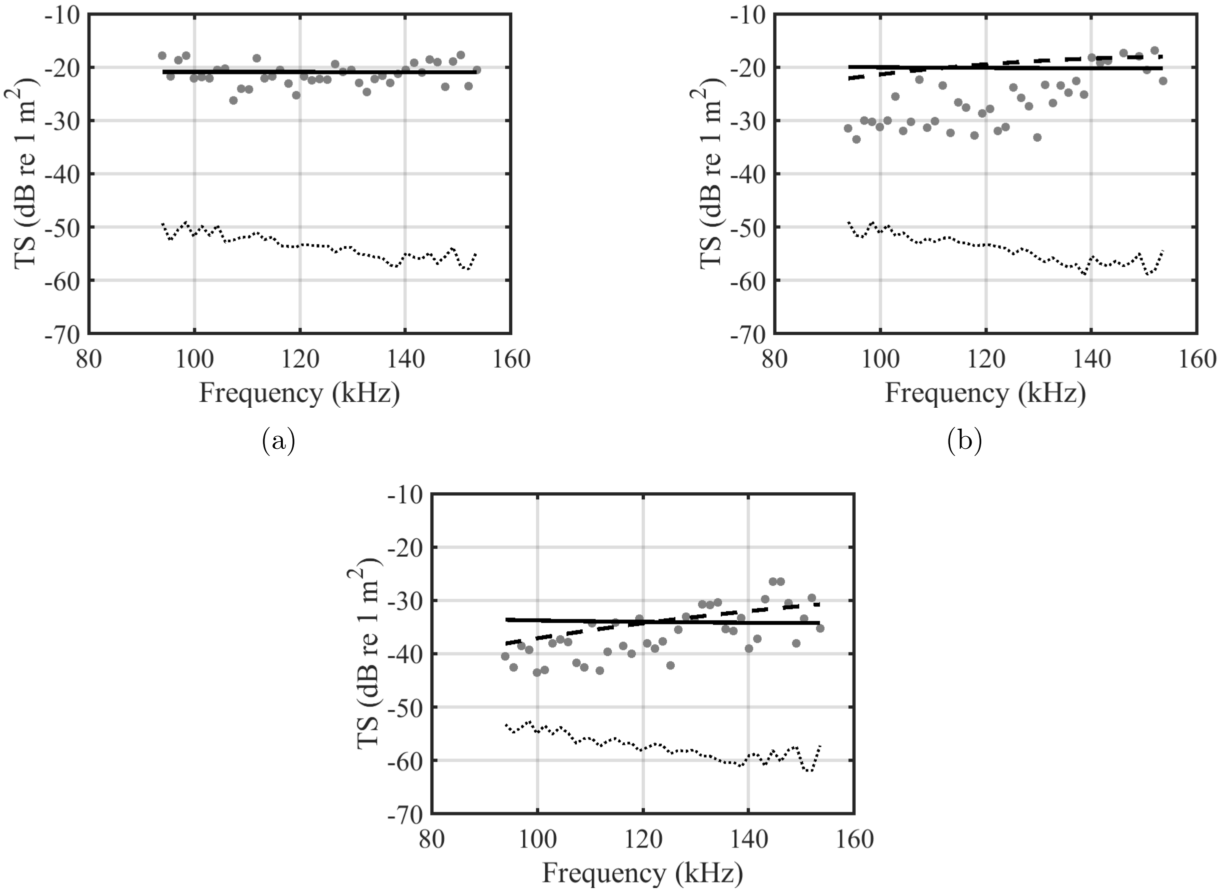

(a)

(b)

(c)

Figure 4.13: The measured frequency dependant target strength (σ_t gray dots) compared to the predicted backscatter for the scenario where all targets are methane bubbles ($\overline{\sigma}_{bs,N}N$, solid black line) and where all targets are oil droplets ($\overline{\sigma}_{bs,M}M$, black dashed line) for a single cross sectional pass. (a) is a rise rate of 20.2 cm/s and bubbles radius 1.04 mm, (b) is a rise rate of 10.3 cm/s, bubble radius of 0.45 mm and droplet radius 2.24 mm and (c) is a rise rate of 6.9 cm/s, bubble radius 0.31 mm and droplet radius 1.33 mm. There are no droplets predicted for (a) because it is in the bubble rise rate regime - the rise rate is greater than the maximum predicted bubble rise rate (11.3 cm/s). The black dotted line is the noise level, σ_{bg}, for the same depth as the targets.

The number of targets at each depth was used to determine the average Q of the two seeps at each depth according to equation 4.12. Q at each depth were then multiplied by two to get the total Q from both seeps and summed for across all depths to determine the total average Q from the two seeps in each cross-sectional pass (fig 4.14). No significant relationship was found between Q of oil and distance from the origin or time of cross-sectional pass. The average Q of oil ($\overline{Q}$) for the scenario where all the targets in the oil droplet rise rate regime are oil droplets was 249 barrels / day. It was assumed that the twelve observations (N = 12) of the total Q were sufficient for the central limit theorem to apply and therefore the 95% confidence interval for the estimate of the true mean Q (μ_x) was determined by,

$$Prob\Big[\overline{Q} > \Big(\frac{st_{n;\alpha}}{\sqrt{N}} + \mu_x\Big)\Big] = \alpha, \tag{4.15}$$

where $\overline{Q}$ is the mean of the 12 observations of Q, s is the standard deviation and $t_{n;\alpha}$ is the Student's t distribution for $n = N - 1$ degrees of freedom and at confidence interval α (Bendat & Piersol, 2000). The 95% confidence interval for the total Q of oil was determined to be 341 to 156 barrels/day.

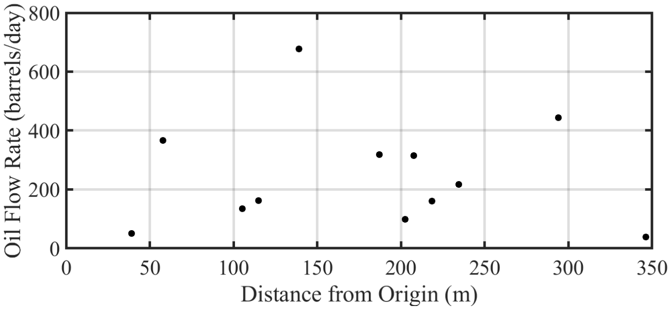

Figure 4.14: The depth integrated flow rate of oil for each cross section of the plume by distance from the northern seep origin.

For methane gas, for the scenario that all targets in the plume were comprised of methane gas the total Q for the entire plume (the gas rise rate regime and droplet rise rate regime) was 13.7 to 3.84 m^3 / day with a mean of 8.78 m^3/day of methane (fig 4.15). The volume of methane was determined for methane at surface temperature and pressure.

The average Q of 249 barrels/day of oil and 8.78 m^3/ day of methane represent the two end members of the possible plume scenarios. For cases where oil and gas were both present, the total Q of methane and oil from the droplet rise rate regime as a function of the GOR of the entire plume is shown in figure 4.16.

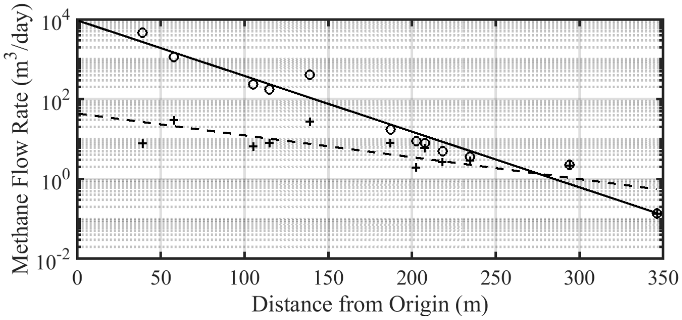

Figure 4.15: The depth integrated volumetric flow rate of methane for each cross section of the plume by distance from the northern seep origin for both rise rate regimes (Black circles) and the oil droplet rise rate regime only (black crosses). The fit lines are also shown for both rise rate regimes (solid black line) and the oil droplet rise rate regime only (black dashed line).

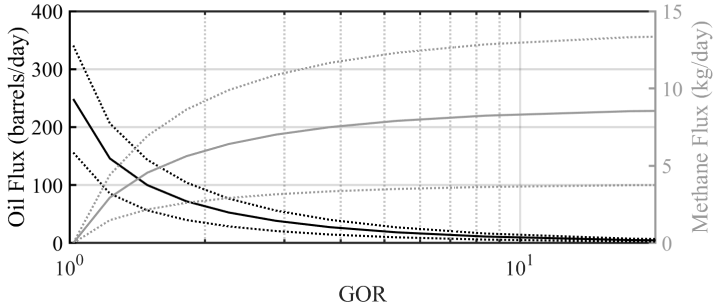

Figure 4.16: The total methane and oil volumetric flow rate from the droplet rise rate regime (rise rate ¡ 11.3 cm/s) required to explain the acoustic observations in that regime for different GOR's. The GOR is the ratio of the volume of gas in the entire plume to the volume of oil in the entire plume. The entire plume includes both the droplet rise rate regime and the bubble rise rate regime, however oil is predict to only be present in the droplet rise rate regime. When the total volume of the droplet rise rate regime is assumed to be oil droplets, the GOR of the entire plume is approximately 1.

4.10 Discussion

Of the two end member scenarios, that the droplet rise rate regime of the plume was comprised of solely methane or solely oil droplets, there are indications that the later is the more probable. The constant rise rate of the bottom of the plume indicates the presence of targets of a constant size. The rise rate of gas bubbles is very sensitive to changes in the bubble size. As bubbles rise, the pressure decreases and compressible gas expands. At the same time, gases dissolve from the bubble to the water column and vice versa. Without information about the chemical composition of the water column and the composition of the bubbles themselves, it is not possible to model this dissolution. However, for bubbles to rise with a constant rise rate from 90 meters to the surface would require expansion of the bubble and dissolution at exactly equal rates - an unlikely scenario. If the targets at the bottom were incompressible oil droplets on the other hand, the size would not change due to changes in pressure. The incompressiblity combined with the decreased sensitivity of oil droplet rise rate to size (Fig 4.10), means that oil droplets would be likely to rise with a constant velocity over the depths in this experiment.

The difference in slope of the total Q as a function of distance between the entire plume and the oil droplet rise rate range for gas bubbles indicates that gas is dissolving as it rises the water column, however in the droplet rise rate regime where gas bubbles are smaller this volume loss occurs much less rapidly. The top of the plume reaches the surface at about 115 meters downstream from the northern seep origin, and by this point the total plume has decreased in volume by about two orders of magnitude. In contrast, the droplet rise rate regime of the plume has not decreased in volume at all in the first 150 meters from the origin. The top of the oil droplet rise rate regime does not reach the surface until about 300 meters downstream of the origin. Over that much greater distance, the volume of gas in the droplet rise rate regime has decreased by only one order of magnitude. The difference in the loss of volume for the entire plume compared to the droplet rise rate regime could be due to a difference in the dissolution rate of smaller bubbles in the plume - possibly due to oil coated bubbles - or it is due to the fact that the scatterers in this regime are not methane bubbles like the upper part of the plume. In the oil only scenario the droplets show no change in volume as the plume moves downstream.

The final indication that the droplet rise rate regime is the coincidence of the minimum droplet size and the transition from Rayleigh Scattering to geometric scattering. In the Rayleigh scattering regime (where wavelength is large compared to the radius of the target) the TS decreases rapid for a given frequency (and wavelength) as the size decreases. For oil droplets, this transition occurs around $ka = 1$, where k is the acoustic wavenumber and a is the radius of the target. The smallest droplets (1.4 mm radius) have a $ka = 0.9$ at the maximum frequency (smallest wavelength) of 153.5 kHz. Therefore, the bottom of the plume occurs where droplet size is small enough that targets are in the Rayleigh scattering regime and TS is lower (Figure 4.1). For gas bubbles, the transition to Rayleigh scattering occurs at much lower frequencies - in the 10s of kHz range for the smallest bubbles at the bottom of the plume. Therefore, the distinct bottom of the plume would be unlikely to be due to the decreased scatttering amplitude from smaller droplets, but instead due to a sudden decrease in the number of bubbles below the minimum bubble size.

From figure 4.13, it appears that the slop of the backscatter is a best fit to the shape of the predicted frequency response for the scenario where all targets in the droplet rise rate regime are oil droplets. However, the frequency response of droplets and bubbles was predicted from assumed physical properties. In order to rigorously determine how the frequency response matches the predicted, the material properties of the oil droplets and gas bubbles must be known. Loranger *et al.* (2018) found that small changes in the density and sound speed of oil can results in significant differences between the predicted and measured frequency response for oil droplets, and for this study there exists the potential for significant errors due to differences between the assumed physical properties of the oil and gas and the actual properties.

The estimate of total oil Q does not include Q of oil from bubble coated in oil, and there is the potential for the presence of smaller oil droplets, with ka less than 1 as discussed above that were not detected by the vessel mounted echo sounders.

4.11 Conclusions

The shipboard broadband acoustic system used in this study was capable of detecting and quantifying the Q of hydrocarbons from the sea floor plume site. The plume consisted of two distinct seeps, both of which rose with a constant rise rate. Due to a paucity of information about the physical properties of the oil and gas at this site, it was not possible to use the broadband backscatter to determine the identity of targets with out the potential for significant errors due to the difference between the assumed properties and the actual physical properties. The plume was broken up in to two regimes by the rise rate - the bubble rise rate regime, where the rise rate was greater than the maximum predicted rise rate for oil droplets and therefore only gas was present, and the droplet rise rate regime where oil and gas could both occur. For the assumption that all targets in the droplet rise rate regime were oil droplets, it was estimated that Q of oil was between 156 and 341 barrels of oil per day, with a mean Q of 249 barrels per day. Assuming that all targets in the gas rise rate regime were gas bubbles, the total Q of methane for the entire plume was estimated to be between 3.84 and 13.7 m^3 per day with a mean of 8.78 m^3 per day. Qualitative evidence indicates that targets in the droplet rise rate regime were mostly oil droplets, however, the lack of information on the physical properties precludes the use of broadband backscatter to identify the targets.

Chapter 5

Conclusion

In order to accurately predict the backscatter from oil droplets, it is necessary to determine the material properties that determine scattering, especially sound speed and density, as well as the shape and size of droplets. In chapter two of this thesis new empirical models of the density and sound speed were derived for those properties at oceanographically relevant temperatures and pressures. These models show better agreement with measurements made in chapter 2 as well as with literature values. The improvement in predicting the material properties of oils significantly impacts models of backscatter. These models require only the API gravity to predict the density and sound speed.

In chapter 3, the new models of the density and sound speed were used to inform three scattering models used to predict the broadband backscatter from three different oil droplets of differing size and shape. It was determine that the distorted wave Born approximation and boundary element method, which account for the oblate spheroidal shape of oil droplets, are better predictors of scattering for medium oils. None of the three models used accurately predicted the shape of the backscatter for the heavy oil. This discrepancy is potentially due to changes in the sound speed as a function of frequency not accounted for in this chapter. Further study is required to understand dispersion in oil droplets.

In chapter 4, broadband backscatter was used to estimate the flux from an oil and gas seep in the Gulf of Mexico. Measurements of the physical properties of the oil and gas at this site were not available and this lack of information impeded the use of broadband backscatter to identify scatterers. Despite the lack of information about the material properties, qualitative analysis indicates that the dominant scatterers in the plume were oil droplets.

With an improved understanding of the broadband backscatter from oil droplets it is possible to predict the limit to detection for different echosounders. The detection limit was predicted for the ES120, ES200 and ES333 echosounders used in chapter 3. Two cases of the noise level (NL) were used in determining the detection limit. The first was the case where the shallow high backscattering layer seen in chapter 4 (Fig.4.11) between 40 and 60 meters depth was present through the entire water column. This is to simulate the detection limit when other scatterers, such as the planktonic species that comprise scattering layers, are present in the watercolumn. NL for this case was set to the average NL between 40 and 60 meters (Fig.4.11b) for the center frequency of the transducer (120kHz) in chapter 4. The resulting NL, -57dB was assumed to be the noise level for all the three transducers. For the low noise case, the average noise of the calibration tank was used. It was assumed that NL was constant through the watercolumn and equal to the noise floor at the center frequencies of the transducers for the calibration tank from chapter 3 (Fig 3.6). The resulting noise level at 1 meter for each transducer was -98 dB -95 dB and -88 dB for the ES120, ES200 and ES333 respectively..

The TS was simulated for oil droplets of 1 mm and 3 mm radius with properties equal to ANS oil at 20°C and hydrostatic pressure at depth according to the models derived in chapter 1. The distorted wave Born approximation was used for oblate spheres with eccentricity of 0.4 and 0.6 for the 1 mm and 3 mm droplets respectively (Figure 5.1.

The % volume of oil necessary for detection was determined by rearranging equation 4.14 such that,

$$\frac{|S_{mf}|^2}{C_{mf}} = \sigma_t \frac{e^{-4ar}}{r^4}, \tag{5.1}$$

The limit of detection was set to a signal to noise ratio of 7 dB (the intensity of the signal

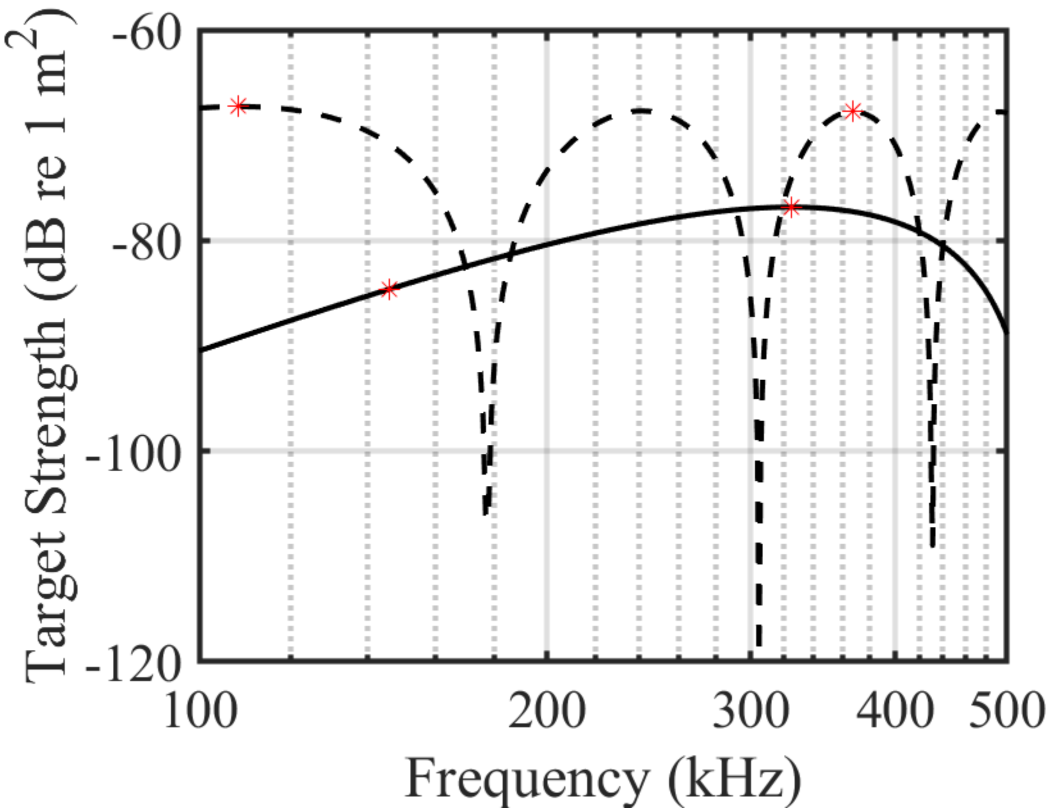

Figure 5.1: The frequency response for a 1 mm (solid black line) and 3 mm radius (dashed line) ANS droplet at 20°C and hydrostatic pressure deteremined at depth. The red asterix indicate the peak of the backscatter in the broadband range of the ES120 and ES333 described in chapter 3.

must be 5 times the intensity of the noise), where

$$\frac{|S_{mf}|^2}{C_{mf}} > 5\sigma_N, \tag{5.2}$$

and σ_N is the scattering from targets other than oil droplets present in the ensonfied volume as described in equation 4.9. Combining equation 5.1 with equation 4.10 modified for a normal distribution of scatterers and equation 5.2 and rearranging, the total number of droplets necessary for detection, N is results in,

$$N > \frac{(5\sigma_N r^4)}{(e^{-4ar})\,\overline{\sigma}_{bs,N}}, \tag{5.3}$$

The number of droplets per unit volume was then calculated by dividing N by the ensonified volume V. For a downward looking echosounder that has been matched filtered V was calculated according to,

$$V = \pi[rsin(\frac{\theta_{2eq}}{2})]^2\frac{cT}{2}, \tag{5.4}$$

where θ_{2eq} is the two-way equivalent beam-width of the transducer, c is the sound speed and T is length of the analysis window. θ_{2eq} was five degrees, T was set to the 4.7 milliseconds, (equal to a sample range of 0.5 meters for the three transducers). The percent oil by volume of seawater (V_{oil}) was determined according to,

$$V_{oil} = \Big[\Big(\frac{N}{V}\Big)\frac{4}{3}\pi a^3\Big]x\ 100 \tag{5.5}$$

The result is the volume of oil, expressed as the percent of the total ensonified volume, necessary for the SNR to be 7 dB at distance r (Fig 5.2). At a % oil by volume of 100% the volume of oil necessary for detection is equal to the ensonified volume.

There are a number of ways to decrease the percent volume of oil necessary for a detec-

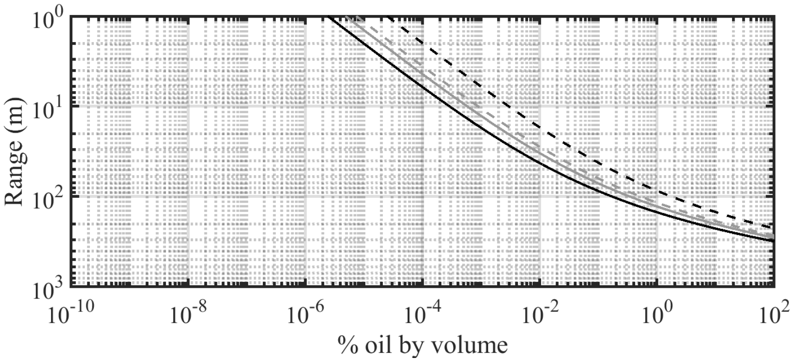

(a)

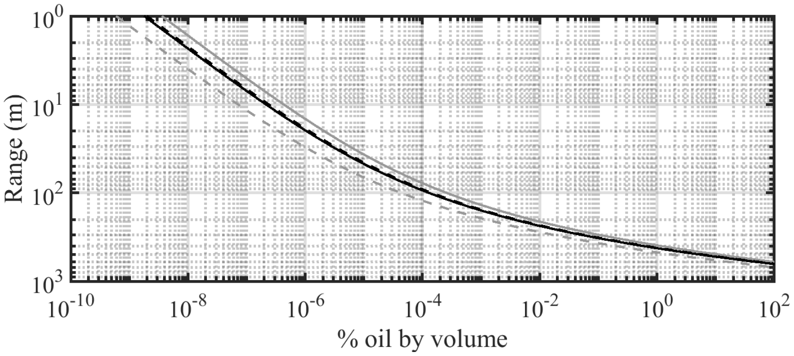

(b)

Figure 5.2: The percent of oil per volume of seawater require for detection as a function of range at 120 kHz (solid lines) and 333 kHz (dashed line) for 1 mm droplets (gray lines) and 3 mm droplets (black lines). The detection ranges are computed for environments with noise equal to the (a) the noise level averaged between 40 and 60 meters (Fig.4.11b) and (b) is the detection range for the noise levels for each transducer from the calibration tank in chapter 3.

tion. The first is to decrease the range from the echo sounder to the target. By mounting broadband echo sounders on ROV's AUV's or towed platforms, the instruments can be moved closer to the targets. With echo sounders mounted on vehicles in the water column, it is also possible to evaluate seeps at select depths. In Figure 4.11, the noise profile has layers of relatively high and low scattering. These layers can be identified by a preliminary surface survey, and evaluation of the seep can focus on low scattering layers, such as between 80 and 100 m in figure 4.11.

Moving the instruments closer to the targets will also serve to decrease the ensonified volume, V. For weak scatterers such as oil droplets the presence of other scatterers - such as plankton, oceanic microstructure and gas bubbles, can mask the signal from the weak scatterer of interest. With a smaller ensonified volume, fewer of the other scatterers are present are the likelihood of detecting oil increases. V is also decreased by decreasing T the analysis window. For broadband pulses, the range resolution scales as $1/B$, where B is the bandwidth, as opposed to $\tau/2$, where τ is the pulse length, which is the scale of the range resolution for narrowband pulses (Weidner *et al.* , 2019). With more fine range resolution, smaller analysis windows can be used to decrease V. However, decreasing the number of samples will also decrease the frequency resolution when evaluating the broadband backscatter in the frequency domain.

Decreasing the percent volume of oil required for a detection requires maximizing the SNR. Broadband matched filtered signals show an improvement of $2B\tau$ in SNR (Chu & Stanton, 1998; Turin, 1960). The SNR could be improved by with wider bandwidth or increased pulse length.

The final consideration for evaluating oil in the marine environment and maximizing the likelihood of detecting these weak scatterers is to use the appropriate frequency. Using the models derived in chapter 2 and the distorted wave Born approximation verified in chapter 3 to predict the frequency dependent backscatter, users can select frequencies at the peak of the backscatter curve. Higher frequency systems have wider bandwidth, and therefore increase the likelihood of have some portion of that band in the peak of the frequency response, however attenuation is also greater at higher frequencies. A high frequency system should be combined with a lower frequency system where oil droplets are within the Rayleigh scattering regime. As the frequency decreases, the discrepancy between the TS of gas bubbles and oil droplets at a give frequency increases (Figure 1.1). At low frequencies oil would need to be present at incredibly high volumes for detection, where as gas bubbles would be readily detected. A detection in the high frequency but no detection at low frequency would indicate oil droplets (or some other liquid scatterer) and not gas bubbles. Using low and high frequencies, therefore, could be used to differentiate between oil and gas. The frequencies used for evaluating oil in the marine environment should be carefully chosen based on the predicted backscatter and distance from the transducers to the target of interest.

Bibliography

Abbriano, Raffaela, Carranza, Magdalena, Hogle, Shane, Levin, Rachel, Netburn, Amanda, Seto, Katherine, Snyder, Stephanie, & Franks, Peter. 2011. Deepwater Horizon Oil Spill: A Review of the Planktonic Response. *Oceanography*, **24**(3), 294–301.

Ainslie, Michael A., & Leighton, Timothy G. 2009. Near resonant bubble acoustic cross-section corrections, including examples from oceanography, volcanology, and biomedical ultrasound. *The Journal of the Acoustical Society of America*, **126**(5), 2163–2175.

Alvarez, Nicolas J., Walker, Lynn M., & Anna, Shelley L. 2010. A Microtensiometer To Probe the Effect of Radius of Curvature on Surfactant Transport to a Spherical Interface. *Langmuir*, **26**(16), 13310–13319.

Anderson, V.C. 1950. Sound Scattering from a Fluid Sphere. *Journal of the Acoustical Society of America*, **22**(4), 426–431.

ASTM A276 - 98b. 2017. Standard Specification for Stainless Steel Bars and Shapes. *ASTM Standard A582/A582M*.

ASTM D7867-13. 2013. *Standard Test Methods for Measurement of the Rotational Viscosity of Paints , Inks and Related Liquid Materials as a Function of Temperature.* Tech. rept. ASTM International, West Conshohocken, PA.

Ball, Stuart J., Goodwin, Anthony R.H. H, & Trusler, J.P.Martin P M. 2002. Phase behavior and physical properties of petroleum reservoir fluids from acoustic measurements. *Journal of Petroleum Science and Engineering*, **34**(1-4), 1–11.

Bassett, Christopher, Lavery, Andone C., Maksym, Ted, & Wilkinson, Jeremy P. 2016. Broadband acoustic backscatter from crude oil under laboratory-grown sea ice. *The Journal of the Acoustical Society of America*, **140**(4), 2274–2287.

Batzle, Michael, & Wang, Zhijing. 1992. Seismic properties of pore fluids. *Geophysics*, **57**(11), 1396–1408.

Belogol'skii, V, Sekoyan, S, Samorukova, L, Stefanov, S, & Levtsov, V. 1999. Pressure dependence of the sound velocity in distilled water. *Measurement Techniques*, **42**(4), 406–413.

Bendat, Julius S., & Piersol, Allan G. 2000. *Random Data: Analysis and Measurement Procedures.* New York, NY: Wiley.

Beyer, Jonny, Trannum, Hilde C., Bakke, Torgeir, Hodson, Peter V., & Collier, Tracy K. 2016. Environmental effects of the Deepwater Horizon oil spill: A review. *Marine Pollution Bulletin*, **110**(1), 28–51.

Bilaniuk, Nykolai, & Wong, George S. K. 1993. Speed of sound in pure water as a function of temperature. *The Journal of the Acoustical Society of America*, **93**(3), 1609–1612.

Camilli, Richard, Di Iorio, Daniela, Bowen, Andrew, Reddy, Christopher M, Techet, Alexandra H, Yoerger, Dana R, Whitcomb, Louis L, Seewald, Jeffrey S, Sylva, Sean P, & Fenwick, Judith. 2012. Acoustic measurement of the Deepwater Horizon Macondo well flow rate. *Proceedings of the National Academy of Sciences of the United States of America*, **109**(50), 20235–9.

Chaudhuri, Anirban, Osterhoudt, Curtis, & Sinha, Dipen. 2012. An Algorithm for Determining Volume Fractions in Two-Phase Liquid Flows by Measuring Sound Speed. *Journal of Fluids Engineering,*, **Vol. 134**(October), 1–7.

Chu, Dezhang, & Stanton, Timothy K. 1998. Application of pulse compression techniques to broadband acoustic scattering by live individual zooplankton. *The Journal of the Acoustical Society of America*, **104**(1), 39–55.

Chu, Dezhang, Foote, Kenneth G., & Stanton, Timothy K. 1993. Further analysis of target strength measurements of Antarctic krill at 38 and 120 kHz: Comparison with deformed cylinder model and inference of orientation distribution. *The Journal of the Acoustical Society of America*, **93**(5), 2985–2988.

Clay, C.S., & Medwin, H. 1977. *Acoustical Oceanography: Principles and Applications*. New York: John Wiley & Sons.

Clift, Roland, Grace, John R., & Weber, Martin E. 1978. *Bubbles, drops, and particles*. New York, NY: Academic Press.

Coombes, Kevin R., Tsavachidis, Spiridon, Morris, Jeffrey S., Baggerly, Keith A., Hung, Mien Chie, & Kuerer, Henry M. 2005. Improved peak detection and quantification of mass spectrometry data acquired from surface-enhanced laser desorption and ionization by denoising spectra with the undecimated discrete wavelet transform. *Proteomics*, **5**(16), 4107–4117.

Crooke, Emma, Talukder, Asrar, Ross, Andrew, Trefry, Christine, Caruso, Michael, Carragher, Peter, Stalvies, Charlotte, & Armand, Stephane. 2015. Determination of sea-floor seepage locations in the Mississippi Canyon. *Marine and Petroleum Geology*, **59**(jan), 129–135.

Daridon, J L, Lagourette, B, Xans, P, & Montel, F. 1998. Petroleum charcterization from ultrasonic measurement. *J. Petr. Sci. Eng.*, **19**, 281–293.

Dashti, Hameeda H., & Riazi, M. R. 2014. Acoustic velocities in petroleum fluids: Measurement and prediction. *Journal of Petroleum Science and Engineering*, **124**, 94–104.

De Robertis, Alex, & Higginbottom, Ian. 2007. A post-processing technique to estimate the signal-to-noise ratio and remove echosounder background noise. *ICES Journal of Marine Science*, **64**(6), 1282–1291.

Demer, D.A., L., Berger, M., Bernasconi, E., Bethke, K., Boswell, D., Chu, R., Domokos, & Al, Et. 2015. Calibration of acoustic instruments. *ICES Cooperative Research Report*.

Draper, Norman Richard., & Smith, Harry. 1998. *Applied Regression Analysis*. 3rd edn. New York: Wiley.

Fingas, Merv, & Brown, Carl E. 2018. A Review of Oil Spill Remote Sensing. *Sensors*, **18**(1), 91.

Francis, David T I, & Foote, Kenneth G. 2003. Depth-dependent target strengths of gadoids by the boundary-element method. *The Journal of the Acoustical Society of America*, **114**(6 Pt 1), 3136–46.

Francois, R. E., & Garrison, G. R. 1982. Sound absorption based on ocean measurements. Part II: Boric acid contribution and equation for total absorption. *The Journal of the Acoustical Society of America*, **72**(6), 1879–1890.

García, María del Carmen. 2000. Crude oil wax crystallization. The effect of heavy n-paraffins and flocculated asphaltenes. *Energy and Fuels*, **14**(5), 1043–1048.

García, María del Carmen, & Urbina, Argelia. 2003. Effect of Crude Oil Composition and Blending on Flowing Properties. *Petroleum Science and Technology*, **21**(5-6), 863–878.

George, A. K., Al-Majrafi, Naura, Singh, R. N., & Arafin, S. 2008. Thermo-elastic and thermodynamic properties of light and heavy crude oil. *Physics and Chemistry of Liquids*, **46**(3), 328–341.

GESAMP. 2007. Estimates of oil entering the marine environment from sea-based activities. *Rep. Stud. GESAMP*, **75**(96).

Greinert, Jens, Artemov, Yuriy, Egorov, Viktor, De Batist, Marc, & McGinnis, Daniel. 2006. 1300-m-high rising bubbles from mud volcanoes at 2080 m in the Black Sea: Hydroacoustic characteristics and temporal variability. *Earth and Planetary Science Letters*, **244**(1-2), 1–15.

Gross, Joachim, & Sadowski, Gabriele. 2001. Perturbed-Chain SAFT: An Equation of State Based on a Perturbation Theory for Chain Molecules. *Industrial & Engineering Chemistry Research*, **40**(4), 1244–1260.

Han, De-hua, Liu, Jianjin, & Batzle, Michael. 2010. Seismic Properties of Heavy Oils - Measured Data. *Heavy oils: reservoir characterization and production monitoring*, 73–80.

Heeschen, Katja U., Tréhu, Anne M., Collier, Robert W., Suess, Erwin, & Rehder, Gregor. 2003. Distribution and height of methane bubble plumes on the Cascadia Margin characterized by acoustic imaging. *Geophysical Research Letters*, **30**(12).

Holliday, D. V. 1972. Resonance Structure in Echoes from Schooled Pelagic Fish. *The Journal of the Acoustical Society of America*, **51**(4B), 1322–1332.

Hornafius, J Scott, Quigley, Derek, & Luyendyk, Bruce P. 1999. The world's most spectacular marine hydrocarbons seeps (Coal Oil Point, Santa Barbara Channel, California): Quantifications of emissions. *Jounral of Geophysical Research*, **104**(C9), 20703–20711.

Hu, Chuanmin, Feng, Lian, Holmes, Jamie, Swayze, Gregg A, Leifer, Ira, Melton, Christopher, Garcia, Oscar, MacDonald, Ian, Hess, Mark, Muller-Karger, Frank, Graettinger, George, & Green, Rebecca. 2018. Remote sensing estimation of surface oil volume during the 2010 Deepwater Horizon oil blowout in the Gulf of Mexico: scaling up AVIRIS observations with MODIS measurements. *Journal of Applied Remote Sensing*, **12**(02), 1.

IHS. 2015. *Offshore Rig Data: Weekly Rig Count — IHS Petrodata.*

Incardona, John P, Gardner, Luke D, Linbo, Tiffany L, Brown, Tanya L, Esbaugh, Andrew J, Mager, Edward M, Stieglitz, John D, French, Barbara L, Labenia, Jana S, Laetz, Cathy A, Tagal, Mark, Sloan, Catherine A, Elizur, Abigail, Benetti, Daniel D, Grosell, Martin, Block, Barbara A, & Scholz, Nathaniel L. 2014. Deepwater Horizon crude oil impacts the developing hearts of large predatory pelagic fish. *Proceedings of the National Academy of Sciences of the United States of America*, **111**(15), E1510–8.

Jatiault, Romain, Dhont, Damien, Loncke, Lies, de Madron, Xavier Durrieu, Dubucq, Dominique, Channelliere, Claire, & Bourrin, François. 2018. Deflection of natural oil droplets through the water column in deep-water environments: The case of the Lower Congo Basin. *Deep Sea Research Part I: Oceanographic Research Papers*, **136**(jun), 44–61.

Jech, J Michael, Horne, John K, Chu, Dezhang, Demer, David A, Francis, David T I, Gorska, Natalia, Jones, Benjamin, Lavery, Andone C, Stanton, Timothy K, Macaulay, Gavin J, Reeder, D Benjamin, & Sawada, Kouichi. 2015. Comparisons among ten models of acoustic backscattering used in aquatic ecosystem research. *Journal of the Acoustical Society of America*, **138**(6), 3742–3764.

Jones, Benjamin A., Lavery, Andone C., & Stanton, Timothy K. 2009. Use of the distorted wave Born approximation to predict scattering by inhomogeneous objects: Application to squid. *The Journal of the Acoustical Society of America*, **125**(1), 73–88.

Judd, Alan G. 2003. The global importance and context of methane escape from the seabed. *Geo-Marine Letters*, **23**(3-4), 147–154.

Kester, DANA R., Duedall, IVER W., Connors, DONALD N., & Pytkowicz, RICARDO M. 1967. PREPARATION OF ARTIFICIAL SEAWATER. *Limnology and Oceanography*, **12**(1), 176–179.

Khelladi, Hassina, Plantier, Frédéric, & Daridon, Jean Luc. 2010. A phase comparison technique for sound velocity measurement in strongly dissipative liquids under pressure. *The Journal of the Acoustical Society of America*, **128**(2), 672–8.

Kleinman, R. E., & Martin, P. A. 1988. On Single Integral Equations for the Transmission Problem of Acoustics. *SIAM Journal on Applied Mathematics*, **48**(2), 307–325.

Kristensen, Åge, & Dalen, John. 1986. Acoustic estimation of size distribution and abundance of zooplankton. *The Journal of the Acoustical Society of America*, **80**(2), 601–611.

Kulkarni, Amol A., & Joshi, Jyeshtharaj B. 2005. *Bubble formation and bubble rise velocity in gas-liquid systems: A review.*

Kvenvolden, K. A., & Cooper, C. K. 2003. Natural seepage of crude oil into the marine environment. *Geo-Marine Letters*, **23**(3-4), 140–146.

Lavery, Andone C., Chu, Dezhang, & Moum, James N. 2010. Measurements of acoustic scattering from zooplankton and oceanic microstructure using a broadband echosounder. *ICES Journal of Marine Science*, **67**(2), 379–394.

Loranger, Scott, Bassett, Christopher, Cole, Justin P., Boyle, Bret, & Weber, Thomas C. 2018. Acoustically relevant properties of four crude oils at oceanographic temperatures and pressures. *The Journal of the Acoustical Society of America*, **144**(5), 2926–2936.

Loranger, Scott, Pedersen, Geir, & Weber, Thomas C. In review. Broadband acoustic scattering from oblate hydrocarbon droplets. *The Journal of the Acoustical Society of America.*

MacDonald, I. R., Garcia-Pineda, O., Beet, A., Daneshgar Asl, S., Feng, L., Graettinger, G., French-McCay, D., Holmes, J., Hu, C., Huffer, F., Leifer, I., Muller-Karger, F., Solow, A., Silva, M., & Swayze, G. 2015. Natural and unnatural oil slicks in the Gulf of Mexico. *Journal of Geophysical Research: Oceans*, **120**(12), 8364–8380.

Medwin, Herman, & Breitz, Nigel D. 1989. Ambient and transient bubble spectral densities in quiescent seas and under spilling breakers. *Journal of Geophysical Research*, **94**(C9), 12751.

Mendelssohn, Irving A., Andersen, Gary L., Baltz, Donald M., Caffey, Rex H., Carman, Kevin R., Fleeger, John W., Joye, Samantha B., Lin, Qianxin, Maltby, Edward, Overton, Edward B., & Rozas, Lawrence P. 2012. Oil Impacts on Coastal Wetlands: Implications for the Mississippi River Delta Ecosystem after the Deepwater Horizon Oil Spill. *BioScience*, **62**(6), 562–574.

Meng, Guangtian, Jaworski, Artur J., & White, Neil M. 2006. Composition measurements of crude oil and process water emulsions using thick-film ultrasonic transducers. *Chemical Engineering and Processing: Process Intensification*, **45**(5), 383–391.

Merewether, Ray, Olsson, Mark S., & Lonsdale, Peter. 1985. Acoustically detected hydrocarbon plumes rising from 2-km depths in Guaymas Basin, Gulf of California. *Journal of Geophysical Research*, **90**(B4), 3075–3085.

Morris, Jeffrey S., Coombes, Kevin R., Koomen, John, Baggerly, Keith A., & Kobayashi, Ryuji. 2005. Feature extraction and quantification for mass spectrometry in biomedical applications using the mean spectrum. *Bioinformatics*, **21**(9), 1764–1775.

Morse, Philip M., & Ingard, K. U. 1968. *Theoretical acoustics*. Princeton, NJ: Princeton University Press.

North, Elizabeth W., Adams, E. Eric, Thessen, Anne E., Schlag, Zachary, He, Ruoying, Socolofsky, Scott A., Masutani, Stephen M., & Peckham, Scott D. 2015. The influence of droplet size and biodegradation on the transport of subsurface oil droplets during the Deepwater Horizon spill: A model sensitivity study. *Environmental Research Letters*, **10**(2), 24016.

Okumura, T, Masuya, T, Takao, Y, & Sawada, K. 2003. Acoustic scattering by an arbitrarily shaped body: an application of the boundary-element method. *ICES Journal of Marine Science*, **60**(3), 563–570.

Ozhan, Koray, Parsons, Michael L., & Bargu, Sibel. 2014. How Were Phytoplankton Affected by the Deepwater Horizon Oil Spill? *BioScience*, **64**(9), 829–836.

Parsons, M. L., Morrison, W., Rabalais, N. N., Turner, R. E., & Tyre, K. N. 2015. Phytoplankton and the Macondo oil spill: A comparison of the 2010 phytoplankton assemblage to baseline conditions on the Louisiana shelf. *Environmental Pollution*, **207**(dec), 152–160.

Pedersen, Geir. 2016. Simulation of acoustic backscattering from bubbles and droplets under different shape regimes with implications for underwater detection of leakages using active acoustic sensors. *The Journal of the Acoustical Society of America*, **140**(4), 3364–3364.

Pegau, W. Scott, Garron, Jessica, Zabilansky, Leonard, Bassett, Christopher, Bello, Job, Bradford, John, Carns, Regina, Courville, Zoe, Eicken, Hajo, Elder, Bruce, Eriksen, Peter, Lavery, Andone, Light, Bonnie, Maksym, Ted, Marshall, Hans-Peter, Oggier, Marc, Perovich, Don, Pacwiardowski, Pawel, Singh, Hanumant, Tang, Dajun, Wiggins, Chris, & Wilkinson, Jeremy. 2017. Detection of oil in and under ice. *International Oil Spill Conference Proceedings*, **2017**(1), 1857–1876.

Plantier, F., Bessières, D., Daridon, J. L., & Montel, F. 2008. Structure and thermodynamic consistency of heavy oils: A study on the basis of acoustic measurements. *Fuel*, **87**(2), 196–201.

Roberts, Harry H., & Carney, Robert S. 1997. Evidence of episodic fluid, gas, and sediment venting on the northern Gulf of Mexico continental slope. *Economic Geology*, **92**(7-8), 863–879.

Römer, Miriam, Sahling, Heiko, Pape, Thomas, Bohrmann, Gerhard, & Spieß, Volkhard. 2012. Quantification of gas bubble emissions from submarine hydrocarbon seeps at the

Makran continental margin (offshore Pakistan). *Journal of Geophysical Research: Oceans*, **117**(oct).

Ronningsen, Hans Petter, Bjorndal, Brit, Hansen, Asger Baltzer, & Pedersen, Walther Batsberg. 1991. Wax Precipitation from North Sea Crude Oils. 1. Crystallization and Dissolution Temperatures, and Newtonian and Non-Newtonian Flow Properties. *Energy and Fuels*, **5**(6), 895–908.

Rozas, Lawrence P, Minello, Thomas J, & Henry, Charles B. 2000. An assessment of potential oil spill damage to salt marsh habitats and fishery resources in Galveston Bay, Texas. *Marine Pollution Bulletin*, **40**(12), 1148–1160.

Sahling, Heiko, Borowski, Christian, Escobar-Briones, Elva, Gaytán-Caballero, Adriana, Hsu, Chieh-Wei, Loher, Markus, MacDonald, Ian, Marcon, Yann, Pape, Thomas, Römer, Miriam, Rubin-Blum, Maxim, Schubotz, Florence, Smrzka, Daniel, Wegener, Gunter, & Bohrmann, Gerhard. 2016. Massive asphalt deposits, oil seepage, and gas venting support abundant chemosynthetic communities at the Campeche Knolls, southern Gulf of Mexico. *Biogeosciences*, **13**(aug), 4491–4512.

Schneider von Deimling, J., Rehder, G., Greinert, J., McGinnnis, D.F., Boetius, A., & Linke, P. 2011. Quantification of seep-related methane gas emissions at Tommeliten, North Sea. *Continental Shelf Research*, **31**(7), 867–878.

Śmigaj, Wojciech, Betcke, Timo, Arridge, Simon, Phillips, Joel, & Schweiger, Martin. 2015. Solving Boundary Integral Problems with BEM++. *ACM Transactions on Mathematical Software*, **41**(2), 1–40.

Socolofsky, Scott A., Adams, E. Eric, & Sherwood, Christopher R. 2011. Formation dynamics of subsurface hydrocarbon intrusions following the Deepwater Horizon blowout. *Geophysical Research Letters*, **38**(9), n/a–n/a.

Stanton, Timothy K., & Chu, Dezhang. 2000 (aug). *Review and recommendations for the modelling of acoustic scattering by fluid-like elongated zooplankton: Euphausiids and copepods.*

Stanton, Timothy K., & Chu, Dezhang. 2008. Calibration of broadband active acoustic systems using a single standard spherical target. *The Journal of the Acoustical Society of America*, **124**(1), 128–136.

Stanton, Timothy K, Chu, Dezhang, Wiebe, Peter H, & Clay, Clarence S. 1993. Average echoes from randomly oriented random-length finite cylinders: Zooplankton models Scattering of an obliquely incident acoustic wave by an infinite cylinder Determining dominant scatterers of sound in mixed zooplankton populations. *The Journal of the Acoustical Society of America Acoustical Society of America The Journal of the Acoustical Society of America*, **94**(119), 1397–1832.

Stanton, Timothy K., Chu, Dezhang, & Wiebe, Peter H. 1998. Sound scattering by several zooplankton groups. II. Scattering models. *The Journal of the Acoustical Society of America*, **103**(1), 236.

Stanton, Timothy K., Chu, Dezhang, Jech, J. Michael, & Irish, James D. 2010. New broadband methods for resonance classification and high-resolution imagery of fish with swimbladders using a modified commercial broadband echosounder. *ICES Journal of Marine Science*, **67**(2), 365–378.

Terrill, Eric J., & Melville, W. Kendall. 2000. A Broadband Acoustic Technique for Measuring Bubble Size Distributions: Laboratory and Shallow Water Measurements. *Journal of Atmospheric and Oceanic Technology*, **17**(2), 220–240.

Thompson, Charles H., & Love, Richard H. 1996. Determination of fish size distributions and areal densities using broadband low-frequency measurements. *ICES Journal of Marine Science*, **53**(2), 197–201.

Transportation Research Board and National Research Council. 2003. Natural Seepage of Crude Oil into the Marine Environment. *Pages 191–192 of: Oil in the Sea III: Inputs, Fates, and Effects.*

Turin, George L. 1960. An Introduction to Matched Filters. *IRE Transactions of Information Theory*, **IT-6**, 311–329.

United States, & Coast Guard. 2011. Coordinator Report Deepwater Horizon. *On Scene Coordination Report Deepwater Horizon Oil Spill.*

U.S. Department of Energy, Energy Information Administration, Independent Statistics & Analysis. 2016. *Offshore oil production in deepwater and ultra-deepwater is increasing - Today in Energy - U.S. Energy Information Administration (EIA).*

US EPA. 2007. *Test Methods for Evaluating Solid Waste, Physical/Chemical Methods.* Vol. Third Edit.

Vagle, Svein, & Farmer, David M. 1992. The Measurement of Bubble-Size Distributions by Acoustical Backscatter. *Journal of Atmospheric and Oceanic Technology*, **9**(5), 630–644.

Valentine, David L., Kessler, John D., Redmond, Molly C., Mendes, Stephanie D., Heintz, Monica B., Farwell, Christopher, Hu, Lei, Kinnaman, Franklin S., Yvon-Lewis, Shari, Du, Mengran, Chan, Eric W., Tigreros, Fenix Garcia, & Villanueva, Christie J. 2010. Propane respiration jump-starts microbial response to a deep oil spill. *Science*, **330**(6001), 208–211.

Van Der Ham, Joris L., & De Mutsert, Kim. 2014. Abundance and size of gulf shrimp in louisiana's coastal estuaries following the deepwater horizon oil spill. *PLoS ONE*, **9**(10), e108884.

Vazquez, D, & Mansoori, G. A. 2000. Identification and measurement of petroleum precipitates. *Pages 49–55 of: Journal of Petroleum Science and Engineering*, vol. 26. Elsevier.

Venn-Watson, Stephanie, Colegrove, Kathleen M., Litz, Jenny, Kinsel, Michael, Terio, Karen, Saliki, Jeremiah, Fire, Spencer, Carmichael, Ruth, Chevis, Connie, Hatchett, Wendy, Pitchford, Jonathan, Tumlin, Mandy, Field, Cara, Smith, Suzanne, Ewing, Ruth, Fauquier, Deborah, Lovewell, Gretchen, Whitehead, Heidi, Rotstein, David, McFee, Wayne, Fougeres, Erin, & Rowles, Teri. 2015. Adrenal gland and lung lesions in Gulf of Mexico common bottlenose dolphins (Tursiops truncatus) found dead following the Deepwater Horizon oil spill. *PLoS ONE*, **10**(5), e0126538.

Weber, Thomas C., & Ward, Larry G. 2015. Observations of backscatter from sand and gravel seafloors between 170 and 250 kHz. *The Journal of the Acoustical Society of America*, **138**(4), 2169–2180.

Weber, Thomas C, De Robertis, Alex, Greenaway, Samuel F, Smith, Shep, Mayer, Larry, & Rice, Glen. 2012. Estimating oil concentration and flow rate with calibrated vessel-mounted acoustic echo sounders. *Proceedings of the National Academy of Sciences of the United States of America*, **109**(50), 20240–5.

Weber, Thomas C., Mayer, Larry, Jerram, Kevin, Beaudoin, Jonathan, Rzhanov, Yuri, & Lovalvo, Dave. 2014. Acoustic estimates of methane gas flux from the seabed in a 6000 km2 region in the Northern Gulf of Mexico. *Geochemistry, Geophysics, Geosystems*, **15**(5), 1911–1925.

Weidner, Elizabeth, Weber, Thomas C., Mayer, Larry, Jakobsson, Martin, Chernykh, Denis, & Semiletov, Igor. 2019. A wideband acoustic method for direct assessment of bubble-mediated methane flux. *Continental Shelf Research*, **173**(feb), 104–115.

Wiggins, Sean M., Leifer, Ira, Linke, Peter, & Hildebrand, John A. 2015. Long-term acoustic monitoring at North Sea well site 22/4b. *Marine and Petroleum Geology*, **68**, 776–788.

Wilkinson, J. P., Boyd, T., Hagen, B., Maksym, T., Pegau, S., Roman, C., Singh, H., &

Zabilansky, L. 2015. Detection and quantification of oil under sea ice: The view from below. *Cold Regions Science and Technology*, **109**(jan), 9–17.

Wunderlich, Bernhard. 1990. *Thermal analysis*. Boston: Academic Press.

Zhao, Lin, Boufadel, Michel C., Socolofsky, Scott A., Adams, Eric, King, Thomas, & Lee, Kenneth. 2014. Evolution of droplets in subsea oil and gas blowouts: Development and validation of the numerical model VDROP-J. *Marine Pollution Bulletin*, **83**(1), 58–69.

Zheng, Li, & Yapa, Poojitha D. 2000. Buoyant Velocity of Spherical and Nonspherical Bubbles/Droplets. *Journal of Hydraulic Engineering*, **126**(11), 852–854.